Development of Dual Mode Labels for the Quantitative Analysis of Surface Functional Groups with XPS and Fluorescence

D i s s e r t a t i o n
Zur Erlangung des akademischen Grades
doctor rerum naturalium (Dr. rer. nat.)

im Fach Chemie:
Angewandte Analytik und Umweltchemie

eingereicht an der
Mathematisch-Naturwissenschaftlichen Fakultät
der **Humboldt-Universität zu Berlin**

von
Dipl.-Chem. Tobias Fischer

Präsidentin der Humbold-Universität zu Berlin:
Prof. Dr.-Ing. habil. Dr. Sabine Kunst
Dekan der Mathematisch-Naturwissenschaftlichen Fakultät:
Prof. Dr. Elmar Kulke

Gutachter: 1. Prof. Dr. Ulrich Panne
2. Prof. Dr. Klaus Rademann

Tag der mündlichen Prüfung: 23.02.2017

For my mother – and my little one.

May her spirit be your guide.

You can use logic to justify almost anything. That's its power – and its flaw.

Captain Kathryn Janeway, *Star Trek Voyager*

Abstract

The aim of this work was the development of dual-mode labelling method that allows to combine the precise and reliable quantitative information of X-ray photoelectron spectroscopy (XPS) with the fast and widely available fluorescence measurements for surface functional group quantification. A set of label dyes combining robust fluorescence properties with high fluorine contents were investigated towards their selective reaction with surface amino groups and the lead candidate subjected to detailed analysis on simple model surfaces. It was found that fluorescence quenching on such samples precluded a detailed investigation of the capabilities of dual-mode labelling, despite providing sufficient signal in XPS and fluorescence scanning. The fabrication process of the model surfaces based on vapour deposition (VD) of silanes in toluene was optimized stepwise under aid of contact angle (CA) measurements. Finally, a procedure to prepare surfaces with variable amounts of surface functional groups was developed using binary mixtures of mono-alkoxy silanes at different ratios. Through Cassie's law, the relative surface functional group fractions could be estimated from the contact angle measurement. Such samples were treated with the label dye to show that XPS and fluorescence provide a linear overlap in signal generation over at least one order of magnitude. The combination of synchrotron radiation XPS (SR-XPS) and total reflection X-ray fluorescence spectroscopy (TXRF) provided an absolute and traceable quantification of the surface functional group density.

Different model surfaces based on tri-alkoxy silanes showed that fluorescence quenching can not be excluded on realistic samples. A fluorescence lifetime based correction was developed to account for such quenching effects. Additionally, the application of spectrophotometry provided a independent method of quantification for the surface bound dye which allowed, in combination with information obtained from XPS, to determine the surface functional group density in high precision. With cavity ring-down spectroscopy (CRDS), a laser based technique for highly sensitive and spatially resolved absorption measurements on transparent substrates could be developed and applied in a proof-of-concept. A modular system for the fabrication of label dyes with adjustable spectral properties and different binding sites was investigated using prototype candidates to prove the general applicability of such systems and identify problems involved in this approach.

Zusammenfassung

Das Ziel dieser Arbeit war die Entwicklung einer Derivatisierungsmethode, die die duale Quantifizierung funktioneller Gruppen an Oberflächen mittels Röntgenphotoelektronenspektroskopie (XPS) und Fluoreszenz ermöglicht, um die genauen und verlässlichen Information aus XPS mit der Einfachheit der Fluoreszenzmessung zu kombinieren. Verschiedene Derivatisierungsreagenzien, die robuste Fluoreszenzeigenschaften mit hohen Fluorgehalten für XPS kombinieren, wurden auf ihre selektive Reaktion mit Aminogruppen getestet und der Prototyp einer tiefergehenden Analyse auf einer Modelloberfläche unterzogen. Durch Fluoreszenzlöschung konnten die Möglichkeiten der bimodalen Analyse nur begrenzt abgeschätzt werden, obwohl in beiden Methoden, XPS und Fluoreszenzscannen, intensive Signale gemessen wurden. Die Herstellung der Modelloberflächen mittels Gasphasenabscheidung von Silanen konnte unter Zuhilfenahme der Kontaktwinkelmessung schrittweise optimiert werden. Schließlich wurde ein Verfahren entwickelt, mit dem Oberflächen mit variabler Funktionalgruppendichte aus der Kombination zweier Monoalkoxysilane hergestellt werden können. Cassie's Gesetz erlaubt hier die Abschätzung der relativen Beträge der funktionellen Gruppen durch die Kontaktwinkelmessung. Die Analyse dieser Oberflächen nach Reaktion mit dem dualen Marker zeigte, dass XPS und Fluoreszenz mindestens über eine Größenordnung korrelieren. Durch Synchrotron-XPS (SR-XPS) und Röntgenfluoreszenz unter Totalreflektion (TXRF) konnte eine absoule und rückführbare Bestimmung der Funktionalgruppendichte erzielt werden.

Weitere Modelloberflächen auf Basis von Trialkoxysilanen zeigten, dass bei anwendungsnahen Proben Fluoreszenzlöschung nur schwerlich verhindert werden kann. Diese konnte in einem gewissen Maße mittels Fluoreszenzlebensdauer berechnet werden. Darüberhinaus konnte mit der Photometrie eine unabhängige Methode gefunden werden, die die Quantifizierung des Farbstoffs an der Oberfläche in hoher Präzision ermöglicht und mit Hilfe der XPS damit auch der funtionellen Gruppen. Die Cavity Ring-Down Spektroskopie (CRDS) wurde als Laserbasierte Methode zur empfindlichen und ortsaufgelösten Messung der Absorption auf transparenten Substraten untersucht und erste vielversprechende Ergebnisse gewonnen. Weiterhin wurde ein modulares Farbstoffsystem entwickelt, das sowohl Variation der spektralen als auch der Bindungseigenschaften erlaubt. Erste Versuche mit Prototypen aus diesem Bausatz zeigten zwar gutes Bindungsverhalten, aber auch einige Probleme in der dualen Analyse.

Contents

Acknowledgement

I want to thank Mister Panne for providing me with the opportunity to write my thesis at BAM. My very special gratitude goes to Knut Rurack, my supervisor for so many years. You made me the scientist I am today. My colleagues at division 1.9 also deserve special acknowledgement for keeping up with me through all this time, especially Mandy Hecht, Jeannine Wehr and Wei Wan, whose affords directly affected this work. Thanks goes to Wolfgang E.S. Unger from division 6.8 not only for acquiring the funding for my long hours at BAM, but also for his scientific support. From the same group Paul M. Dietrich is the one who teached me the fundamentals of XPS and how to understand my data. Accordingly, I acknowledge the EMRP, jointly funded by EURAMET and the European Union, for the funding of this work and the entire SurfChem Project. The same project that made it possible for me to go to NPL in London. That was a special time, thanks to Alex G. Shard who teached me so much in so little time, Santanu Ray, who took his task of being my guide very seriously, thank you for always having an open ear for all sorts of problems. There are so many of you I got to know there at NPL and I am happily calling my friends now, it is impossible to name you all. But I will always cherish the experience and the memories you provided me with. And I hope you found somebody else to organize the Pub crawls.

My special thanks goes out to my family and friends, to my sister, for always being there. That bound cannot be separated. To my father for his constant support for everything I came up with, irrespective of being a good idea or not. I will carry on your approach of raising a child: An experience made is a lesson learned.

Finally, this entire work would not have been possible without the one person, who was always with me, physically or mentally, who supported me when I went across the sea, not to far luckily, shared so many experiences with me, being with me or not, my compass, whose empathy and impeccable understanding of the human nature guided me through to all those little conflicts on the way, the one person who will always be there for me as I will always be there for you. To my wife Katharina. I am not complete without you.

Acronyms

AFM	atomic force microscopy
AHAMTES	*N*-(6-aminohexyl)aminomethyltriethoxysilane
APDIPES	(3-aminopropyl)diisopropylethoxysilane
APDMES	(3-aminopropyl)dimethylethoxysilane
APTES	(3-aminopropyl)triethmendeleyoxysilane
ARCA	advancing and receding contact angle
AR-XPS	angle resolved XPS
BAM	Bundesanstalt für Materialforschung und -prüfung
BODIPY	boron-dipyrromethene
BTPITC	3,5-bis(trifluoromethyl)phenyl isothiocyanate
Bu_2O	dibutyl ether
CA	contact angle
CD-XPS	chemical derivatization XPS
CETES	(2-cyanoethyl)triethoxysilane
CLSM	confocal laser scanning microscope
CPDMMS	(3-cyanopropyl)dimethylmethoxysilane
CRDS	cavity ring-down spectroscopy
CVD	chemical vapour deposition
DIC	*N,N'*-diisopropylcarbodiimide
DIPEA	*N,N*-diisopropyl-ethylamin (Hünig's base)
DMF	*N,N*-dimethylformamide
ESCA	electron spectroscopy for chemical analysis
Et_2O	diethyl ether
EtOH	ethanol
FITC	fluorescein isothiocyanate
FLOSS	fluorescence labelling of surface species

Fluram	4-phenylspiro-[furan-2(3H),10-pthalan]-3,30-dione
FTIR	Fourier transform infrared spectroscopy
GOPTMS	(3-glycidoxypropyl)trimethoxysilane
Hex	*n*-hexane
IPA	isopropyl alcohol
LOD	limit of detection
MeCN	acetonitrile
MeOH	methanol
MPTMS	(3-mercaptopropyl)trimethoxysilane
NEXAFS	X-ray absorption near edge fine structure
NHS	*N*-hydroxysuccinimide
NIR	near infrared
NMR	nuclear magnetic resonance
NPL	National Physical Laboratory
OPA	optical parametric amplifier
PE	petrol ether
PET	photoinduced electron transfer
PFA	perfluoroalkoxy alkane
PFB	pentafluorobenzaldehyde
PMT	photomultiplier tube
PP	polypropylene
PPS	poly(p-phenylene sulfide)
PTFE	polytetrafluoroethylene
PTMS	n-propyltrimethoxysilane
Rh101	Rhodamine 101
Rh6G	Rhodamine 6G
RITC	Rhodamine B isothiocyanate
SAM	self-assembled monolayer
SESSA	simulation of electron spectra for surface analysis
SR-XPS	synchrotron radiation XPS
TFA	trifluoroacetic acid
TFAA	trifluoroacetic anhydride
TFBA	(4-trifluoromethyl)benzaldehyde

THF	tetrahydrofuran
TLC	thin layer chromatography
ToF-SIMS	time-of-flight secondary ion mass spectrometry
Tol	toluene
TXRF	total reflection X-ray fluorescence spectroscopy
UHV	ultra-high vacuum ($<10^{-9}$ mbar)
US	ultrasound
UV	ultraviolet
VD	vapour deposition
XPS	X-ray photoelectron spectroscopy

Symbols and Constants

$\boldsymbol{A}$	optical absorption
ε_λ	molar absorption coefficient at wavelength λ $\left[\mathrm{M}^{-1}\,\mathrm{cm}^{-1}\right]$
$f_\mathbf{1}$	functional component fraction determined via Cassies's Law
$f_\mathbf{a}$	functional component fraction as applied to the preparation
$f_\mathbf{f}$	functional component fraction represented by the normalized fluorescence intensity
$f_\mathbf{t}$	functional component fraction determined by ToF-SIMS
$f_\mathbf{x}$	functional component fraction as determined from XPS
$\boldsymbol{F}$	fluorescence intensity
$\theta_\mathbf{C}$	static contact angle [°]
$\theta_\mathbf{adv}$	advancing contact angle [°]
$\theta_\mathbf{rec}$	receding contact angle [°]
$\theta_\mathbf{hys}$	contact angle hysteresis [°]
$k_\mathbf{nr}$	non-radiative decay constant [$10^8\ \mathrm{s}^{-1}$]
$k_\mathbf{r}$	radiative decay constant [$10^8\ \mathrm{s}^{-1}$]
$\mathbf{P}$	power [W]
$\Phi_\mathbf{f}$	fluorescence quantum yield
$\tau_\mathbf{f}$	fluorescence lifetime [s]
$\boldsymbol{T}$	optical transmission
$\boldsymbol{Z}$	atomic number

1 Introduction

In 1990, when the Humane Genome Project set out with the aim to sequence the entire human genome in just 15 years, it was widely regarded a bold endeavour.[1,2] But in time the effort was justified: the project managed to sequence the entire human genome, base-pair for base-pair, even two years ahead of schedule. That was only possible due to the major progress made in sequencing technologies during the projects term, reducing both time and cost of the sequencing. And the end of Human Genome Project does not mark the end of this development, on the contrary.[3] Whereas the first full human genome sequence, based on Sangers chain termination method,[4,5] just cost about 13 billion US$ and took 13 years, it is now possible to sequence the entire genome of a human individual for about 1000 US$ in a single day.[6]

One of the more prominent technologies that emerged along this project are the DNA array technologies. Here, DNA single strands are immobilized on a flat solid surface and the interaction with their complementary sequence, e.g. the relative amount of its expression, can be quantified via appropriate fluorescence labelling.[7] With modern technologies, all possible DNA 12mers, based on the four DNA bases, can be printed on a single microscope slide and full expression be quantified, with $>10^6$ individual assays.[8,9]

Whereas this technology was surpassed in its sequencing capabilities by the so called „next-generation sequencing“ methods, which are mostly Sanger-based, yet combined with highly-parallel techniques,[10] its power in complex expression analysis is still unrivalled. This analysis, together with the decoded sequence, allows to connect certain DNA sequences to specific expressions of proteines, for example. Having such information available is crucial to understand the role of those sequences on the cellular system.[11] Medical applications for example target DNA sequences that are known to have harmful effects to prevent their expression.[12]

Although DNA arrays are the foundation of this technological development and still provide the majority of microarray assays, this technology is not limited to them.[13] Having such a highly developed technology for the fast and precise analysis of a multitude of analytes together with the high degree of multiplexing achieved with spatial resolution, other fields of bioanalysis thrived to exploit it as well. Interaction studies with immobilized proteins,[14–16] miniaturized and multiplexed immunoassays,[17–20] sugar-binding studies,[21] pharmaceutical high-throughput screening,[22–24] and even full-cell studies have been shown.[25] Several methods of

read-out were realized, including the abundant laser scanning and chemiluminescence.[7,26,27] Whereas the technology of signal generation and detection and the types of molecules immobilized received significant attention, the surfaces used to attach those compounds are only rarely studied in detailed, despite being a fundamental prerequisite to a successful assay.[28,29] As it will be shown later, the technologies commonly used to characterize such substrates are rare and much more common in the fields of physics rather than biology. Accordingly, the target assay is tested under various conditions and substrates until an optimum combination is found. The absence of detailed knowledge on the substrate precludes a concise choice of the parameters.

To overcome this limitation, this work aims to provide a simple assay to judge the quality of a substrate in terms of density and homogeneity of the surface functional group and finally enable a simple approach to choose a suitable substrate. This shall be achieved by developing a label compound that is compatible to the widely employed read-out methods, including fluorescence laser scanning and microscopy, yet can be traced back to significantly more detailed information based on comprehensive surface analytical techniques.

1.1 Organic surfaces in Bioanalysis

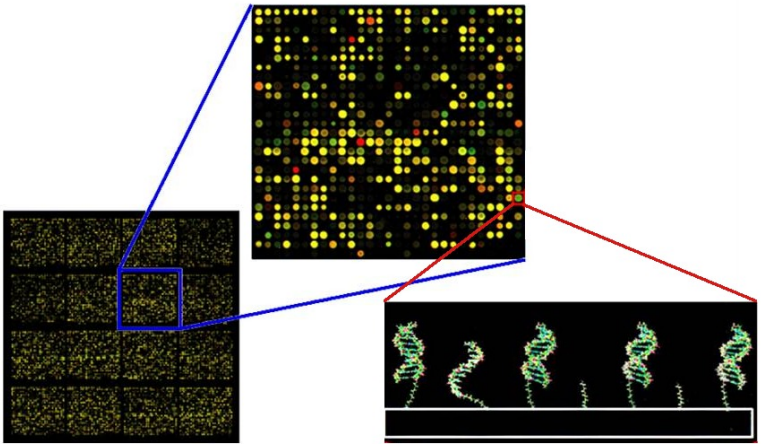

Figure 1.1: Illustration of the spot density and read-out of a DNA microarray and the molecular attachment to the substrate surface (DNA on surface image reprinted from ref. 28)

More or less all of the arrays described above, irrespective of the target material, are fundamentally dependent on an organic surface. Most of the investigations of this dependency focussed on the type of functional group, which can rather easily be modified,[30,31] and to a lesser extent on the structure of the surface.[32] This work on biomolecule capturing on organic surfaces even precedes the development of microarray technology.[33] Figure 1.1 shows an exemplary magnification process of a DNA microarray and illustrates how the DNA strands are attached to the surface.

The performance of biomolecular arrays depends on how those biomolecules are immobilized on the surface. Southern *et al.* provide a comprehensive discussion of DNA interactions on surfaces, where they point out that not only the sequence and the length are influential on the array performance, but also the structure and the density of the immobilization.[28] Shircliff *et al.* compared glass surfaces functionalized with trialkoxy- and monoalkoxy silanes, where the latter provide smoother surfaces with a lesser density of functional groups.[34] They found that despite the denser surface showing a high *binding capacity* for the capture sequence, the *hybridization efficiency*, describing the ratio of immobilized single-strand DNA that is available to bind its counter-strand, is higher for the monoalkoxy silane surface since the lesser density of strands leaves more space for the counter-strands to interact and the monolayer like arrangement avoids coiling of the single-strands. Similar findings where made by Peterson *et al.*, although they relied on varying the immobilization time to vary the surface density of probe molecules.[35] They also found that the hybridization of mismatched DNA depends on the target density.[36] It should be kept in mind that in terms of structure and interaction, DNA is probably the easiest class of biochemical targets for a microarray system. In case of proteins, for example, not only the density but also the point of attachment and the resulting orientation play a pivotal role in the activity of the protein on the surface.[16] Accordingly, different studies were performed dealing with the effects of structure and functionalization of the surfaces on the performance of protein assays, including stability and efficiency of the immobilized protein.[14–16,29,37,38] They all found that apart from the type of functional group, their abundance and availability significantly affect the assay.

However, the described effects are not limited to individual bio-molecules on surfaces. Lee *et al.* described the effects of surface charge and wettability on the behaviour of cells on surfaces and found that not only the functional groups themselves, but also their densitity and charge, are paramount parameters on the immobilization and growth of cells on surfaces.[39,40]

All these effects clearly show that reliable application of functionalized surfaces, especially in bio-analytical laboratories on a day-to-day basis with high repeatability of the performed assays, depends decisively on the structure and functional group density of those surfaces. However, reliable assays to allow for a routine characterization of these parameters are exceedingly rare.

1.2 Methods of surface functional group quantification

The quantification of functional groups on surfaces involves the main problem of surface analysis: The discrimination of the surface from the bulk material. Two general approaches are considered to circumvent that problem: First, a technique can be used that is inherently surface sensitive, meaning that only the top few nanometre of a surface are analysed. Typical examples of such techniques are X-ray photoelectron spectroscopy (XPS) or time-of-flight secondary ion mass spectrometry (ToF-SIMS).

Second, one could render a bulk technique surface sensitive by introducing a specific signal to the surface. Very rarely the analyte on the surface, in our case the surface functional group, comprises a sufficiently strong signal to be analysed directly despite the bulk background with, for example, vibrational spectroscopy. Much more common is the derivatization of the targeted functional group with a specific label that the involved technique is very sensitive for. Various methods are compatible with this approach, like Fourier transform infrared spectroscopy (FTIR), nuclear magnetic resonance (NMR), Raman spectroscopy and of course the fluorescence based techniques like fluorescence microscopy, spectroscopy or scanning. However, a high sensitivity of the analytical technique is still required: In the case of small particles with their high surface-to-volume ratios analysis is not only possible with FTIR and NMR,[41,42] but also with indirect techniques like conductometry and zeta-potential measurement.[43] The total number of functional groups on *flat* substrates, however, is too low to be analysed with those comparatively insensitive techniques. That is why the techniques commonly employed in surface functional group quantification are, in comparison, limited. The most important will be discussed here in detail.

1.2.1 Chemical derivatization XPS (CD-XPS)

XPS, or electron spectroscopy for chemical analysis (ESCA), is a surface analytical technique that provides information about the relative elemental composition of a surface, for elements with $Z > 3$. Apart from the elemental information certain knowledge about the chemical state of these elements can be obtained, hence electron spectroscopy for chemical analysis. The quantitative information is usually provided relatively in atom percentage (at%) rather

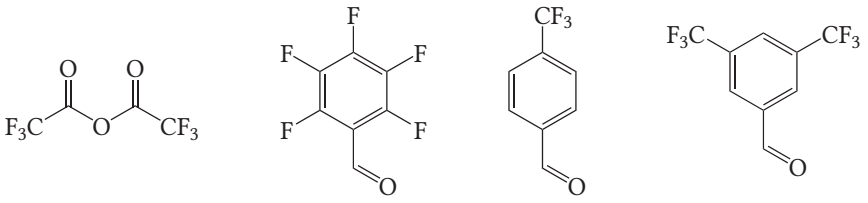

TFAA **PFB** **TFBA** **BTPITC**

Scheme 1.1: Structures of relevant surface amino group labels for XPS analysis

than absolute values. The sensitivity of the method varies for different elements but can be as low as 0.003 at%, depending on the element and the matrix (other elements in the sample can influence the sensitivity through several effects, including overlapping peaks).[44] In a typical XPS experiment, an untreated sample is transferred into the ultra-high vacuum (UHV) analysis chamber and exposed to high-energy X-Ray radiation, typically Mg or Al K_α. The high-energy radiation excites core-level electrons of atoms on the surface to leave the sample, these electrons are subsequently analysed with an electron energy analyser. Despite the penetration depth of the X-rays being several micrometre, the information depth of XPS is typically around 10 nm. The reason for this is that the photoelectrons have to actually escape the sample to be analysed, however, the excited electron will be involved in several interactions in the matter, including inelastic collisions, recombination and re-excitation, which influences increase exponentially with the depth of the excitation. Accordingly, the signals from atoms deeper in the sample are increasingly attenuated compared to atoms directly at the surface. This effect can be exploited for semi-quantitative analysis since it allows to measure the thickness of a surface layer through its dampening of the signal intensity of the bulk material.[45,46] This effect was used to quantify proteins on gold layers.[47] The surface sensitivity of XPS can be enhanced if the surface-to-analyzer angle is changed to angles lower than the commonly used 90° (angle resolved XPS (AR-XPS)).[48] As electrons can only travel a given distance through a material before an interaction resulting in an energy loss occurs (the inelastic mean free path of an electron), changing the angle at which electrons are detected from the surface increases the surface contribution to the measured XPS signal. However, common laboratory instruments only allow crude adjustments of this angle and critical parameters for XPS-spectra are only well-understood for normal geometry. The chemical shifts in XPS are not even remotely as pronounced as in NMR for example and peak-fitting of the overlapping peaks found for one element commonly needs to be applied. This often prohibits a clear solution, since baseline separation only seldomly occurs, and detailed knowledge of the sample is required for a reliable allocation.[49] Accordingly, quantitative analysis of surface functional groups still relies

on chemical derivatization of the target. The label that is applied usually contains at least one unique element not found in the surface itself to allow unequivocal allocation of the signal to the surface functional group. The major pre-requisite for this approach is that the labelling is performed quantitatively, e.g. that all surface functional groups are labelled. Since the conditions on a surface are very dense, conventional solution reactions that are considered quantitative do not necessarily work the same way on a surface and careful analysis is essential when introducing a new label. A good introduction to that problem and a number of labels for various functional groups can be found in Batich's comprehensive review.[49]

Surface amino groups are of superior importance in this work; only a limited number of derivatization agents is commonly used for them in the literature: trifluoroacetic anhydride (TFAA),[50–55] pentafluorobenzaldehyde (PFB),[56,57] (4-trifluoromethyl)benzaldehyde (TFBA)[58–60] and very occasionally 3,5-bis(trifluoromethyl)phenyl isothiocyanate (BTPITC)[61] (see Scheme 1.1). Whereas TFAA is considered preferential due to its small size and high fluorine content, it carries the disadvantage, especially for glass based materials, of being reactive towards hydroxyl groups as well.[50,62] PFB is capable of quantitative binding in vapour phase as well as in solution and provides a reversible binding chemistry, which is relevant in case the samples needs to be retrieved. However, as Yegen *et al.* observed,[54] PFB appears to be prone to C–F bond cleavage under X-ray irradiation due to the susceptibility of the C–F bond to nucleophilic substitution.[63] TFBA on the other hand appears resistant to that effect and is suggested as an alternative to PFB, despite the lesser fluorine content. Graf *et al.* used 3,5-bis(trifluoromethyl)phenyl isothiocyanate (BTPITC) as a XPS-label.[61] Apart from the high fluorine content, the surface binding of BTPITC relies on the isocyanate-amino reaction, which is commonly used to anchor biomolecules on surfaces.[16] In combination with NEXAFS studies, they could show that this particular label is capable of near quantitative labelling of amino-groups of thiols bonded to gold surfaces, whereas only ~30 % of the amino groups on amino-silane functionalized glass surfaces could be derivatized. Even less amino groups could be transformed on aminated polyethylene owing to the complicated structure of polymeric substrates. In contrast to aminated glass and gold surfaces, the bulk material here is the same as the surface material and nitrogen cannot be unequivocally allocated to surface amino groups. The limit of detection (LOD) for chemical derivatization XPS (CD-XPS) basically depends on the LOD of the considered elements and is around ~0.1 functional groups nm^{-2} for fluorinated derivatization agents.[64,65] Apart form the surface functional group quantification after chemical derivatization, XPS is very well suited to provide information on the structure and thickness of organic films on different substrates, as it had been shown in numerous publications.[42,48,58,59,66–72]

1.2.2 Fluorescence labelling of surface species

Due to the abundance of fluorescence instrumentation, especially in laboratories dealing with bio-functionalized surfaces, most publications concerning organo-modified substrates apply fluorescence labelling of surface species (FLOSS) in one or the other way. Either simply as a proof for the presence of certain functional group,[73,74], as relative comparison of functional group densities,[29,75–79] or as an absolute quantification method.[52,64,80–83] The latter provides the theoretical advantage over CD-XPS that the signal intensity can directly be transformed into a number of molecules, if a careful calibration has been performed. Unlike in CD-XPS, the case of incomplete functional group labelling can hardly be identified and the number of functional groups is usually underestimated, particularly since the molecular labels applied in FLOSS are significantly larger than XPS-labels. The number of functional groups assessed with FLOSS is accordingly often treated as the number of *accessible* functional groups rather than the *total* amount of functional groups.[83] If the chemistry applied to bind the dye is comparable to the later bio-functionalization of the surface, that parameter can be sufficient as a characterization. An unique problem arising in FLOSS is the limitation of its upper dynamic range by fluorescence quenching. Here, the measured signal does not increase linearly or even decreases as the number of dyes on the surface increases.[51,81] Fluorescence quenching can be identified to a certain extent in spectroscopic measurements,[79] clear identification requires time-resolved measurements.[84,85] Most notably, quenching effects can hardly be identified on filter based fluorescence equipment which does not offer spectroscopically, let alone time-, resolved measurements. Since these filter based measurements, for example with fluorescence scanners and microscopes, are typically used for FLOSS, fluorescence quenching can easily yield to strong underestimation of the surface functional group density.

In contrast to CD-XPS, the limit of detection in FLOSS is slightly more complex to access and varies throughout the literature, depending on the substrate and the technique. Whereas Ivanov *et al.* report a LOD of 0.01 functional groups nm^{-2} for measurements performed with a spectrometer on plastic surfaces, with the diffraction of the excitation light on the substrate being the limitation,[64] Wayment *et al.* performed quantification at a single-emitter counting level at a 10^{-7} fraction of a monolayer, with the background fluorescence of the substrate as the limitation.[73] Generally, a LOD of ~0.001 functional groups nm^{-2} seems reasonable.[65,86,87] The inherent advantage of FLOSS is that adapting the applied protocol can potentially lower the LOD if necessary, like changing the instrumentation from a spectrometer to a laser scanner or a microscope, or changing the label dye to go to a wavelength region with less pronounced substrate fluorescence.[86]

Concerning the instrumentation, different techniques bear particular advantages and can be selected according to the current need. Fluorescence spectrometers, despite being less sensitive for fluorescence on solid surfaces, provide unprecedented spectral resolution and are advantageous if detailed spectral information, like broadening or shifts of emission bands are investigated.[88] Fluorescence intensities can also be evaluated with spectrometers, if careful background correction is applied. A significant drawback of these instruments is their lack of spatial resolution, so that sample homogeneity is very difficult to assess. Microarray scanners are favourable for this endeavour, since they provide large area scans (commonly 72 mm × 22 mm, higher areas are possible with combined microarray/microplate readers) with a resolution at the lower µm-range. The laser scanning provides homogeneous excitation and detection throughout the scan, meaning that the homogeneity of the coating of a slide can easily be derived from the fluorescence scan and instrumental factors are only marginally important. The high repeatability of the sample positioning also provides a high reproducibility and accordingly a good comparability between different samples. The measurement is rather fast with a single scan finished within a few minutes. Spectral information is only very limited, based on the available excitation laser and emission filter. The filter-based measurement is neccessary to provide the high sensitivity and the superior signal-to-noise through efficient suppression of scattered light in high-quality filters.

Considering that the size of individual features of high-density microarrays is close to the resolution border of the instruments, even higher resolutions can be necessary to evaluate the quality of a substrate to rule out, for example, structure formation of the surface layer. This can be achieved with fluorescence microscopy, even beyond the Abbe diffraction limit. Some microscopes, especially confocal laser scanning microscopes (CLSMs), are able to provide spectral information as well, but quantitative information is very difficult to obtain due to insufficient excitation intensity correction and differences in the focus position on different samples. Depending on the applied dyes and conditions, photobleaching due to the laser intensities is often limiting as well. For the present work, the microarray scanner is the instrument of choice, not only because microarray technology is significantly affected by surface functional group density as a performance parameter, but also as it offers unprecedented spatial homogeneity and scan-to-scan repeatability. A number of dyes and dye classes were applied for surface functional group determination, including Rhodamine dyes,[73,78,80,89], fluorescein isothiocyanate (FITC),[64,90] Cyanine,[91] Dansyl,[64,79] or BODIPYs[86]. One of the most prominent reporters is Fluram,[51,52,64,74,79] a well known label dye for primary amine groups (see Scheme 1.2).[92] The great advantage of this compound is that only the reacted state is fluorescent and

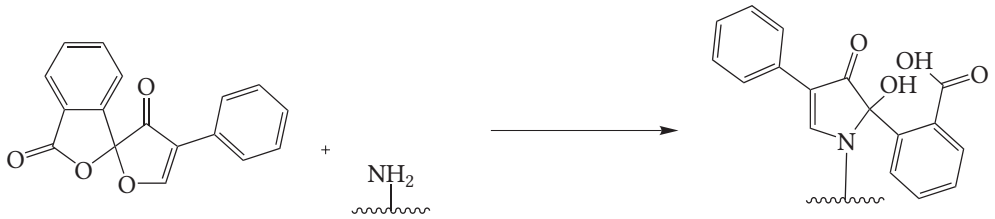

Fluram

Scheme 1.2: Reaction of Fluram with primary surface amino groups

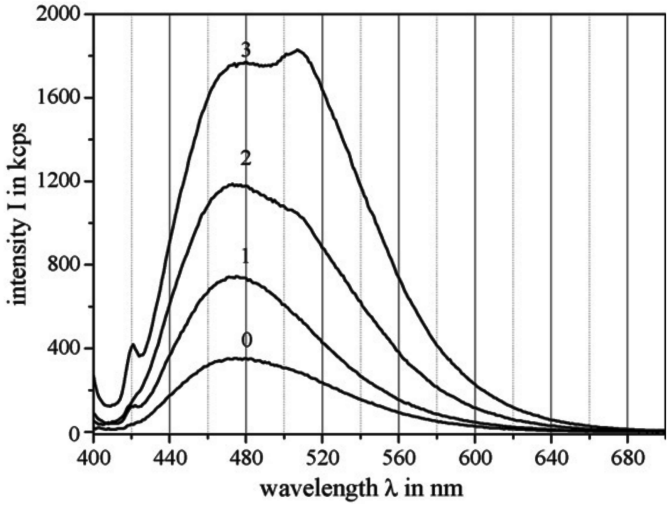

Figure 1.2: Fluorescence of Fluram on surfaces with increasing functional group density generated by dendrimer formation (the numbers indicate the dendrimer generation) (reprinted from ref. 79)

background fluorescence of non-specific bounded reporter dyes does not need to be taken into account. Holländer and his group performed a comprehensive analysis of the performance of Fluram, including a study on high density surfaces were they found that the occurrence of fluorescence quenching can easily be identified through changes of the emission spectrum (see Figure 1.2).[79]

Since absolute fluorescence measurement is intrinsically very difficult even for dilute solutions, different procedures for calibration were described for quantitative fluorescence measurements of dyes on surfaces: The common approach is to dry a defined volume of solvent with different dye concentrations on a defined surface area and determine the fluorescence intensities for the different concentrations.[86] The experience in this work is that this approach suffers from inhomogeneous layer formation and ill-defined surfaces areas. Ivanov *et al.* described a procedure where pieces of a non-reactive substrate with known dimensions were

incubated with the label dye and the fluorescence intensity was determined upon drying.[64] Subsequently, the dye was re-dissolved from the sample and the fluorescence intensity of that solution was measured to assess the contained dye concentration. Both methods are very difficult for dyes that change their fluorescence properties upon binding. Additionally, the assumption that loosely adsorbed and covalently attached, and therefore oriented, dyes show the same fluorescence properties was, to the best of my knowledge, never proven.

Apart from fluorescence measurements, determination of the photometric absorption of a dye on a surface is also possible. For the measurement of absolute amounts, photometry is usually the method of choice as it provides precise quantification and, in solution, high sensitivity. In contrast to fluorescence scanning, however, confining the dye from a volume onto a surface does not increase the sensitivity, since photometry is measured in a transmission configuration. Consequently, the layer thickness in Lambert-Beer's Law (Eq. 2.12) is reduced to an infinitesimal small layer and the sensitivity of photometry in solution is not recovered on surfaces. Two general methods are known to employ UV-vis spectrophotometry for surface functional group quantification: the direct method, were the dye-covered surfaces are measured directly,[86,93–99] and the indirect method, which involves cleaving the dye from the surface and measuring its absorption spectra in solution.[83,100–103] The direct method carries the advantage of involving fewer steps and being less prone to experimental errors, but can only be applied on substrates of high optical transparency, often functionalized on both sides to increase the amount of dye to be determined. Due to the higher surface density that can be reached, mostly small molecular labels are used, namely naphthyl derivatives[98] and *p*-nitrobenzaldehyde[93–95,97]. This limits, however, the applicability since these labels are UV absorbing, which interferes with several substrates like glass slides.[86] The indirect method on the other hand requires more surface to have enough dye released, yet, the substrates can often be further applied upon dye removal.

1.2.3 Time-of-flight secondary ion mass spectrometry

In time-of-flight secondary ion mass spectrometry (ToF-SIMS), the sample surface is bombarded in high vacuum with a focussed primary ion beam (typically gallium or bismuth ions or cluster ions) to produce secondary ions that are collected and analysed with a time-of-flight mass analyser. Generally, two modes are differentiated: dynamic SIMS, where the flux of the primary ion beam is high enough that the surface is notably sputtered, and static SIMS, where a low primary ion current is used and only a marginal amount of the surface is ionized. Given the low layer thickness encountered in surface functional group analysis, the latter is obviously the method of choice. Due to the analysis of molecules or molecule fragments, ToF-SIMS provides insight in chemical structures on the surface with significantly more detailed information than it is available from XPS alone. Especially in combination with gas cluster ion sput-

tering, very good depth resolution can be achieved, since only the top one or two nanometre are analysed.[104] Yet, secondary ion formation is prone to strong, hardly predictable, matrix effects, which renders quantitative ToF-SIMS very challenging.[105] Accordingly, the majority of surface functional group analysis employing ToF-SIMS uses the technique to acquire structural information instead of quantitative.[72,80,91,106] Only little research focussed on using ToF-SIMS in a quantitative manner.[97,107] A conceivable approach is to use ToF-SIMS analogue to FLOSS, only employing a label that provides a unique fragment with good linearity. The advantage of ToF-SIMS here is that its sensitivity is close to carefully performed fluorescence measurements, yet provides a higher dynamic range that overlaps with XPS. That should enable a combined XPS/ToF-SIMS analysis with chemical labelling to transfer the quantitative results of XPS on to the dynamic range of ToF-SIMS.

1.3 Dual-Mode labelling

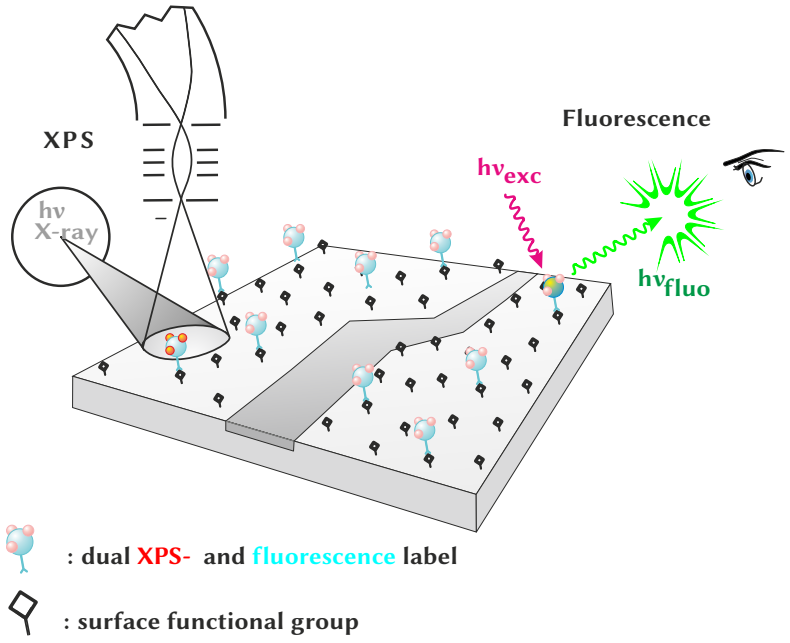

Figure 1.3: Dual-Mode labelling concept

The methods of CD-XPS and FLOSS both have their merits and pitfalls for quantitative surface functional group analysis, but stand separated from each other and results obtained with one technique offer limited comparability with results obtained with the other. This does not only originate from the different dynamic ranges of the methods that qualifies them for different samples, but also from the different sizes and binding chemistries of the employed labels.

A clear comparison of these two methods can only be reliably performed on one and the same sample with one and the same label. A label compound with the required properties, however, has not yet been presented for this purpose. Combination of CD-XPS with FLOSS would not only allow a simple comparison of the results, but also significantly enhance the available information. Currently, FLOSS suffers from a great unknown quenching influence that hampers the reliability of the method. If the content of the dye could be determined independently with a method that allows unequivocal interpretation, the effect of quenching could be identified and quantified. Additionally, given that the functional group can be clearly identified in its elemental contribution, like it is the case for amino groups on glass surfaces, the determination of the labelling ratio from XPS enables a reliable quantification of functional groups with incomplete labelling. A schematic overview of the concept is shown in Figure 1.3.

Accordingly, the route of this work guides towards the development of dual-mode labelling that additional to fluorescence invokes XPS as a method of quantification of dye and functional groups to provide the relevant information needed to calibrate the fluorescence intensity of the dyes on the surface in dependence of the functional group density. Such a calibration ultimately allows to perform quantification of surface functional groups via fluorescence measurement based on an (external) calibration via XPS with a reference dual-mode label.

1.3.1 Label design

The fundamental requirement for a novel dual-mode label is a specific and efficient binding to the surface functional group in question. To serve as fluorescent reporter, it obviously needs to show a notable fluorescence. To be widely applicable in different laboratories, this fluorescence should be compliant to parameters determined by commonly available laser excitation sources and fluorescence dyes, notable examples are fluorescein (λ_{Ex} = 488 nm; λ_{Em} = 500 to 550 nm), Rhodamine 6G (λ_{Ex} = 532 nm; λ_{Em} = 550 to 600 nm) and Cy5 (λ_{Ex} = 635 nm; λ_{Em} = 650 to 700 nm). The mentioned conditions are also employed in the available microarray scanner.

Those two properties of specific labelling and strong fluorescence are, and were, realized for numerous purposes, but it is the third main property that adds the challenge: The compound needs to be rich in a specific element for XPS-determination to allow true dual-mode labelling. Having a compound fulfilling these three properties would be sufficient to establish a method for dual-mode labelling. A number of additional properties is preferable but not initially necessary: The label should be uncharged to avoid ostensible binding by electrostatic interaction. It should be small in molecular size to reduce the steric limit on maximum binding. Water-solubility and applicability would ease wide-spread application. A change in fluorescence upon binding would be helpful to minimize unspecific read-out. Finally, economical considerations prefer an efficient and reliable synthesis. A number of common dyes has

been adopted to provide specific binding to functional groups in the context of bio-molecule analysis. As the surfaces in question are applied in the very same field, the relevant functional groups are the same and existing binding chemistry should be easily transferable. Closer examination of relevant elements with high XPS sensitivity and the possibility to be introduced in higher amounts into organic molecules reveals fluorine as the most promising element, since it can be introduced as a substitute for hydrogen in higher amounts than other elements like chlorine and bromine. Sulphur and phosphorus might be able to be introduced into organic fluorophores, but show limited sensitivity in XPS.

A small number of publications deals with fluorinated fluorescent dyes, mainly to enhance the photostability of such compounds.[109–111]

Fluorescein can be prepared with up to 22 at% fluorine (see Scheme 1.3),[108,109] but introducing a moiety for selective binding is then rather challenging and, more importantly, the fluorescence quantum yield of fluorescein is highly pH-depended,[112] which makes it unsuitable as surface functional group label. The labelled surfaces are scanned in the microarray scanner in air, without solvent, which makes control of the pH value inherently difficult.

Alternatively, Rhodamine derivatives can be considered since they are commonly employed as fluorescent probes.[113,114] They can be prepared with a significant fluorine content as well, but additionally including a reactive moiety that can be transferred into an amino group label.[110] However, expanding the applicability of the label is difficult and Rhodamine dyes are intrinsically charged which makes them prone to electrostatic interaction. The BODIPY dyes on the other hand are characterized by a unique versatility and robust photophysical properties,[115,116] rendering them the dyes of choice when a multitude of requirements has to be met. As Ulrich *et al.* point out in their comprehensive review, the BODIPYs came a long way from their initial application as laser dyes: Originally uncharged, they are unrivalled when hydrophobic fluorophores are required, but can be turned water-soluble with appropriate substitution like sulfunation or PEGylation, if an uncharged substituent is required. Accordingly, their

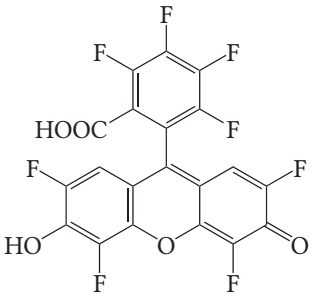

Scheme 1.3: Exemplary structure of highly fluorinated fluorescein (4,5,6,7,2',5',5',7'-octafluorofluorescein) from ref. 108,109

application today spans from staining of polymer beads via labelling of bio-molecules to light-harvesting antennas in organic solar cells.[115] The fundamental BODIPY structure is shown in Scheme 1.4. The synthesis of BODIPYs is mainly performed by condensing two pyrrole units with an aldehyde or acid chloride component to form the dipyrromethan which is subsequently oxidized to the dipyrromethene which itself is ultimately transformed to the BODIPY via basic complexation with $BF_3 \cdot OEt_2$. Here, already the starting material allows manifold variation of the resulting dye, since the synthesis accepts various structural modifications of both the pyrrole as well as the aldehyde/acid chloride component. In addition, numerous methods of post-modification are known and possible due to the high chemical stability of the BODIPY system. The synthetic possibilities were well summarized by Loudet *et al.*[116] In the context of surface functional group labelling, BODIPY dyes are favourable since they are net-neutrally charged, comparably photostable and generally very robust emitters with little dependence of the brightness on the surrounding environment. These effects are relevant since the samples are usually measured in a dry state, were the environment is governed by the surface and moisture layer and difficult to define or modify. However, commercial BODIPY dyes have only scarcely been used as surface functional group labels.[86] Additional to the fluorine atoms contained in the BODIPY core themselves, the fluorine content of BODIPYs can easily be increased by introducing a fluorinated *meso* substituent.[117–122] The work of Vives *et al.* suggests that BODIPY dyes containing a Pentafluorophenyl moiety,[117] which were also personally prepared in the preface of this work,[120–122] can even be directly employed as amino group labels (see Scheme 1.5).

Apart from their direct application as amino group labels, these dyes are promising as a platform for different functional group labels. Due to the easy substitution at the para position with amino or, even better, with thiol compounds, different linker moieties could be introduced. Since these occur after fabrication of the BODIPY and solemnly depend on the presence of the penta-fluorophenyl part, the remainder of the BODIPY system can be modified by applying

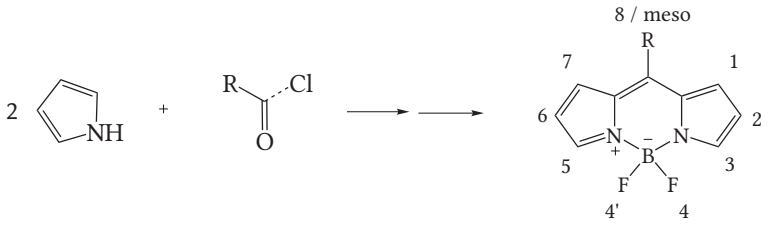

Scheme 1.4: Principal synthesis route and fundamental structure of the BODIPY core, including commonly used numbering of positions

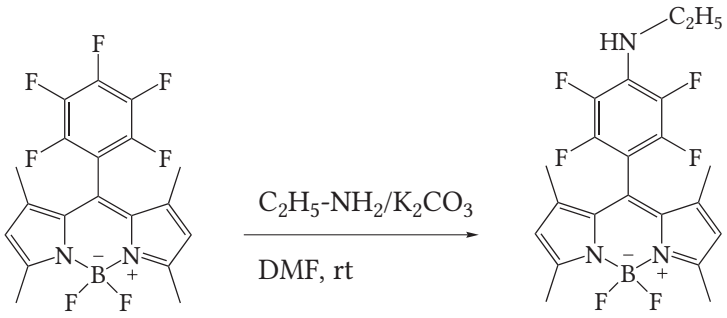

Scheme 1.5: Substitution reaction at the pentafluorophenyl moiety observed by Vives *et al.* (see ref. 117)

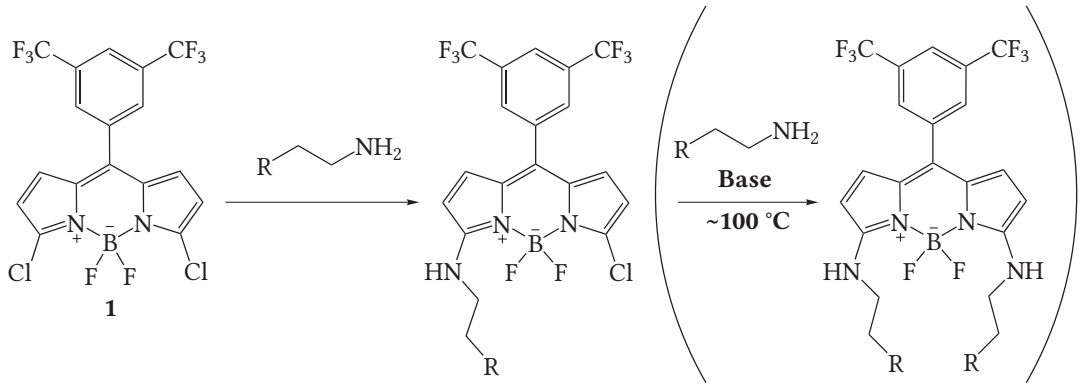

Scheme 1.6: Reaction of **1** with amino compounds, the part in brackets only occurs under drastic conditions

different pyrrole compounds to the synthesis. Apart from significantly increasing the fluorine content, such modification could also be used to alter the absorption and fluorescence properties and adjust the dye to fit certain instrumental needs without having to change the binding chemistry, or to transfer a calibration achieved with XPS for one target functional group to another by changing the linker.

An alternate reaction suitable for surface amino group labelling is the nucleophilic substitution of chlorine at the 3,5 position of the BODIPY core which is known to be very efficient for amino groups, as Boens *et al.* pointed out.[123,124] An advantage of this binding mechanism is that it directly effects the BODIPY core and provokes pronounced spectral changes which eases identification of proper binding. The compound **1** was designed and prepared by Mandy

Hecht alongside this work as an amino label with a fluorine content comparable to commonly employed XPS labels. Scheme 1.6 depicts the reaction of **1** with primary amino groups. As it is indicated, under standard conditions, only mono-substitution occurs. The substitution of the second chlorine atom is possible, yet requires significantly harsher conditions, like addition of base, the amino compound in high excess and elevated temperatures.[124]

2 Results and Discussion

2.1 Fluorinated BODIPY dyes as probes for surface functional groups

Parts of this section were published in ref. 88 and 125.

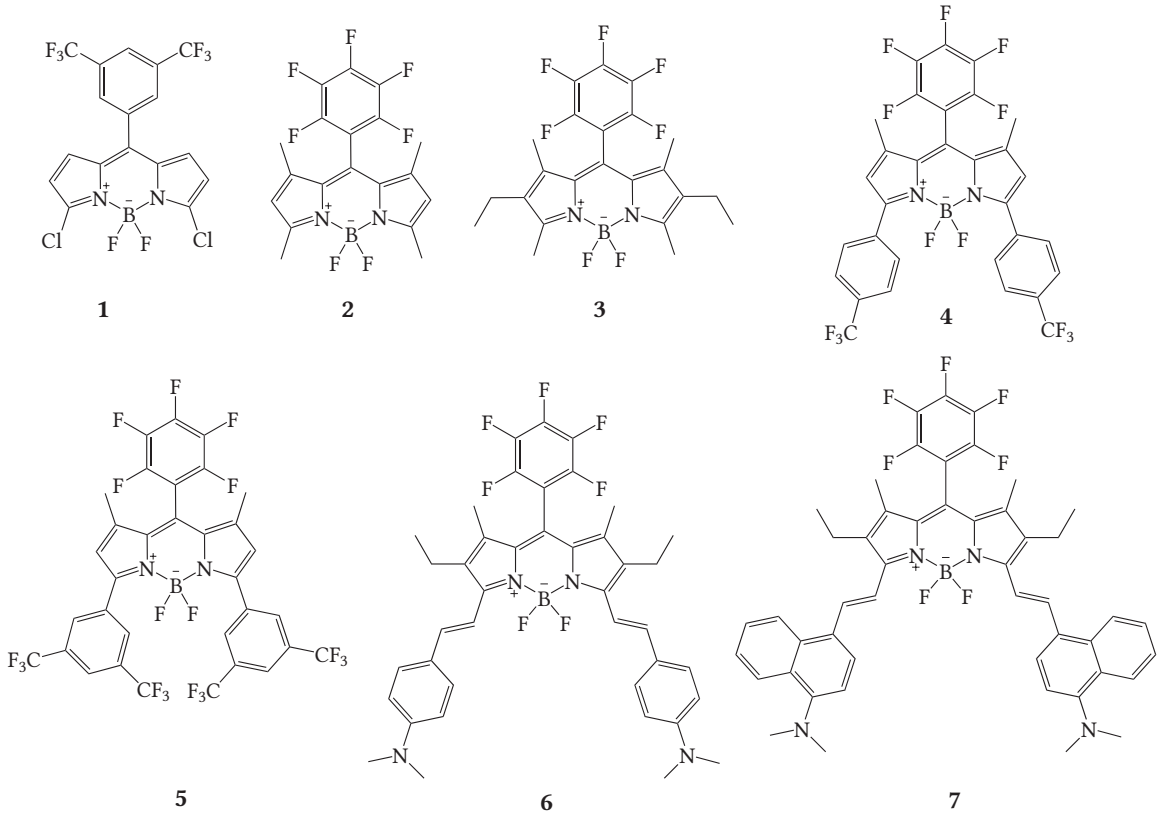

Scheme 2.1: Chemical structures of the compounds investigated in this work

Additional to the presented compound **1**, the dyes **2**-**7** were prepared to emphasize the versatility of the platform approach for functional group labelling. **3**, **6** and **7** are already known and presented prior to this work due to their enhanced photostability.[120–122] Additionally, **2** was prepared to widen the spectral range covered and to evaluate the work of Vives *et al.*[117] **4** and **5** resulted from a cooperation with TU Dortmund and were prepared there applying a novel gold catalysed cycloisomerization.[125] Prior to application as surface functional group labels, the spectral properties of all dyes were comprehensively characterized.

2.1.1 Optical spectroscopic measurements

Dye	Solv.	$\varepsilon_\lambda(10^4)$	λ_{abs} / nm	λ_{em} / nm	$\tilde{\nu}_{abs\text{-}em}$ / cm^{-1}	Φ_f	τ_f / ns	k_r / $10^8\ s^{-1}$	k_{nr}/ $10^8\ s^{-1}$
1	Hex		521	536	537	0.12	0.70	1.7	12.6
	Tol		525	544	665	0.38	1.96	1.9	3.2
	Bu_2O		521	536	537	0.16	0.98	1.9	8.6
	Et_2O		518	532	578	0.11	0.71	1.6	12.5
	THF		518	533	648	0.19	1.09	1.7	7.4
	MeCN	7.8	515	530	550	0.19	1.25	1.5	6.5
	EtOH		518	534	578	0.14	0.88	1.6	9.8
	MeOH		516	532	583	0.14	0.93	1.5	9.3
2	Hex		517	525	295	1.00	5.74	1.8	0.0
	Tol		521	531	361	1.00	4.98	2.3	0.0
	Bu_2O		517	525	295	1.00	5.51	2.0	0.0
	Et_2O		516	523	332	1.00	6.01	1.8	0.0
	THF		517	526	331	1.00	5.53	2.0	0.0
	MeCN	7.7	513	521	373	1.00	6.05	1.7	0.0
	EtOH		515	524	334	1.00	5.88	1.7	0.0
	MeOH		514	523	335	1.00	6.12	1.7	0.0
3	Hex		542	554	400	0.94	6.45	1.5	0.1
	Tol		547	560	456	0.96	6.23	1.7	0.1
	Bu_2O		543	555	398	0.94	5.58	1.5	0.1
	Et_2O		541	554	401	1.00	6.72	1.5	0.0
	THF		543	555	398	0,93	6.18	1.5	0.1
	MeCN	6.7	539	553	470	0.85	6.74	1.3	0.2
	EtOH		541	554	434	0.90	6.53	1.4	0.2

Dye	Solv.	$\varepsilon_\lambda(10^4)$	λ_{abs} / nm	λ_{em} / nm	$\tilde{\nu}_{abs\text{-}em}$ / cm^{-1}	Φ_f	τ_f / ns	k_r / $10^8\ s^{-1}$	k_{nr}/ $10^8\ s^{-1}$
	MeOH		540	553	435	0.89	6.69	1.3	0.2
4	Hex		558	588	914	0.86	5.36	1.6	0.3
	Tol		563	598	1040	0.95	4.75	2.0	0.1
	Bu_2O		559	590	940	0.93	5.14	1.8	0.1
	Et_2O		556	589	1008	0.93	5.48	1.7	0.1
	THF		557	593	1090	0.92	5.13	1.8	0.2
	MeCN	5.9	550	587	1146	0.94	5.57	1.7	0.1
	EtOH		555	586	953	0.86	5.25	1.6	0.3
	MeOH		553	587	1047	0.89	5.39	1.7	0.2
5	Hex		558	584	798	0.91	5.44	1.7	0.2
	Tol		566	595	861	0.93	4.88	1.9	0.2
	Bu_2O		560	587	821	0.89	5.26	1.7	0.2
	Et_2O		558	586	856	0.91	5.67	1.6	0.2
	THF		560	589	879	0.89	5.19	1.7	0.2
	MeCN	4.7	556	587	950	0.91	5.8	1.6	0.2
	EtOH		558	589	943	0.90	5.46	1.6	0.2
	MeOH		556	584	862	0.91	5.67	1.6	0.2
6	Bu_2O		723	762	776	0.29	1.67	1.7	4.3
	Et_2O		723	772	978	0.28	1.51	1.9	4.8
	THF		737	798	1084	0.15	0.94	1.6	9.1
	MeCN	7.5	739	849	1998	0.05	0.43	1.2	22.1
7	Hex		692	743	1010	0.23	1.39	1.6	5.5
	Bu_2O		697	770	1360	0.17	1.04	1.6	8.0
	Et_2O		694	780	1670	0.13	0.88	1.5	9.9
	THF		699	(830)	2373	0.06	0.40	1.5	23.5

Table 2.1: Selected spectroscopic data of **1**-**7** in various solvents at 298 K, the uncertainty of Φ_f is typically ±0.01 and the one of ε_λ ±3000

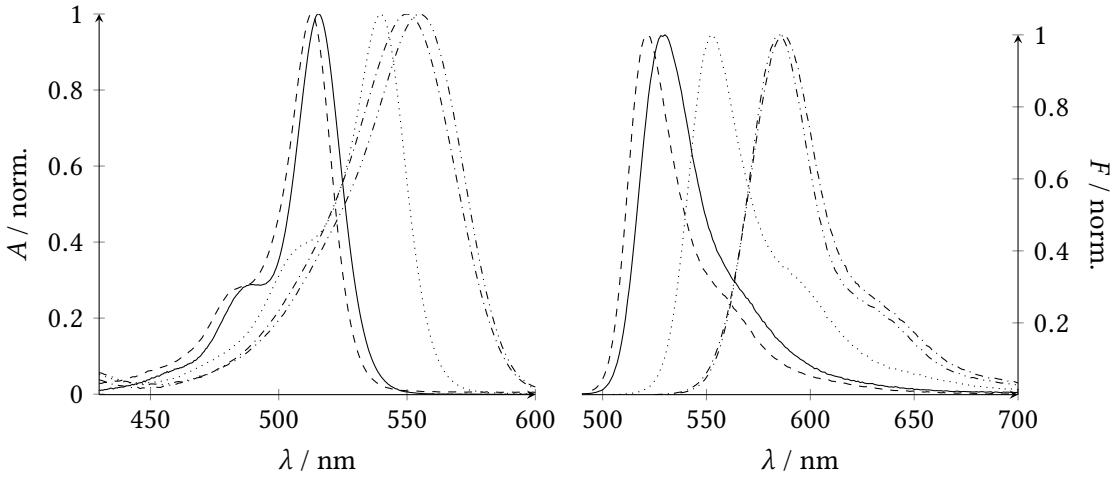

Figure 2.1: Absorption and emission spectra of **1** (——), **2** (- - -), **3** (·····), **4** (-·-·-) and **5** (-··-··) in MeCN

A comprehensive analysis was performed including determination of the fluorescence quantum yields Φ_f, fluorescence lifetimes τ_f and spectral maxima for the compounds **1**-**7**. The results are listed in Table 2.1. It can be seen that electrostatic effects such as an enhanced dipole moment of the 1,3,5,7-tetramethyl compared with the 1,3,5,7-tetramethyl-2,6-diethyl BODIPY core lead to a more ionic nature of the 1,3,5,7-tetramethyl core and slightly blue shifted absorption bands of **2** compared to **3** and **1**. The fluorescence quantum yields Φ_f are strongly affected by the meso-substituent. In the case of **2**, it is virtually 1 for all solvents, whereas Φ_f of the meso-phenyl analogue varies around 0.6.[126,127] This can be explained by the strongly restricted rotation of the pentafluorophenyl moiety by the *o*-fluorine atoms additional to the 1,7-methyl groups. The crystal structures show almost orthogonal orientation of the phenyl substituent for all the dyes bearing the 1,7-methyl groups and the pentafluorophenyl moiety.[88] For **1**, which does not possess the latter, the dihedral angle between the BODIPY core and the phenyl moiety amounts to only ca. 60°, indicating a partial conjugation of meso-substituent and BODIPY core and a higher rotational freedom. The first is supported by the bathochromic shift of the spectra compared to its 1,3,5,7-tetramethyl analogue and the latter by the lower fluorescence quantum yield of <0.2, which is consistent with the higher k_{nr}.[88] Compared to their parent dye **2** that carries methyl groups instead of the trifluoromethylphenyl residues on the 3,5-positions, the absorption maxima of **4** and **5** are shifted by ca. 40 nm and the absorption bands are significantly broadened. The Stokes shifts are increased from ca. 300 to 1000 cm^{-1}. In view of the colour rules for BODIPY π-system substitution, these changes can be attributed to the extension of the fluorophores' π-system with the additional trifluorophenyl moieties and their enhanced rotational freedom.[128] The comparatively small spectral differences between **5** and **4** despite the introduc-

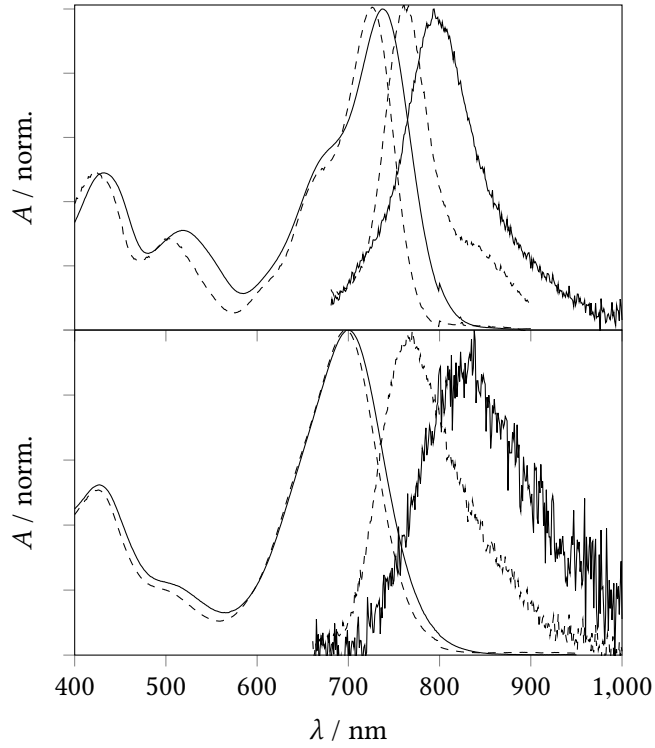

Figure 2.2: Absorption and fluorescence spectra of **6** (top) and **7** (bottom) in Bu_2O (- - -) and THF (——).

tion of two additional CF_3 groups in the first one are tentatively ascribed to the enhanced steric hindrance in the case of 3,5-phenyl substitution on the BODIPY core.[129] That results in considerable (average) torsion angles and hence reduced electronic coupling between the BODIPY core and phenyl rings, diminishing the electron withdrawing effect of these substituents. The quantum yields Φ_f of **4** and **5** are only slightly reduced compared to **2**, most likely due to enhanced vibrational de-excitation via the 3,5-phenyl moieties, and the fluorescence lifetimes τ_f only change slightly. Elongation of the π-system by attachment of styryl substituents at the 3,5-positions rather than phenyl moieties affects the spectral characteristics of the dyes by shifting the absorption and emission maxima to even longer wavelengths (Figure 2.2).[130–133] In the case of **6** and **7**, the shift compared to **3** is significantly larger as compared to **2** and **4**/**5** with values of +140 and +200 nm, depending on solvent polarity (Table 2.1). Similar effects have been observed before for doubly (*N,N*-dimethylamino)styryl-substituted BODIPYs.[130] Moreover, not only are the band positions solvatochromically shifted but the fluorescence quantum yields are affected as well, resulting in a gradual decrease of Φ_f as the polarity of the solvent increases. Apparently, the charge-transfer character from the terminal electron-donating dimethylamino

groups to the more electron-deficient BODIPY core is enhanced in polar solvents. Although one would perhaps expect a stronger displacement to the NIR for **7** compared with **6**, because the naphthenyl moieties should provide enhanced π electron delocalization, the opposite effect is observed. The latter is tentatively ascribed to the higher steric demand of the naphthenyl moieties which decreases the degree of planarity within the two naphthostyryl extensions. Although, unfortunately, all attempts to grow crystals of **7** suitable for X-ray structural analysis failed, quantum chemical calculations provided further insight into the molecular peculiarities of **6** and **7**. Whereas the dihedral angles between the BODIPY plane and the meso-substituent differ by only 0.4° and the angles between the two pyrrole units of the BODIPY core by only 0.8°, the average angle between the styryl extensions and the BODIPY core is much higher in modelled **7**, (41.8°) compared with modelled **6** (23.6°) as is the angle between the two styryl extensions, 33.0° for **7** vs 20.2° for **6**, details can again be found in ref. 88. Another noteworthy difference are the significantly larger Stokes shifts of **7** compared to **6**, which is likely to arise from an in-plane rotation of the naphthenyl moieties in the excited state, strengthening π-conjugation and therefore lowering the energy of the excited state (Figure 2.2).

2.1.2 Photostability

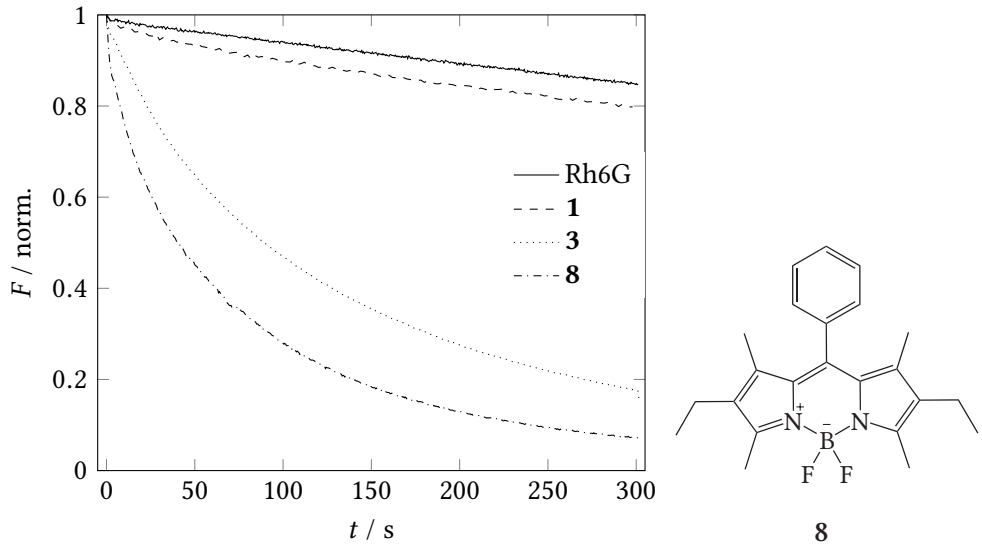

Figure 2.3: Relative fluorescence intensity decay profiles of Rh6G, **1**, **3** and **8** in MeCN under intense laser irradiation (λ_{Ex} = 532 nm, P = 0.2 W) and structure of reference compound **8**

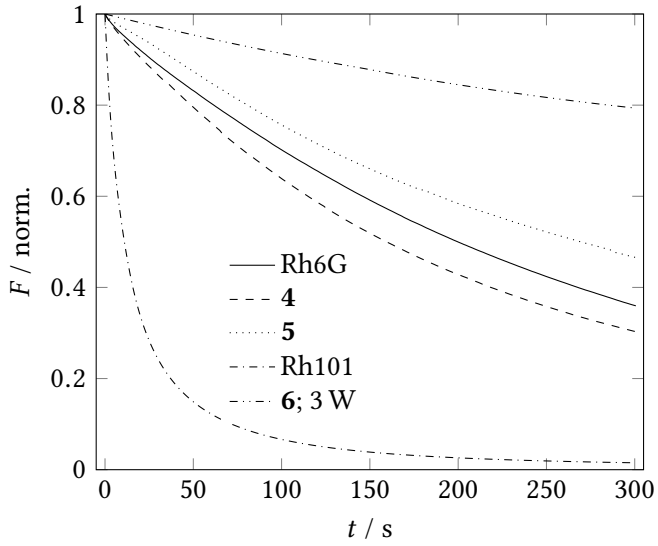

Figure 2.4: Relative fluorescence intensity decay profiles of Rh6G, **4**, **5**, Rh101 and **6** in MeCN under intense laser irradiation (λ_{Ex} = 532 nm, P = 1 W; **6**: P = 3 W)

As the fluorine substitution at the meso-phenyl group is supposed to equip the dyes with an increased photostability, **1** and **3** were compared to **8** and Rh6G under intense laser irradiation conditions, as these two are the most interesting structural and/or spectral competitors (Figure 2.3). **4** and **5** were additionally compared to Rh101, as this dye is the closest spectral match of commercial importance (Figure 2.4). The laser power for irradiation was selected to achieve a notable bleaching in all cases. The absorption of the dye solutions was adjusted to $A_{532\,nm}$ = 0.1 which means the photostability is a comparison of stability per photons absorbed in solution. This approach is sufficient to judge the application of the dyes since all the solutions have a similar brightness. It is noteworthy that the relative photostability of a dye solution is highly concentration depended and the measured stability is not "per photon absorbed per dye". **6** showed most remarkable photostability and was measured unrivalled at P = 3 W. (Figure 2.4). Dye **3** showed increased photostability compared to its non-fluorinated analogue **8**, as it is expected upon fluorination, but is exceeded by **1**. The latter also shows a significantly shorter fluorescence lifetime (6.7 vs 1.3 ns) which could explain the higher photostability, as less time is spent in an excited state. A comparable explanation, together with the increased structural stability through the large π-system, leads to the extreme photostability of **6**.

2 could not be measured with the available photostability setup, as this dye shows only marginal absorption at 532 nm. Its elongated analogues **4** and **5** on the other hand, show strong absorption at 532 nm and high photostability, although the long fluorescence lifetimes of around 6 ns are retained. As shown in Figure 2.4, the photostability shows differences between **4** and **5** with **5** being even more photostable than Rh6G and **4** slightly less. This is consistent with the expected increase in photostability with increased fluorination. Both dyes are significantly more photostable than Rh101, but spectrally nearly identical to Rh101, irrespective of the environment, which renders them promising substitutes for Rh101 and other Rhodamine dyes in given applications, other than surface labelling. Especially their high lipophilicity makes them ideal candidates not only for particle doping, but also for membrane staining experiments.

2.1.3 Labelling of surface functional groups

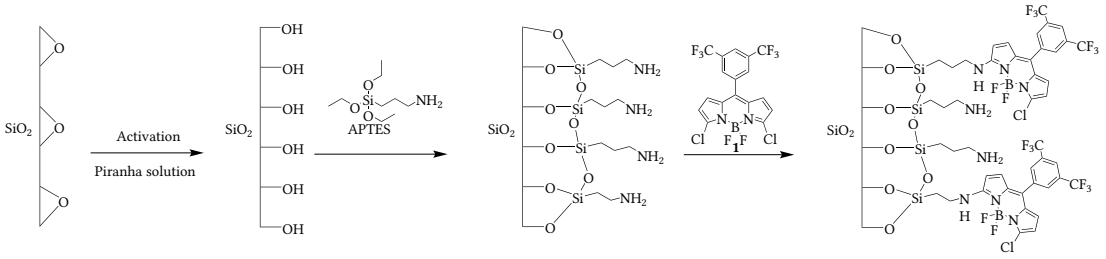

Scheme 2.2: Simplified surface reaction scheme for the activation of the glass surface, the treatment with APTES and the subsequent labelling using a label dye

Based on the work of Boens *et al.*,[123,124] **1** should provide a reliable surface label for amino groups which can be directly applied in solution, whereas the results presented by Vives *et al.* suggests **2** and **3** show amino and thiol binding in basic conditions.[117]

To establish the fundamental binding properties, a set of comparably functionalized slides is required. In a first attempt, activated glass surfaces where dipcoated in a silane solution (10 % in ethanol) containing either APTES (sample **AA**, all full list of all slide samples can be found at the end of this work at page 149) or (3-mercaptopropyl)trimethoxysilane (MPTMS) (sample **AB**), rinsed with ethanol (EtOH) and finally cured at 120 °C. One slide of each silane was either placed in 0.2 mM solution of **1** in MeCN or in a 0.2 mM solution of either **2** or **3** with a small amount of K_2CO_3. A simplified scheme for the surface reactions using the example of APTES and **1** is shown in scheme 2.2. After reacting for 24 h, the slides were carefully

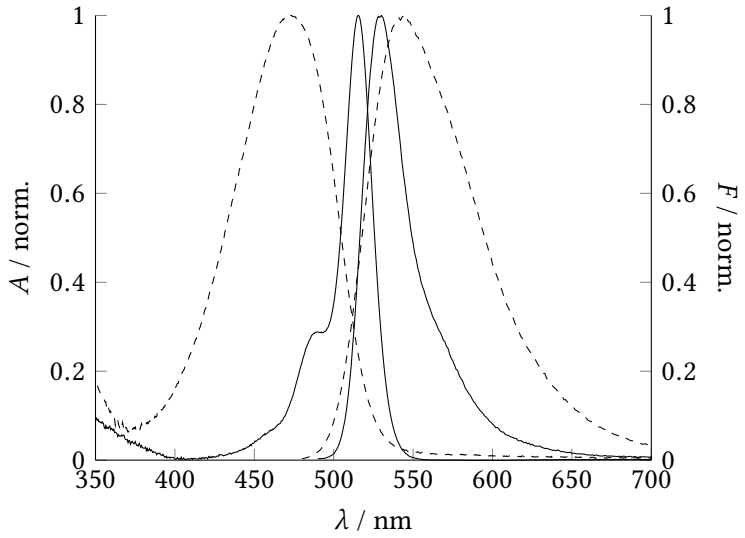

Figure 2.5: Absorption and emission spectra of **1** (——) and the reaction product of **1** and APTES (mono-substitution, - - -) in MeCN, λ_{Ex} = 480 nm

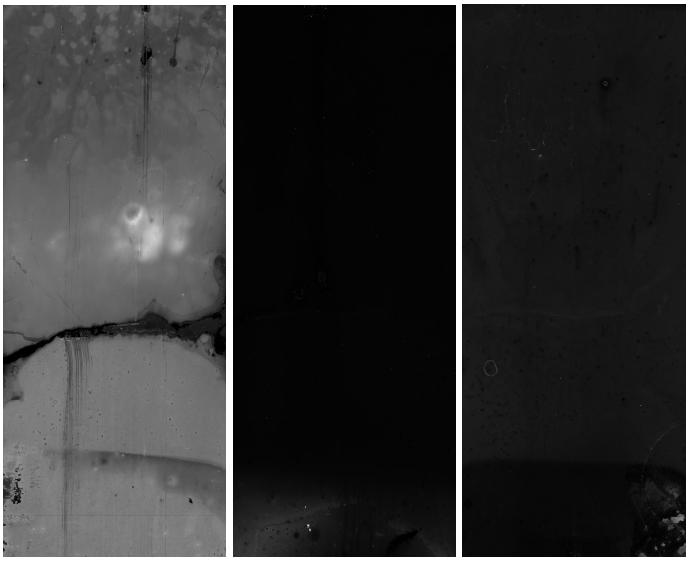

Figure 2.6: Visual comparison of amino surfaces labelled with **1** (left), **2** (middle) and **3** (right), λ_{Ex} = 488 nm for **1** and **2** and 532 nm for **3**, note that intensities do not scale

rinsed, dried and analysed using the fluorescence scanner. Unfortunately, the scans revealed that the manufactured surfaces are very heterogeneous and the results allow only qualitative comparison. Neither **2** nor **3** showed significant binding as to surface amino groups, in contrast to **1**. Apparently, the susceptibility of the pentafluorophenyl moiety for a nucleophilic attack is not high enough to allow high-yield reaction with surface-bound amino groups.

1 combines five main advantages over previously reported substances for a quantitative and sensitive surface group analysis, i.e., two amino-reactive chlorine moieties at the 3- and 5-position of the dipyrrin core which can undergo a mono-substitution reaction with nucleophiles under mild reaction conditions, a suitable amount of fluorine atoms (21.6 at%) for quantitative assessment by XPS, a reasonable brightness for rapid analysis via fluorescence scanning, an absorption band well within the excitation range of commercial fluorescence scanners and a change in its absorption and fluorescence maxima as a consequence of exchanging a chloro group by an amino group after a successful labelling reaction.[134] As can be seen in Figure 2.5, reaction of **1** with a primary alkylamine results in a significant hypsochromic shift of the absorption band and a bathochromic shift and broadening of the emission band.

2.1.4 Vapour deposition

2.1.4.1 Fluorescence analysis of slides

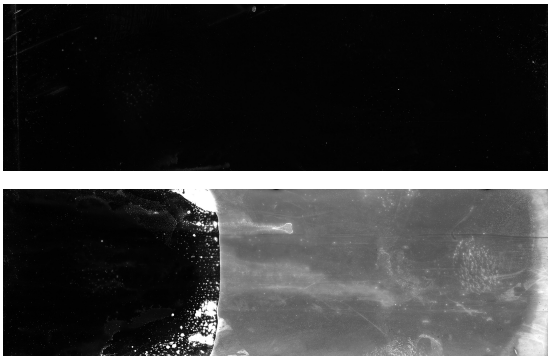

Figure 2.7: Scan images of amino-functionalized slide (**AC**) prior to (top) and after reaction with **1** (**AC1**) (bottom; the part of the slide shown on the left was not functionalized to facilitate handling) as described in the text; λ_{Ex} = 488 nm, λ_{Em} = 550 to 600 nm (standard green filter in emission), PMT voltage = 500 V

More detailed understanding of the binding properties on a surface requires a reliable fabrication of silane layers. According to literature, the VD from dilute vapour is the superior method to produce homogeneous silane films on glass surfaces.[78,91,95,103,135] Following the procedure from Xiang *et al.*,[95] activated and carefully dried slides were incubated with 100 µL of APTES solution (10 % in toluene) at 140 °C for 3 h, followed by careful rinsing with acetone, ethanol and water (slides **AC**). Slide **AC1** was incubated with **1** following the previous procedure (see section 2.1.3).

Fig. 2.7 compares the resulting slides prior (slide **AC**) and after (slide **AC1**) reacting with **1**. Compared to the dip coated slide **AA**, the homogeneity increased significantly and the fluorescence signal obtained on **AC1** can clearly be allocated to the successful labelling procedure. Given a working range of 300 to 800 V of the scanner's photomultiplier tube, the parameter used for the present measurements (500 V as indicated in the caption of Figure 2.7) makes it obvious that not only the labelling procedure yields rather uniform surface coverage but that the approach realized here leaves enough room for higher and lower signal intensities, i.e., changes in dye concentration.

However, a single point determination of the fluorescence intensity is insufficient to judge the potential of **1** as a quantitative XPS and fluorescence label. To adjust the surface contents of amino groups, the fabrication was modified by using 50 and 200 µl (slides **AE** and **AF**, respectively) of the silane solution for the vapour deposition, in hope that the change in concentration will lead to a variation in surface functional group density. The resulting slides were again reacted with **1** following the known procedure and subjected to careful analysis by fluorescence and XPS. For unequivocal allocation of the data, a number of references were used: a slide with silane but without **1** (**AC**) and piranha activated glass slides without silane treatment, but with (slide **AD1**) and without (slide **AD**) being subjected to **1**. The comparison of **AD1** and **AD** provides a measure for the amount of unspecific binding of **1** to a bare support and for the quality of the washing/drying process. Table 2.2 collects the relevant fluorescence data retrieved from the scans of those samples. In line with the previous experiments, the significant increase upon labelling with **1** is evident, the references without **1** show only very minor background

Table 2.2: Fluorescence intensities (F) of investigated slides, observed at λ_{Ex} = 488 and 532 nm, λ_{Em} = 550 to 600 nm

F_{exc}	bare glass	APTES	APTES + **1**(I)	APTES + **1**(II)	**1**
	AD	**AC**	**AE1**	**AF1**	**AD1**
F_{488}	17(17)	35(23)	23 255(3803)	12 740(935)	194(82)
F_{532}	12(10)	11(12)	7416(991)	5395(268)	72(38)

signal. Noteworthy is the very minor increase in fluorescence on the silane-free reference surface upon exposure to **1** which clearly suggests a specific binding of dye **1** to surface amino groups rather than an unspecific electrostatical binding to the surface. The change in fluorescence intensity is opposed to the expectation, e.g. an decrease is seen albeit the amount of surface functional groups is supposed to increase. To achieve a clear understanding, a technique like XPS, that is insensitive to signal saturation, yet still surface sensitive, is required.

2.1.4.2 XPS analysis of slides

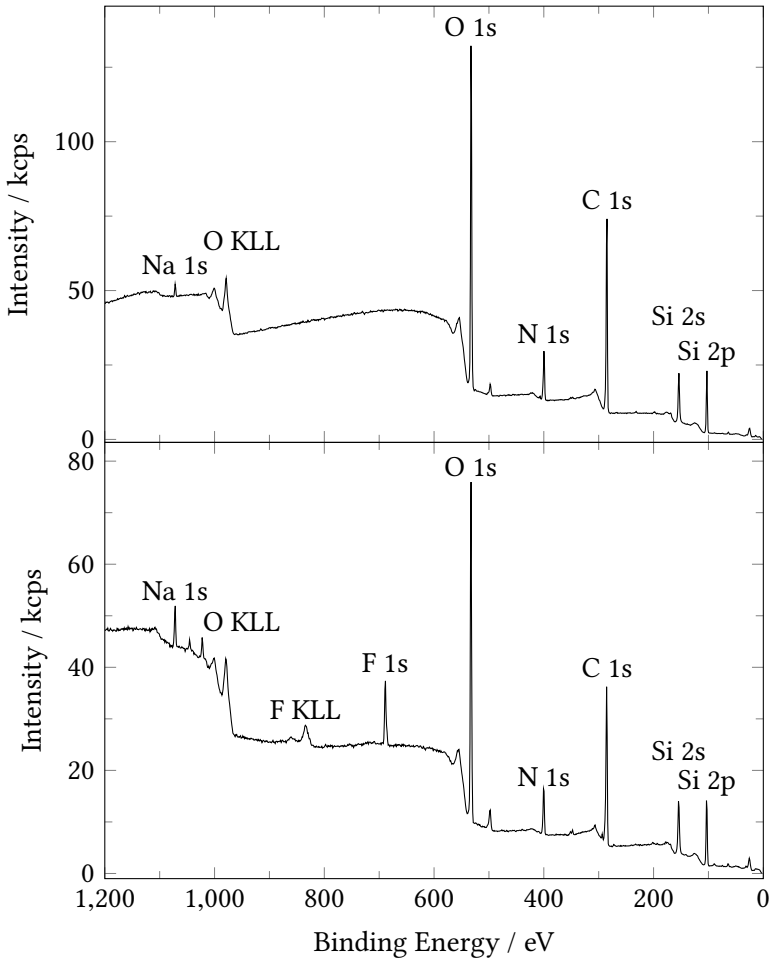

Figure 2.8: XPS survey scan spectra of the dye-covered area of the slides shown in Figure 2.7, amino-functionalized slide prior to (slide **AC**, top) and after reaction with **1** (slide **AF1**, bottom, high-resolution F 1s core level spectra are shown in Fig. 2.9) as described in the text

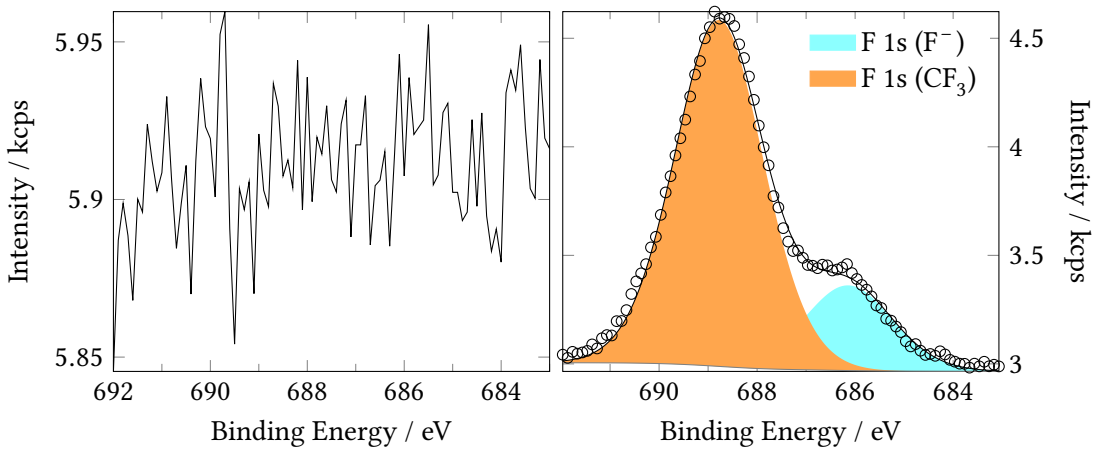

Figure 2.9: F 1s core-level scan spectra of the samples surveyed in Figure 2.8, amino-functionalized slide prior to (slide **AC**, right) and after reaction with **1** (slide **AF1**, left)

XPS analyses were employed on the same slides to quantitatively evaluate the different derivatization steps. Through the assessment of atomic ratios and atomic concentrations (at%) by this elemental analysis technique, it is possible to determine for instance the entire nitrogen or fluorine content introduced by functionalization with APTES and subsequent reaction with a dye such as **1**. On the basis of the labelling reaction depicted in scheme 1.6 , the amount fraction of carbon atoms containing amino groups $[NH_2]_C$ which are reactive towards **1** can be derived from the fluorine content according to eq. 2.1.[54,56,61,136–139]

$$[NH_2]_C = \frac{[F]}{8[C] - 17[F] \cdot 100} \tag{2.1}$$

Eq. 2.1 follows from the generalized mass balance law $-(CH_2)_3-(NH_2)_y + y(CF_3)_2C_6H_3(C_9H_4BF_2N_2)Cl_2 \longrightarrow HCl + C_{3+17y}N_{1+2y}F_{8y}B_yH_{14+7y}Cl_y$ of the reaction under consideration of $y = [F]/8, x = [C] - 17y$, and eq. 2.2. Table 2.3 lists representative XPS results, figure 2.8 shows the corresponding XPS scans.

$$[NH_2] = \frac{n_{N(NH_2)}}{n_{C,APTES}} = \frac{y}{x} \cdot 100 \tag{2.2}$$

The XPS results of the Piranha-activated (slide **AD**) and the dye-treated, washed substrates

Table 2.3: XPS elemental composition of investigated slides in at% and relevant atomic number ratios; EC = elemental composition and atom number ratios; Slide **AF1** was observed at an electron emission angle of 60° and 0°

EC	bare glass	APTES	APTES + **1**(I)	APTES + **1**(II)	APTES + **1**(II)	**1**
	AD	**AC**	**AE1**	**AF1**(0°)	**AF1**(60°)	**AD1**
C	6.9	51.3	42.7	44.4	51.4	9.2
N	0.6	7.4	7.1	7.2	8.4	1.1
O	69.1	28.1	30.4	28.3	21.4	67.0
Si	23.4	13.2	16.7	15.3	10.6	22.7
F	-	-	3.0	4.8	8.1	-
N/C	0.09	0.14	0.17	0.16	0.16	0.12
C/Si	0.30	3.89	2.56	2.90	4.85	0.41
N/Si	0.03	0.56	0.42	0.47	0.79	0.05

(slide **AD1**) present high amounts of silicon and oxygen that are specific for the glass substrate, as well as other glass ingredients (Ca, Zn, Mg, Al) and small amounts of organic (hydrocarbon) contaminations (originating from incomplete substrate cleaning and impurities adsorbed during handling from solution and environmental air). In line with an only slightly enhanced fluorescence from slide **AD1** compared with slide **AD** (Table 2.2), which might either be due to traces of adsorbed **1** or due to slightly enhanced scattering because of the deposition of unspecific organic material on the support during the processing, these results suggest that unspecific adsorption of **1** is negligible.

The content of the carbon and nitrogen components increased significantly after functionalization with APTES to generate amino-terminated surfaces (slide **AC**). High-resolution spectra of the N 1s region exhibit two components at 399.4 and 401.1 eV, corresponding to amino groups (NH_2) and their tightly electrostatically bound ammonium counterparts ($NH_3^+\cdots X^-$), which lie at energies between the more common hydrogen-bonded and protonated amino groups.[137,140]

After the labelling process, a new fluorine peak with two components at 688.5 and 686.2 eV related to the CF_3 and BF_2 moieties of bound dye is detected in the survey and high-resolution XPS spectra for slides **AE1** and **AF1** (Figures 2.8). The presence of fluorine containing groups can be verified independently by a new CF_3 component at 293.3 eV in the high-resolution C 1s core level spectra after treatment of the APTES-functionalized slide with **1**. These fluorine-related signals were absent on the reference supports (**AD** and **AD1**). In addition, traces of approx. 0.2 at% of chlorine could be detected for the APTES+**1** slide **AF1**, supporting the successful labelling step. Along with the fact that the **1**-tethered slides show spectral features

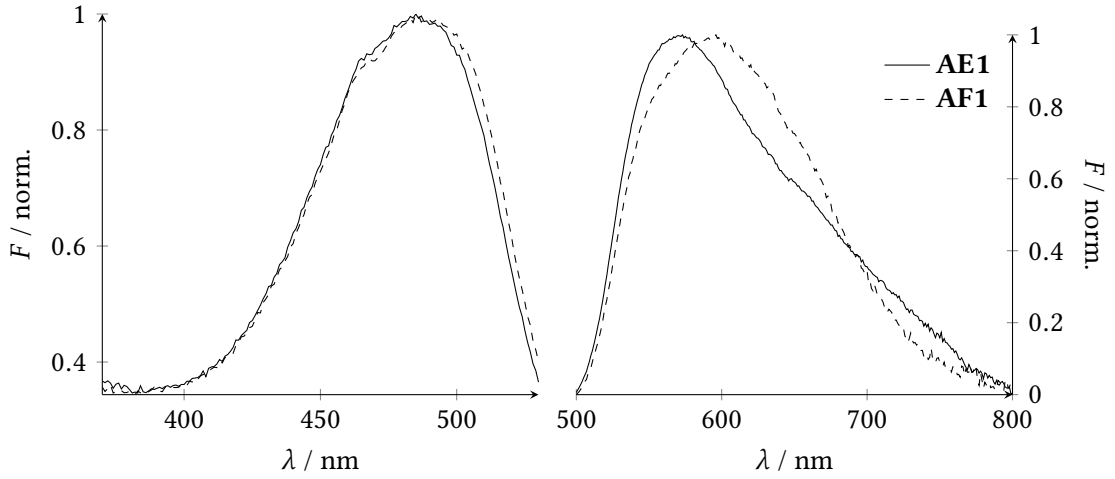

Figure 2.10: Fluorescence excitation (λ_{Em} = 590 nm, left) and emission scans (λ_{Ex} = 466 nm, right) of slide **AE1** and **AF1**

of the mono-substituted reaction product between **1** and APTES, compare absorption spectra in Figure 2.5 and fluorescence excitation spectra in Figure 2.10, these chlorine traces by XPS support the presence of only the mono-substitution product on the slide. The absence of the fluorine peak in the case of slide **AD1** suggests that an activated glass slide without amino moieties is unable to react with **1** when incubated for 24 h at room temperature, despite the fact that nucleophilic hydroxyl groups are present on the surface of the plain activated SiO_2 supports, which is again supported by the respective fluorescence scanning results of slide **AD1** in Table 2.2. Moreover, the data listed for slide **AF1** at 60° electron emission angle in Table 2.3 (slide **AF1**(60°)) further show that the amount of fluorine atoms attached to the outermost layer of the APTES film increases significantly to approx. 8 at% when measured in a more surface-sensitive mode to suppress substrate signals (Si and O). If we assume that the amino group density achieved under the high-loading deposition conditions as employed here amounts to ≥3 molecules per nm^2,[95,141] the concentration of labelled amino groups derived from slide **AF**60° data according to equations 2.1 and 2.2 of $[NH_2]_C$ ~3 % indicates that approx. 9×10^{12} NH_2 groups per cm^2 have been successfully labelled with **1**. Considering that based on the van der Waals radii of common organic dye molecules such as Rhodamines or BODIPYs the theoretically achievable surface coverage amounts to 2.5×10^{13} per cm^2,[86] the present labelling ratio of only approx. 3 % suggests that the high-loading deposition procedure adapted from ref.[95] indeed produces APTES films which are thicker than a monolayer. Such a behaviour has been reported before for APTES and other deposition techniques.[91,94] Apparently, the opposed trends found in the XPS and fluorescence results above, i.e. a decrease in fluorescence intensity upon going from slide **AE1** to slide **AF1** yet a slight increase in fluorine content

indicates that more dye molecules undergo unspecific interaction with the thicker APTES film on slide **AF1** or interact with each other, leading to self-quenching effects. This is supported by the differences in fluorescence signals obtained from 488 and 532 nm excitation in Table 2.2 as well as by the red-shifted fluorescence spectra of slide **AF1** (Figure 2.10), longer wavelengths usually leading to preferred excitation of dye species which are energetically stabilized through interaction with the surface or other dye molecules.[142]

2.1.5 Conclusion

These experiments prove the feasibility of dual-mode labelling of surface functional groups. The obtained fluorescence signals are well within the linear range of the employed fluorescence scanner and the fluorine contents found on the sample are significantly above the limit of detection for fluorine in XPS (0.1 at%).

Yet, these measurements point ot a problem in the determination with fluorescence, although the fluorescence intensity is instrumentally well within the linear range, it appears that the linear range of the fluorescence method using label **1** is exceeded as strong indication of fluorescence quenching due to a high fluorophore density was found.

The employed surface preparation method was found to depend on the amount of silane applied. Upon closer consideration, this result disagrees with the suggested mechanism of the dry vapour deposition, where due to the absence of significant amounts of water, only surface hydroxyl groups are available to react with the silane and no condensation that promotes multi-layer formation should occur. However, especially APTES is well known in the literature for its complicated binding chemistry, involving e.g. self-catalysis of binding and hydrolysis.[42,66,78,91,135,143,144] Even the nearly unavoidable amounts of surface bound water might be sufficient to induce multi-layer formation. The goal of a reliable reference surface system is obviously not yet met, but understanding the fluorescence intensity changes of the surface label **1** necessitates a controlled preparation of surfaces with defined densities of surface functional groups. To meet this requirement, the methodology used to characterize the manufactured surfaces needs to be expanded.

The label dye candidates **2** and **3** could not be straightforwardly utilized as fluorescence labels due to apparently insufficient binding. Yet, the available library of compounds containing the reactive pentyfluorophenyl moiety is very promising as a platform system for various surface labels with comparable binding properties, but different spectral properties. Further functionalization of the meso substituent with linker components capable of selective surface functional group binding is strongly expected to yield highly versatile label dyes.

2.2 Towards reference surfaces with controlled surface functional group density

2.2.1 Relevant substrates

As unravelled in the previous section, the formation of amino silane layers on glass does not follow a straightforward mechanism. Yet, since the results obtained do not allow to clearly understand and judge the performance of **1** as a dual-mode surface functional group label, a refined process to prepare surfaces with controlled functional group densities are urgently required.

The common choice in the preparation of true self-assembled monolayers (SAMs) is the deposition of long-chain thiols on gold.[145] These are known for their defined layers and allow the formation of varying functional group densities by changing the ratio of thiols in the preparation.[146] However, gold surfaces are known for quenching the fluorescence of dyes in their vicinity and accordingly unsuitable for fluorescence intensity based assays.[147]

Organic polymer based substrates received increased attention due to their easy manufacturing and robustness, but are unfavourable here since they depend on plasma activation, which results in rather undefined functionalizations.[32,50,55,57,59,106,148,149] They also pose pronounced problems in XPS analysis, since the surface cannot be distinguished from the bulk material.[139] Additionally, those substrates are only of limited stability against organic solvents and even minimum swelling might be sufficient to incorporate label dye molecules unspecifically and render the fluorescence analysis useless. Accordingly, glass slides functionalized with silanes were selected as candidates for the required reference surfaces. Advantages of glass as substrate material are its sufficient flatness, rigidity and transparency, together with reliable and cost-efficient availability. Since the material is non-porous and does not swell, unspecific dye attachment is only relevant at the interface. The manifold of silanes available offers fabrication of differently functionalized surfaces following the same protocol and the resulting layers are of good chemical stability, especially towards organic solvents and elevated temperatures. Numerous commercial suppliers offer glass slides composed of different types of glass with numerous functional groups, including amino, aldehyde, carboxyl or mercapto groups. Since the glass contains mainly silicon dioxide with additions of different alkali- and alkaline earth salts, whereas carbon, nitrogen and fluorine are only contained in traces, the contribution to the surface layer of the latter can individually be analysed without having to consider the bulk.

As silane chemistry is comparable for different silicon dioxide surfaces, the glass can be substituted with materials like quartz and surface oxidized silicon wafer if special requirements have to be met. The significant drawback for glass substrates is the silane chemistry which, despite being extensively investigated, is not fully understood and difficult to predict.

2.2.2 Fundamentals on silane layer formation

Numerous methods are available for the fabrication of such silane layers. Wang *et al.* provided a comprehensive comparison of four different methods for amino silane layer preparation from APTES:[78] The deposition from the vapour of diluted and concentrated silane and the solution phase deposition from an organic and an aqueous phase. Both the deposition from a concentrated vapour and from organic solution was found to yield thick layers of silane, well above a monolayer, although the functional groups in those layers seemed to be of better availability in the case of the concentrated vapour deposition. The dilute vapour was found to produce the smoothest film with acceptable thickness and good accessibility and the aqueous solution also thin and smooth films, yet with a very low density of functional groups. These findings point to different natures of silane layer formation, depending on the reaction conditions. The main influential parameters are the temperature and the humidity. The presence of water promotes the hydrolysis of the Si–X (with X being Cl or OR) to Si–OH. This hydrolysis is required for the silane to effectively coordinate via hydrogen-bonding to the Si–OH/Si–O^- groups on the glass surfaces. At room temperature and in the absence of a catalyst, the *condensation*, the formation of a Si–O–Si bound, of silanes on the surfaces should not occur. Only if the temperature is raised, the silanes begin to condense with the surface to form stable Si–O–Si bounds. Obviously, if di- or tri-alkoxysilanes are employed, polycondensation and multilayer formation can occur here through crosslinking between the silanes, if sufficient silane is available.

In the absence of water, elevated temperatures are used ($\geq$100 °C) to promote direct condensation of the Si–OR bound with surface hydroxyl groups. In case of diluted vapour deposition, it is assumed that the direct condensation governs the formation of the silane layer and multilayer formation is, accordingly, minimized. However, in case of aminosilanes, the situation is significantly more complicated: since the amino group acts as a base catalyst, the hydrolysis of the Si–OR bounds occurs already in the presence of trace amounts of water. It also catalyses the condensation of the alkoxy bound with the surface, but most importantly, the amino group tends to coordinate to the surface hydroxyl groups from the glass surface which can result in a head-to-tail orientation of the silanes and disordered layer formation. Preferential adsorption of amino-silanes has been described, yet their catalytic properties were also found to facilitate silane layer formation if they are added to non-amino-silanes.[77,150]

Noteworthy is that the surface condensation requires a Si–OH group which is why silane layer formation is always preceded by surface activation. Here, the condensed Si–O–Si network on the surface is hydrolysed, usually under acidic-oxidative conditions, to form as much Si–OH groups as possible.[151]

2.2.3 Mixed silane layers

The goal of understanding the silane layer formation is to apply it for the dynamic control of the functional group density on the sample surface. This can also be achieved using other methods and substrates: polypropylene (PP) can be subjected to plasma for different time intervals, but unfortunately, PP is unfavourable for this work as pointed out above. The same accounts for SAMs on gold, although these offer the best control over the formation using a binary mixture of ligands. The formation of dendrimers of different generations grafted from a functionalized surface was shown to allow a certain control of the functional group density.[31,79] However, this process only allows for a limited number of steps, each *multiplying* the density of surface functional group. Since the previously prepared samples already exceeded the linear range of the fluorescence intensity based determination, the opposite, a *reduction*, of the surface functional group density is required. Additionally, dendrimer formation results in a 3D structure of the surface which poses problems in analysing the results from XPS since attenuation effects and irregular irradiation have to be accounted for.[49]

A more promising solution is to "dilute" the surface functional group by addition of a compatible silane with a chemically inert headgroup. Compatibility here means that the two silanes co-deposit successfully and form binary surfaces with well distributed functional groups of varying density by changing the ratio of the silanes.

The application of two different silanes is often performed in a sequential manner, where one silane is deposited and a second is added afterwards to fill gaps in the silane layer, for example to increase the stability of an aminosilane layer.[76,152,153] This approach offers very limited control over the functional group density and is therefore unsuitable for this work.

The *simultaneous* deposition of two different silanes in varying ratios is significantly more suitable and was shown to be successful on different materials.[154,155] Synergistic effects upon addition of aminosilanes were found by numerous authors and are based on the preferential adsorption of the amino group and its catalytic properties.[77,156,157] Noteworthy, the effect of amino functionalities has been priorly described and does not require an amino *silane*, pure amines show a similar effect.[150,158]

Lee *et al.* used mixtures of alkyl- and aminosilane to form mixed silane layer on aluminium foils and found a trend, albeit not linear, between the amino groups on the surface and the amino silane content of the solution.[159] Despite showing the feasibility of mixed solution deposition, the different characteristics of the substrate compared to glass permit a clear transfer of the results. Wayment *et al.* used mixtures (2-cyanoethyl)triethoxysilane (CETES) with trace amounts (in the nM range) of APTES to produce surfaces with well isolated amino groups (10^{-7} fraction of a monolayer) and found a linear correlation between the number of dyes immobilized per μm^2 and the APTES amount.[73] Unfortunately, the extreme ratios of silanes they used

and the resulting surface functional group density in the region of 0.1 functional groups per μm^2 is about three orders of magnitude below the requirement for this work. Yet, with CETES, they identified a suitable candidate to dilute the investigated amino group, as it is comparable in important properties like density, boiling point and polarity to APTES and mixes well, at least with these trace amounts of APTES.

In this work, the ratios will be applied closer to the equimolar range aiming towards dilutions of surface functional groups down to ~10 % of a full layer. This approach can best be performed with the vapour deposition (VD), as it allows the parallel preparation from various silane compositions in different vessels under the same conditions. Solution based silanization would not only suffer from the high amounts of silane required (usually several mL of silane compared to µL amounts applied in the VD), but also from the equipment necessary to run a number of silanizations in parallel under solvent reflux or the time required for sequential preparation. Yet, to the best of my knowledge, simultaneous vapour deposition of binary silane mixtures was not shown yet.

2.2.4 First mixed silane deposition

Table 2.4: Fluorescence intensities of the slides prepared from different silane ratios (λ_{Ex} = 488 nm, λ_{Em} = 550 to 600 nm)

	APTES:CETES ratio		
	3:1 (**AG**)	1:1 (**AH**)	1:3 (**AI**)
F / a.u.:	14 000(2000)	22 000(3000)	30 000(4000)

Since chemical vapour deposition was not yet applied to the formation of mixed silane layers, an initial experiment was performed on the general feasibility of simultaneous deposition of two silanes. Since amino functionalized silanes are known to preferentially absorb on glass surfaces,[42,154], it might react exclusively with the glass surface, despite a different silane being present. APTES and CETES solutions (10 % in Tol) were mixed in the ratios 3:1 (Sample **AG**), 1:1 (Sample **AH**) and 1:3 (Sample **AI**). The resulting solutions were applied to the vapour deposition using 50 µL of mixed silane solution (This amount was shown earlier (Sec. 2.1.4) to be sufficient for complete silane layer preparation). After careful cleaning, the slides **AG**-**AI** were reacted with **1** and, after cleaning, analysed in the microarray scanner.

The fluorescence intensities measured on the mixed silane samples shown in Table 2.4 clearly show an intensity change with changing silane ratio. Unfortunately, the trend is opposite of the expectation, e.g. the intensity increases when the content of amino groups (supposedly) decreases.

These results are in agreement with prior experiments based on changing the volume of the amino silane solution (Sec. 2.1.4, Samples **AE** and **AF**). It is likely that the mixing of silanes in principal works as planned, yet the dynamic range of the fluorescence method is still exceeded. Additionally, the high uncertainty of the fluorescence measurements (>10 %) indicates a significant inhomogeneity of the prepared surfaces and points towards potential for optimization of the performed VD method.

2.3 Process control through contact angle (CA) measurements

The previous results point to a lack of control and understanding of the applied VD process. The employed methods of characterization, namely fluorescence scanning and XPS, both depend on the surface functional group label which itself is the initial subject of investigation. Accordingly, the ability to judge the quality of the surfaces in terms of homogeneity and reproducibility requires a different method for direct analysis of the prepared surfaces. A well-known technique to characterize the morphological and chemical properties of a surface is the static contact angle measurement.[160] Here, a liquid droplet is deposited on the surface and the angle (θ_C) at the air/liquid/solid interface is measured. The contact angle is determined by the chemical , as well as the morphological composition of the surface, the majority of the application invokes water as liquid for analysis.[161] In the context of this work, the technique will be mainly employed to understand the chemistry of the surfaces since morphological aspects should be of minor importance. For silane treated surfaces, contact angle measurements are well established not only as quality control but also to determine the surface free energy.[162] In contrast to fluorescence scanning and XPS, the obtained information is strictly qualitative. Yet the important parameters of homogeneity and reproducibility can be directly derived from the standard deviation of θ_C across a slide and the value of the θ_C across different samples. Given the ease of operation and lack of sample pre-treatment, the CA measurement is an especially valuable tool for constant quality control in the stepwise optimization of the surface preparation process. It has to be noted, that the static contact angle is not necessarily sufficient to describe the quality of the surface. Apart from the application of different solvents to achieve a characterization of the surface free energy,[162] the measurement of dynamic contact angles holds a significant potential. Here, not the contact, θ_{adv} is mainly governed by the more hydrophobic contributions on a surface, where angle of the sessile drop is measured, but of a dynamic system, the contact angle formed at the advancing solvent front is called advancing contact angle , the one at the receding is called receding contact angle , accordingly. The contact angle hysteresis (θ_{hys}) is the difference of these two values ($\theta_{hys} = \theta_{adv} - \theta_{rec}$) and is, on smooth surfaces, commonly treated as a measure of the surface chemical surface heterogen-

eity.[163] In a simplified picture of thermodynamic hysteresis of water droplets, θ_{adv} is mainly governed by the more hydrophobic contributions on a surface, whereas θ_{rec} is governed by the hydrophilic contributions of the surface.[164] Accordingly, comparing different surfaces on the same substrate, a low hysteresis is the sign of chemical more homogeneous surface. It should be noted, that an important effect leading to contact angle hysteresis on a surface is swelling upon water contact.[163,164] This especially relevant for the receding contact angle which is accordingly difficult to be determined reliable.[165] On the investigated surfaces , silanes on glass, surface swelling is expected to be a significance on the measurement of dynamic contact angles. It is noteworthy that the glass surface is not ideal for dynamic contact angles as it not as smooth as the typically employed silicon wafer surfaces and a certain hysteresis will be due to substrate roughness.

The contact angle technique was introduced to the group in the course of this work. Accordingly, this technique is used as a rather simple tool for the characterization of surface heterogeneity and composition and the full potential of the technique could not exploited.[160,164] The first investigations were based on the static contact angle (θ_C).

2.3.1 Orientation on commercial samples

Commercial organic surfaces on glass slides were investigated to serve as a reference for the range of contact angles to be expected on organically modified surfaces for bio-analytical applications.

The reference surfaces were PolyLysin™ and SuperFrost® adhesion slides from Menzel and aminosilane-functionalized microarray substrate (Slide A+) from SCHOTT Nexterion®. The latter is prepared by APTES condensation from dry toluene under reflux and should therefore be comparable to the samples investigated in this work. The PolyLysin™ slide is covered with poly-lysin as an adhesive. SuperFrost®+ is also an adhesion slide, for electrostatical adhesion, but the surface components are not disclosed by the manufacturer. The resulting static water contact angles (θ_C) are summarized in Table 2.5. The contact angles on the Menzel adhesion substrates are lower than on the microarray substrate from SCHOTT Nexterion®, as

Table 2.5: Static water contact angles (θ_C) (from ten or more drops) as measured on commercial microscope slide substrates

Sample	θ_C / °
PolyLysin™	59(1)
SuperFrost®	52(4)
Nexterion® A+	77(1)

they are optimized for electrostatic adhesion, whereas the latter should provide reproducible spot formation. Accordingly, the contact angle determination is with ±1° very reproducible. Only the SuperFrost® substrate shows an elevated error of ±4°. The difference in contact angle between the aminosilane and the poly-lysin surface could originate in the higher density of amino groups and the higher charge density of the latter substrate.

2.3.2 Investigation of activation

Table 2.6: Applied activation procedures and respective water contact angles

	Procedure	Sample	θ_C / °
1.	NH_4OH(30 %):H_2O_2(30 %):H_2O 1:1:5	**AJ**	4(1)
2.	HCl(37 %):H_2O_2(30 %):H_2O 1:1:5	**AK**	3.8(4)
3.	H_2SO_4(conc.):H_2O_2(30 %) 3:1 (Piranha)	**AL**	23(3)
4.	1 M KOH	**AM**	14(3)

The investigated activation solutions are listed in Table 2.6. The first two (Slides **AJ** and **AK**) are to compare acidic and basic oxidative pretreatment in diluted solution, the Piranha solution (**AL**) is the current reference procedure. The KOH treatment was used, as strongly basic solutions are known to open the Si–O bond and expected to yield a high density of silanol groups as well. All slides were thoroughly rinsed, pre-treated in HCl/MeOH 1:1 for 1 h, and activated at 80 °C in the respective solution for 2 h, after which they were repeatedly rinsed and dried in the centrifuge.

A good activation is considered to be characterized by a low contact angle, as the hydrogen bridged, strongly polar silanol surface should be much more hydrophilic than the silicon oxide surface. As it is shown in Table 2.6, only the treatment involving diluted H_2O_2 results in contact angles <5°, which characterizes highly hydrophilic surfaces. It should be noted that contact angles below five degree are in general very difficult to measure. In the current example, the activation on **AK** resulted in comparably regular drops, whereas in the case involving NH_4OH the drops were less regular as shown by the higher error of the measurement. Not only because of the better activation, but also due to the slightly less convenient handling of the NH_4OH solution, the HCl/H_2O_2 treatment is preferable.

The commonly used Piranha solution fails to properly increase the hydrophilicity of the glass surface. This can be explained by the hygroscopic nature of the oleum. The underlying reaction equilibrium yielding the formation of peroxymonosulfuric acid ($H_2SO_4 + H_2O_2 \rightleftharpoons H_2SO_5 + H_2O$) permits the presence of higher amounts of water for the Piranha solution to be efficient. Yet the transfer of silicon oxide on the glass surface to hydroxyl groups requires the presence of water: $Si{-}O{-}Si + H_2O \rightleftharpoons 2Si{-}OH$. Accordingly, despite being probably among the most efficient *cleaning* methods, especially for dissolving even the most resilient organic overlayer, Piranha water seems not to be the method of choice to achieve maximum *activation* of the silicon oxide surface.

The activation involving potassium hydroxide is also not as efficient as the aqueous-oxidative methods. Additionally, the samples retained an opaque appearance after the treatment, which indicates either the formation of a solid, unremovable residue or significant destruction of the surface.

The samples were amino-functionalized using the VD method with APTES following the previous procedure, but the resulting surfaces showed no pronounced differences from each other with $\theta_C \approx 55(6)^\circ$. Given the high error of the contact angle, compared for example with the commercial amino silane sample (see Sec. 2.3.1), it is likely that the differences between the activation procedures are of little influence on the resulting surfaces since the unoptimized VD process introduces a significantly higher heterogeneity that masks the subtle differences resulting from the different activation procedures. The sample size was insufficient to substantiate this assumption with more complex statistical analysis (analysis of variance) and the quality of the samples to poor to justify more effort on that matter.

2.3.3 Influence of deposition time

Table 2.7: Static water contact angles θ_C after different reaction times for the vapour deposition and consecutive cleaning, results and errors calculated from two individual samples

Run	θ_C / ° after VD for:		
	2 h (**AN**)	4 h (**AO**)	24 h (**AP**)
1	50(12)	60(10)	60(10)
2	51(6)	54(6)	57(5)

A number of cleaning and activation procedures are used throughout the literature. The majority are solution based methods, mostly involving H_2O_2, in combination with HCl[166] or NH_4OH[167] in diluted solution or with concentrated H_2SO_4 (Piranha solution).[61,66,76,95,135,144,168–175] Combinations of different solutions[80,162,167,176] or solution cleaning, mostly with Piranha solution, and Plasma[34,48,81,91,152,177,178] or UV/ozone[73,143,179] treatment are also found, some pub-

lications used different methods, yet missed to comprehensively compare the resulting surfaces.[69,103] Very rarely a difference is made between *cleaning* the surface, e.g. removing metallic and/or organic contaminants, and *activating* the silicon oxide surface, e.g. creating a high number of silanol groups (Si–OH). From the literature known methods, Piranha solution is most commonly applied to clean/activate silicon oxide based surfaces. However, due to its hygroscopic nature, the effectiveness in terms of *activation* is questionable. To understand the influence of the pre-treatment, different procedures, all solution-based, were investigated.

To validate the time required to achieve a homogeneous silane layer of acceptable thickness, the reaction during the vapour deposition was changed from two (**AN**) to four (**AO**) and finally 24 hours (**AP**). The slides were washed after deposition consecutively by ultrasonication in acetone and isopropyl alcohol (IPA) and finally stirred in MeCN over night and dried by centrifugation prior to the static water contact angle measurement. This procedure was repeated to evaluate the robustness of this determination (second run in Table 2.7).

The results in Table 2.7 show no significant differences between the different reaction times, only a slight increase of θ_C upon increasing the time to 4 h, which could be an indication that the layer formation is incomplete after 2 h. Prolonging the reaction time to 24 h does not result in a notable change in contact angle, however, the surfaces of the slides reacted for this time were of opaque appearance, in contrast to the transparent surfaces of the other samples, which could be explained with the formation of a significantly thicker silane layer. Much more notable is the reduced error after the second washing which points to an insufficiency in the cleaning, despite being more rigorous than commonly applied washing procedures. As neither the activation procedure, nor the reaction time for the VD show a significant effect on the resulting contact angle, mostly due to the significant error involved, further work on the influence of the final cleaning after the VD is necessary.

Another influential factor, the rigorous control of the humidity involved in the VD, will be the course of later work.

2.3.4 Cleaning of slides after VD and optimization of VD vessel

The practical handling of the vapour deposition suffers from the fact that the slides are loosely placed in the bottle and the silane solution on the bottom of the vessel. This might lead to premature contact of the silane solution with the slides and sometimes to the slides attaching to one another, in which case the process is not strictly deposition from vapour anymore. To overcome this problem, a special Teflon plate was designed to be placed in the centre of bottle (see Fig. 2.11). It serves as a stable separation between the slides and prevents then from attaching face-to-face. A small indentation in the plate serves as a vessel for the silane solution and the bevelled edges facilitate handling. Three sets of slides, containing two slides each,

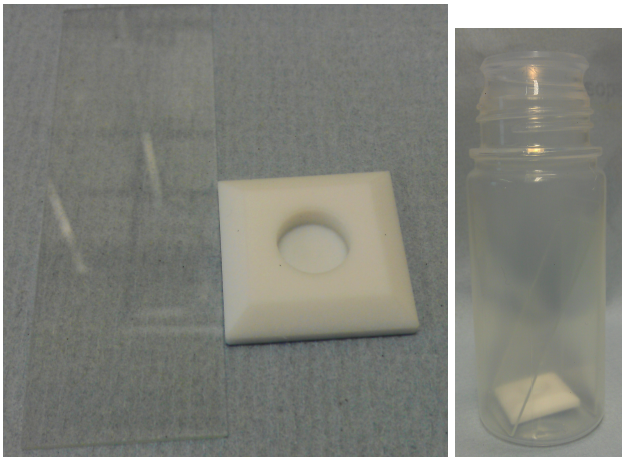

Figure 2.11: Detailed view of the Teflon® plate with a microscope slide for size comparison (left) and a VD bottle containing two slides and the plate

were prepared under similar conditions with fresh APTES following the previous procedure, only including the new Teflon plates. After the vapour deposition and careful rinsing, one set was cleaned under consecutive ultrasonication with acetone, IPA, MeCN and finally water for 10 min each (**AQ**). The second set was placed in MeCN over night (**AR**) and the third set kept *in vacuo* (~0.1 mbar) over night at 70° (**AS**).

All samples were rinsed and dried in the centrifuge prior to the first contact angle measurement. As it is shown in Table 2.8, the contact angles differ significantly between the different cleaning procedures. The ultrasonic cleaning leaves the slide with a substantial error and limited reproducibility, resulting in a difference of $\Delta\theta_C = 14°$ between the two slides measured for **AQ**. These samples were rejected for further analysis by fluorescence labelling for that reason. Sample **AR** shows the lowest contact angle and the highest homogeneity, so it was assumed that this treatment resembles the most efficient cleaning. The samples cured *in vacuo* showed significantly higher contact angles, but also comparable homogeneity. It should be noted that

Table 2.8: Static water contact angles of slides treated with APTES vapour after different cleaning procedures, directly after cleaning and centrifuging and after additional drying in vacuum

Sample	θ_C / °	
	centrifuged	Vacuum dried
US (**AQ**)	63(15)	75(2)
MeCN (**AR**)	55(3)	71(3)
in vacuo (**AS**)	63(4)	72(3)

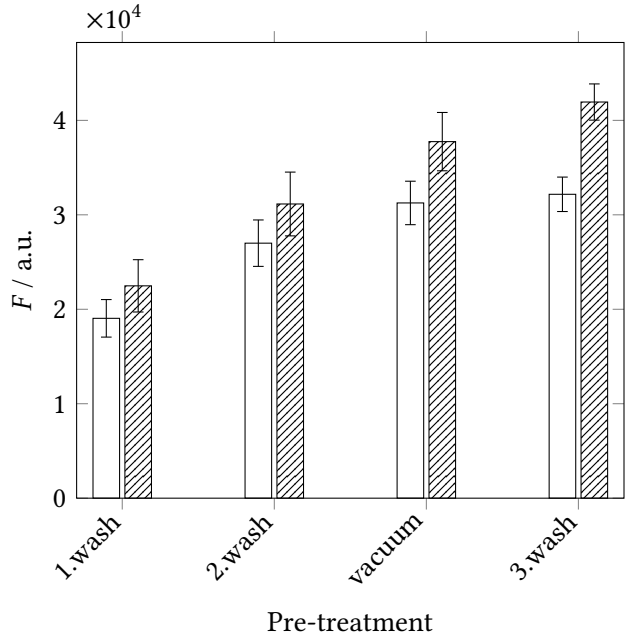

Figure 2.12: Fluorescence intensities of samples **AR1** (cleaned in MeCN after VD, ▯▯) and **AS1** (cured *in vacuo* after VD, ▨▨) after consecutive cleaning steps (λ_{Ex} = 488 nm; λ_{Em} = 550 to 600 nm)

the adopted procedure involving the Teflon plates for the VD yielded a general increase in precision of the CA measurements. Only later it was realized that the difference is not only due to the silane layer, but that the different treatment left the surfaces in different contents of solvent/moisture. To access that effect, the samples **AQ**, **AR** and **AS** were re-evaluated with contact angle measurement after all being additionally dried *in vacuo* (~0.1 mbar, 40 °C, 3 h). As shown in Table 2.8, the vacuum treatment has a tremendous effect on the measured contact angle. The differences that were priorly noticed vanished into insignificance, both for the absolute values as well as the errors of the measurement. These findings can be explained by the different swelling times/conditions employed: the ultrasonic treatment involved exposure to different solvents under comparatively harsh conditions, leaving the layer swelled with a mixture of solvents, resulting in significant variations in the wettability. **AR** on the other hand was neatly saturated with MeCN, as indicated by the low, precisely defined θ_C. The vacuum treated samples were thoroughly dried and could only slightly swell during the water rinsing step, hence the higher θ_C.

To avoid future errors resulting from different wetting states, all future samples will be dried *in vacuo* prior to the CA measurement.

AR1 and **AS1** resulted from additional treatment with **1**. The samples were cleaned repeatedly by stirring in MeCN over night, and cured *in vacuo* after the second washing step. As shown in Figure 2.12, the first cleaning is insufficient to reach a stable fluorescence intensity. Only after two cleaning runs and curing *in vacuo*, the fluorescence intensity stops changing significantly, e.g. a stable signal is reached. Noteworthy is that sample **AS1** shows an increase of 87 %, whereas in the case of **AR1**, the enhancement amounts to only 69 % of the fluorescence intensity measured after the first washing step. These differences should result from the less efficient cleaning of **AS1** after the vapour deposition.

2.3.5 Vapour deposition of different silanes

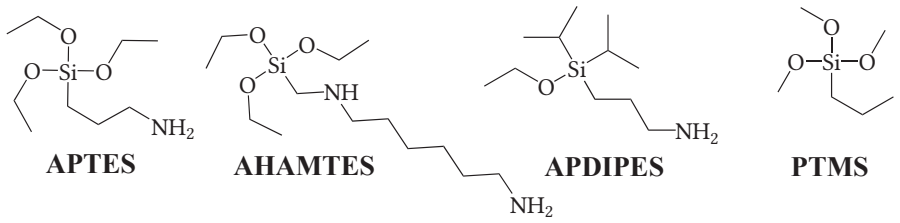

Scheme 2.3: Structures of silanes applied to VD for comparison

Despite being the by far most popular silane for aminated glass surfaces, APTES provides a rather complicated chemistry that renders it less than ideal for reliable surface preparation.[91,93,135,144] Having optimized the vapour deposition procedure and the contact angle determination, the potential of different silanes can now be conclusively investigated. According to the literature, two silanes to replace APTES are *N*-(6-aminohexyl)aminomethyltriethoxysilane (AHAMTES) and (3-aminopropyl)diisopropylethoxysilane (APDIPES). Due to its length and the position of the amines in the chain, the amino functionalities of AHAMTES were shown to be less efficient in coordinating to a surface silanol group which results in more regular structure of the silane layer.[135,144]. APDIPES, which only contains a single surface-binding site (alkoxy residue) is inherently hindered at multi-layer formation and forms smooth monolayer instead.[65,89–91] Additionally, the bulky *i*-Pr side chains prevent the amino group from coordination to the surface and protect the Si–O–Si silane bound which makes the APDIPES derived surface less prone to hydrolysis compared to APTES and (3-aminopropyl)dimethylethoxysilane (APDMES).[91] The unfunctionalized silane n-propyltrimethoxysilane (PTMS) was chosen as an amino-free reference (for structures see Scheme 2.3). Two slides per silane were applied to the VD for each silane and washed with repeated replacement of the solvent for 48 h in acetonitrile.

Additional to the static contact angle (θ_C), the dynamic contact angles (θ_{adv}, θ_{rec} and θ_{hys}) where included in the analysis as well. The contact angles listed in Table 2.9 of the differently silanized samples show remarkable variations, indicating that the silane film in its chemical composition is of major influence on the contact angle. **AT** shows a medium contact angle but with a significant error, as it was already seen in earlier experiments, only **AU** shows a higher heterogeneity in the static contact angle. Noteworthy, also the advancing contact angle (θ_{adv}) of **AU** shows a significant error. As θ_{adv} is measured on two different areas with two consecutive measurements per drop, a high error in this value usually indicates a marked difference between the two areas, e.g. a macroscopic heterogeneity in the silane film. One of the difficulties in using a long-chain silane like AHAMTES is the possibility of forming stable head-to-tail orientation packing of the silane, with the amino group pointing to the surface.[66,180] Yet, the APTES derived surface shows the highest contact angle hysteresis and PTMS the lowest, with AHAMTES and APDIPES in between. This can be attributed to the chemical heterogeneity of the APTES film originated in the rather chaotic packaging that results from the various interactions of APTES with a siloxane surface.[180] In this case, a multitude of functionalities are exposed to the water drop, some less polar, like the *n*-Pr chain or the ethoxy residues of non-hydrolysed alkoxy residues, some very polar, like the protonated amino groups or SiO_x clusters. **AV** shows most stable contact angles and with medium hysteresis, indicating a homogeneity and more ordered exposure on the surface, mostly comprising the less polar compartments of the silane. **AW** finally shows subtle differences in the errors of the dynamic contact angles, which can be interpreted as a slightly higher overall variation in silane density. However, the surface accessible to the water drop is chemically comparably homogeneous, as verified by the very low hysteresis.

The samples prepared from different silanes were additionally reacted with **1**. They were afterwards washed repeatedly in MeCN. The slide **AU1** was lost after the fifth cleaning step due to an accident in handling and could not be measured again. As **AW1** showed a surprisingly high fluorescence intensity, it was additionally cleaned in a Soxhlet extractor over night in MeCN reflux. Figure 2.13 summarizes the measured fluorescence intensities. **AV1** showed a

Table 2.9: Static and dynamic contact angles of samples reacted with different silanes under similar conditions

Silane	Sample	θ_C / °	θ_{adv} / °	θ_{rec} / °	θ_{hys} / °
APTES	**AT**	66(4)	73(1)	36(1)	37
AHAMTES	**AU**	55(6)	54(5)	28(1)	26
APDIPES	**AV**	75(2)	83(1)	58(1)	25
PTMS	**AW**	80(2)	85(2)	71(3)	14

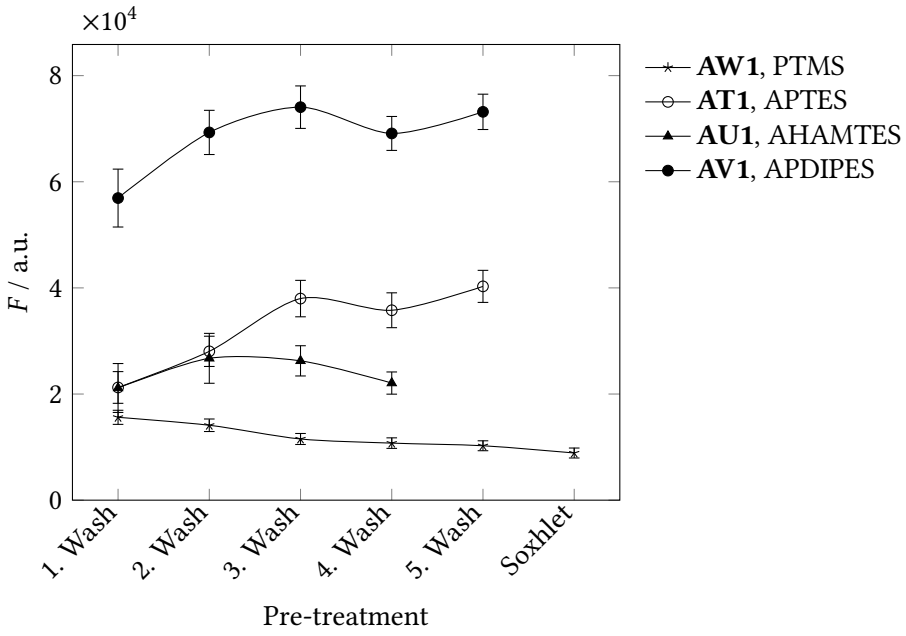

Figure 2.13: Fluorescence intensities of samples derived from different silanes, labelled with **1**, after consecutive cleaning steps (λ_{Ex} = 488 nm; λ_{Em} = 550 to 600 nm)

tremendously higher fluorescence intensity and was measured with a different PMT voltage of V = 450 V compared to the 500 V used for the other samples. By comparing different samples measured at both voltages, it was found that the attenuation factor from 500 V to 450 V amounts to exactly 2.0(1), the given fluorescence intensities for **AV1** are the originally measured values multiplied with this attenuation factor.

As shown in Figure 2.13, a considerable background fluorescence is measured on **AW1**, although this sample does not contain amino groups. However, this is the only sample where washing leads to a continuous reduction of the fluorescence intensity, indicating a strong non-covalent binding of the dye. The origin of this effect will be the course of following experiments.

For the two short-chain amino silanes (Samples **AT1** and **AV1**), a stable fluorescence signal is reached after the third cleaning step with **AV1** showing nearly twice the intensity of **AT1**. As **AV1** was prepared using the mono-alkoxy silane, inherently hindered at multi-layer formation, it is unlikely that this higher fluorescence signal originates from a higher amino group density.[91] The more reasonable explanation is that the lower density leads to less fluorescence quenching.

AU1 does not change significantly with the different washing steps, the fluorescence intensity shows a slight increase and then drops after the third cleaning step. The error of the measurement also reduces until after the third washing step for all three amino silanes and drops nearly to half the initial value in all cases, although the error varies significantly with the silane: AHAMTES (**AU1**) shows a change from 21 to 9 %, APTES (**AT1**) reduces from 14 to 8 % and APDIPES (**AV1**) from 10 to 5 %. Especially the high error of θ_C in sample **AU1** is in agreement with the heterogeneity seen in the fluorescence measurements. From these results it can be concluded that APDIPES is superior for the preparation of reference surfaces to investigate the dynamic behaviour of the fluorescence intensity upon functional group labelling. Not only does it show the highest fluorescence intensity, but also the highest homogeneity, as proven by CA measurements as well as fluorescence scanning. AHAMTES failed to deliver unequivocal results. Given its significantly higher boiling point (~410 °C compared to 217 °C for APTES) it is possible that the current VD procedure is less efficient for AHAMTES. However, as the surface prepared using the inert silane PTMS retains a significant amount of dye, the VD process does not seem to be sufficiently optimized, since simple electrostatic attraction between the glass surface and the dye was ruled out by control experiments on untreated slides (see Sec. 2.1.4).

2.4 Optimized vapour deposition for composite silane surfaces

2.4.1 Composite APDIPES:CETES surfaces

One major source of uncertainty in the current VD procedure is the insufficient control of moisture during the procedure. Although the bottles are prepared under an Ar stream, limited exposure to air can not be excluded. Only preparing the vessels under an argon atmosphere could serve to minimize residual moisture in the vessels during the VD. This would usually be achieved by preparing the samples in a glove box which is not available. A viable alternative is a portable glove bag, in which the vessels are placed and an protective atmosphere is produced by repeated evacuation/flooding with Ar cycles. The drying procedure after the activation was replaced by drying the samples *in vacuo* (<0.1 mbar) over night in a desiccator connected to an Ar source to retrieve the samples under an inert gas stream. The toluene is stored at least three days over activated molecular sieves in oven dried glassware and, like the silanes, only handled under Ar atmosphere. All materials to handle the liquids where dried *in vacuo* prior to being transferred into the glove bag. The bottles for the VD are sealed tightly before being

removed from the Ar atmosphere and placed in the oven. After VD, the bottles were immediately transferred into the desiccator, opened under an Ar stream and subjected to vacuum to remove unreacted silane vapour. Upon cooling *in vacuo*, the slides are rinsed carefully, dried in the centrifuge and cleaned in a Soxhlet extractor with acetone over night. Acetone was chosen, as it boils at an acceptable temperature and without azeotropic water.

A new set of mixed silane slides was prepared following this optimized procedure, where, based on the previous experiments, APTES is replaced by APDIPES. CETES was kept as inert silane, despite probably not being the compound of choice to combine with the mono-alkoxy silane APDIPES. The following APDIPES:CETES ratios were used: 1:0 (**AX**), 3:1 (**AY**), 1:1 (**AZ**), 1:3 (**BA**) and 0:1 (**BB**).

2.4.1.1 CA measurements

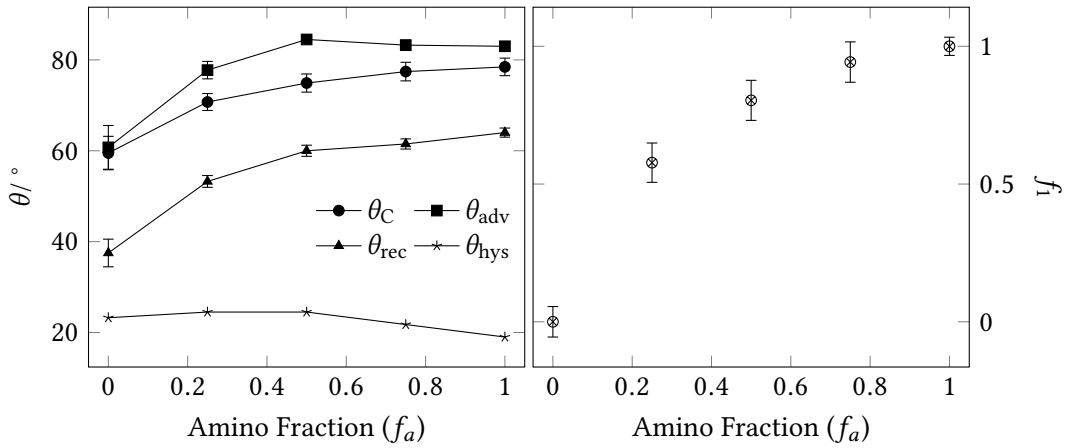

Figure 2.14: Static (θ_C) and dynamic (θ_{adv}, θ_{rec} and θ_{hys}) contact angles of mixed APDIPES/CETES samples **AX**-**BB** vs the fraction of APDIPES applied to the VD (f_a) (left) and the calculated amino fraction from Cassie's Law (f_1 vs f_a)

Table 2.10: Data overview for samples **AX**-**BB**, including the amino silane fraction applied to the VD (f_a), the normalized fluorescence intensity from **AX1**-**BB1** (f_f) and the amino ratio derived from Cassie's Law (f_1)

Sample	f_a	θ_C / °	θ_{adv} / °	θ_{rec} / °	θ_{hys} / °	f_f	f_1
AX	1	78(2)	83(1)	64(1)	19	1.0(1)	1.00(3)
AY	0.75	77(2)	83(1)	62(1)	22	0.79(5)	0.94(7)
AZ	0.5	75(2)	85(1)	60(1)	25	0.74(5)	0.80(7)
BA	0.25	71(2)	78(2)	53(1)	25	0.53(8)	0.58(7)
BB	0	60(4)	61(5)	38(3)	23	0.006(1)	0.00(6)

The samples were first characterized by static and dynamic contact angles. As it can be seen in Figure 2.14 and Table 2.10, the static contact angle changes with the fraction of amino silane in the silane mixture applied to the VD (f_a), and the values of the mixed surfaces span between the individual single silane surfaces. The advancing contact angle shows very little change for samples **AX**-**AZ**, only upon decreasing f_a to 0.75, the advancing angle drops. In contrast, the receding angle reduces continuously and drops strongly going from **BA** to **BB**. In the case of chemically heterogeneous samples, θ_{adv} is mainly affected by the hydrophobic contributions, which here stem from the *i*-Pr side-chains of the APDIPES whereas θ_{rec} is governed by the hydrophilic interactions which mainly involve the silicon oxide bounds of the substrate. These predominate the contribution of CETES. Accordingly, an increase of CETES on the surface affects θ_{rec} more strongly, leading to an increased θ_{hys}. To estimate the ratio of the two silanes, Cassie's Law (Eq. 2.3) was employed which states that for composite binary surfaces, the apparent contact angle of the mixed surface (θ_c) depends on the fraction of the components (f_1 and f_2) and their pure contact angles (θ_1 and θ_2).[181,182]

$$\cos\theta_c = f_1 \cos\theta_1 + f_2 \cos\theta_2 \tag{2.3}$$

Those fractions directly relate to the chemical ratios, assuming that other parameters affecting the contact angle, like surface morphology or density, of surface modification are comparable for both silanes. Accordingly, since $f_1 + f_2 = 1$ and θ_c, θ_1 and θ_2 are known, the fraction of amino silane on the surface (f_1) can be calculated (Table 2.10). Figure 2.14 plots f_1 versus the applied amino fraction f_a. The amino component seems to dominate the deposition, as it was suggested in earlier work.[150,156] A detailed discussion of the kinetics can not be obtained at this point, but can be found later in this work (2.5.2) and in reference 65.

2.4.1.2 Fluorescence Analysis

The labelling with **1** on the previously prepared APDIPES derived surface (sample **AV1**) suggested that the lower amino group density compared to APTES surfaces (e.g. sample **AT1**) leads to a fluorescence unaffected by fluorescence quenching. The new mixed silanes samples were labelled with **1** (Samples **AX1**, **AY1**, **AZ1**, **BA1** and **BB1**), mainly following the previous procedure, only substituting the cleaning with Soxhlet extraction with acetone for 24 h. Figure 2.15 shows the fluorescence intensity change versus the applied amino fraction f_a. Most noteworthy is the very low background fluorescence on the inert silane surface which clearly shows that **1** is a reliable functional group label with little background signal, if a certain surface quality is met. In contrast to previous experiments on APTES based systems, the fluorescence intensity now shows an increase with increased amino groups fraction. However, in agreement with

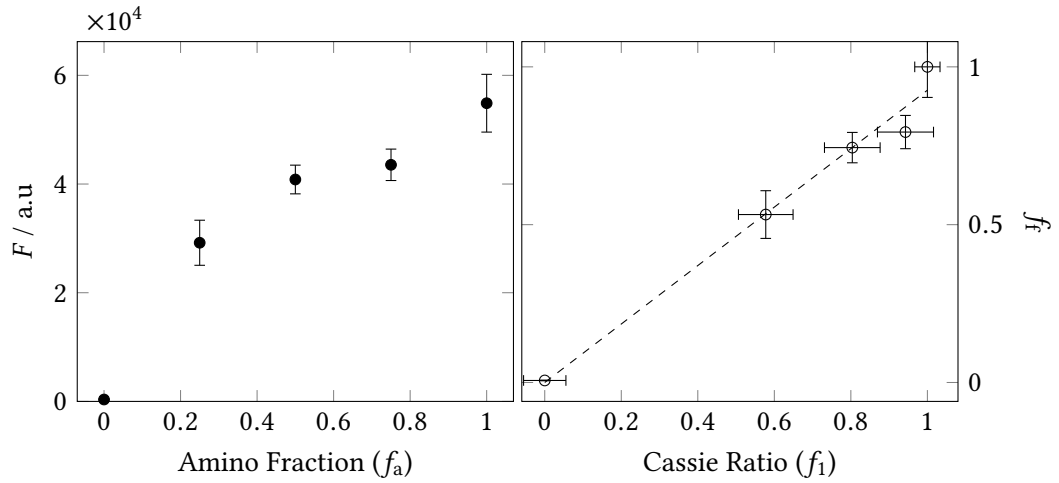

Figure 2.15: Fluorescence intensities vs the applied APDIPES fraction (f_a) for samples **AX1-BB1** (left, λ_{Ex} = 488 nm; λ_{Em} = 550 to 600 nm) and normalized fluorescence intensity (f_f) vs the amino fraction determined by Cassie's Law (f_1), including linear regression (- - -, $y = 0.926x$, $R^2 = 0.98$)

the results obtained from the contact angle measurements, the increase is not strictly linear. To evaluate the correlation between the fluorescence intensity and the calculated amino fraction f_1, the fluorescence intensity was normalized with respect to the highest value. Assuming that the labelling yield is the same for all samples and no fluorescence quenching occurs, the normalized fluorescence intensity equals the amino group fraction. Accordingly, the normalized fluorescence intensity will be treated as amino group fraction determined by fluorescence labelling (f_f). Comparing f_f with f_1 (see Fig. 2.15) yields an approximately linear correlation, to finally show that quantitative information can be obtained from labelling with **1**. However, this information is only relative and does not allow to derive absolute amounts of functional groups. As it is also represented by the elevated errors, f_1 does not seem most reliable. A probable reason is that the requirements for Cassie's Law to be applicable are not fully met. Especially the density and structure of the silanes is expected to change notably when comparing a mono-alkoxy with a tri-alkoxy silane.[91] This also means that the composite surfaces are not a simple linear combination of the respective individual surfaces, as Cassie's Law assumes. Further work shall therefore focus on the application of more comparable silanes.

2.4.1.3 XPS analysis

A selection of samples was investigated with XPS to estimate if the dual-mode labelling still holds potential when the amount of functional groups appears to be substantially reduced. Table 2.11 comprehensively lists the measured elemental fractions on **AX1**, **BA1** and **BB1**; Na 1s, Ca 2p and Mg 2s were also found, as they are typically contained in such glasses, but were excluded from the analysis as they do not bear additional information. It can be seen that the carbon content *decreases* going from APDIPES to CETES, whereas the nitrogen content *increases* significantly. Such behaviour is expected since the C/N ratio changes from 9 to 3, assuming that all three alkoxy groups of CETES reacted with the surface, and taking into account that label **1**, which mainly contributes carbon, is basically absent on **BB1**. The latter is well represented by the presence of fluorine of on **AX1**, although in lower amounts than previously encountered (see Sec. 2.1.4), whereas the amount seen on **BB1** is well below the common limit of detection for fluorine of 0.1 at%. The presence of the dye is also indicated with the reducing layer thickness, which in turn is evidenced by the decreasing C/Si ratio, the prior being representative for the overlayer and the latter for the glass substrate.

The labelling ratio of the amino groups with **1** can be determined from the N/F ratio of **AX1** to be around 5 % (see Sec. 2.5.2 and ref. 65 for details on the calculation).

Now adding **BA1** to the comparison firstly shows that the fluorine content is roughly half of the one seen on **AX1**. This is well in agreement with the fluorescence intensity, that determined the content of **1** to 53(8) % compared to **AX1**, and the Cassie ratio of 0.58(7). However, contents of nitrogen and carbon are not in between those seen on **AX1** and **BB**, but the carbon content compares to **AX1** and the nitrogen content to **BB1**. This implies again that the composite surfaces of APDIPES and CETES can not be treated as linear combination of the two components, but are structurally different.

Table 2.11: XPS fractions of relevant elements for representative **1** labelled mixed silane samples; Na 1s, Ca 2p and Mg 2s excluded

Sample	f_a	elemental fractions / at%					relevant ratios		
		C 1s	N 1s	O 1s	Si 2p	F 1s	C/N	N/F	C/Si
AX1	1	31(1)	1.1(1)	46.3(7)	20.9(5)	0.4(1)	28.1	2.6	1.5
BA1	0.25	29(1)	1.9(1)	47.5(8)	21.6(4)	0.2(1)	15.6	10.4	1.3
BB1	0	17.8(7)	1.9(2)	55.0(5)	25.3(4)	0.03(5)	9.5	54.1	0.7

It should be noted that PFA bottles used for the vapour deposition were found in different experiments (not shown) to contaminate the samples with varying degrees of fluorine. Although there is only very little contamination in this experiments, a surrogate based on non-fluorinated, or more stable fluorinated, materials needs to be found.

2.4.1.4 Conclusion

The experiments performed on mixed APDIPES:CETES surfaces provided valuable insight in the performance of **1**. An amino group content, that, after labelling, meets the linear range of the fluorescence intensity determination can be achieved with silane chemistry, yet the exploitable overlap with XPS remains to be evaluated. For detailed analysis, especially based on the relative elemental composition, the composite surfaces of the individual components require a certain comparability that does not appear to be met. The determination of the component ratios, however, can be approached using the simple and straightforward contact angle analysis. Further work will focus on the preparation of binary composite surfaces with a high similarity to the individual surfaces to enable a clear analysis of the elemental data.

2.4.2 Composite APTES:PTMS surfaces

Since tri-alkoxy silanes are significantly more often used than mono-alkoxy silanes, an attempt on preparing a reference surface with the required properties was made based on a binary APTES:PTMS system. The latter was chosen since the contact angles of the APTES and the previously applied CETES are comparably close and therefore the "contrast" required for successful Cassie ratio determination is very low. The vapour deposition process was adapted in several parameters:

1. The cleaning was substituted with an ultra-sonic cleaning in alkaline glass cleaning solution (Hellmanex® II)
2. The activation was performed in plasma cleaner instead of the previously used wet procedure
3. The VD was performed in special oven-dried glass bottles with highly resistant TpCh260 lids

These parameters were assessed to be of little influence on the resulting surfaces and were mainly changed to facilitate the procedure and reduce the hazardous waste. The following APTES:PTMS ratios were used: 1:0 (**BC**), 1:1 (**BD**), 1:3 (**BE**), 1:7 (**BF**) and 0:1 (**BG**). The amino silane fractions are changed to lower ratios compared to **AX**-**BB** to account for the higher reactivity of the amino silanes.

2.4.2.1 Contact angle measurements

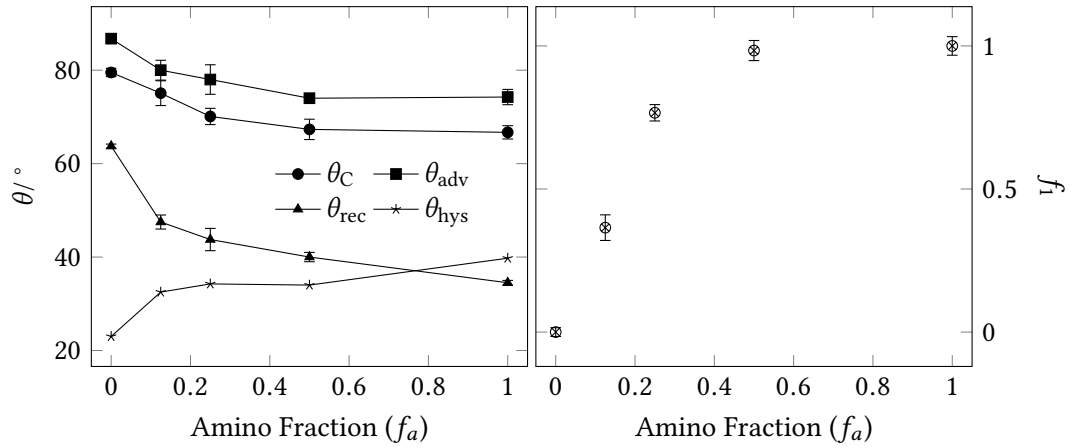

Figure 2.16: Static (θ_C) and dynamic (θ_{adv}, θ_{rec} and θ_{hys}) of mixed APTES:PTMS samples **BC**-**BG** vs the fraction of APTES applied to the VD (f_a) and the calculated amino fraction from Cassie's Law (f_1 vs f_a)

The samples were first characterized by contact angle measurements (Fig. 2.16). In contrast to the APDIPES:CETES samples, the static contact of the amino silane is lower than that of the inert silane (67(1)° vs 79.5(9)°). Accordingly, the contact angles of the mixed samples ascend with decreasing amino fraction. Although the contact angles of the individual silane surface are comparatively precise with errors of ~1°, the composite surfaces are significantly less defined (uncertainty up to 3°). The same effect is found in the dynamic contact angles. The most reasonable explanation is a domain formation of the individual silanes instead of an even distribution throughout the sample. Noteworthy is strong change in θ_{hys} going from **BC** to **BG** (40° vs 23°), with the mixed samples showing a constant hysteresis. θ_{adv} and θ_{rec} change constantly for the mixtures, accordingly. In the prior samples **AX**-**BB**, the change in advancing angles was delayed compared to the static angles, due to the fact that they were mainly influenced by the amino silane APDIPES. In the current case involving APTES, the advancing angles change rather continuously with changing ratio, whereas the receding angle shows a delayed change and increases abruptly going to the pure PTMS surface. Since the θ_{rec} for the pure APTES surface is very low with 35°, the differences should be more significant than simply adding an amino group to the *n*-Pr chain. More likely is a different structure or layer thickness, possibly presenting elevated amounts of silane network to the contact line, in the presence of

APTES. The Cassie ratio (f_1) was also determined for **BC**-**BG** (see. Fig. 2.16) and shows the expected trend, again with the preferential binding of the amino silane. Interestingly, the apparent fraction on **BD** is the same as on the pure APTES sample **BC** and indeed θ_C and θ_{adv} are identical for both samples, only θ_{rec} increases for **BD**. This is another indication of more fundamental differences between the composite and the pure silane surfaces for APTES:PTMS.

2.4.2.2 Fluorescence analysis

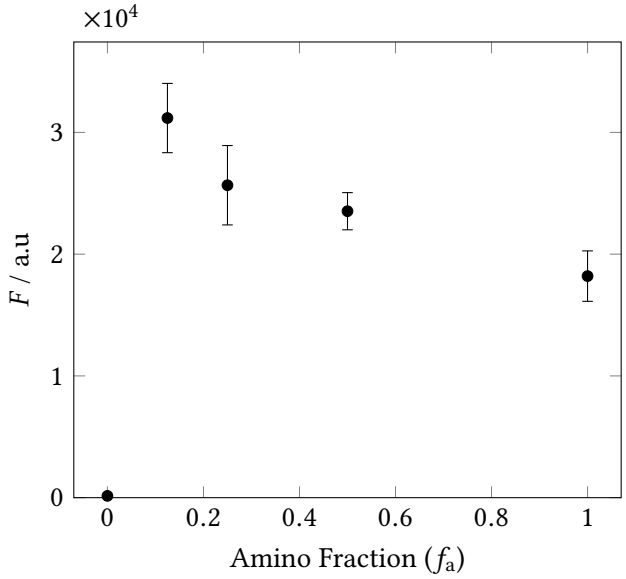

Figure 2.17: Fluorescence intensities vs the applied APTES fraction (f_a) for samples **BC1**-**BG1** λ_{Ex} = 488 nm; λ_{Em} = 550 to 600 nm)

The mixed APTES:PTMS slides were additionally labelled with **1** to yield samples **BC1**,**BD1**, **BE1**, **BF1** to **BG1**. Figure 2.17 shows the measured fluorescence intensities in comparison to the applied amino silane fraction (f_1). As already seen on previous APTES samples, F decreases with increasing amino fraction, so that it has to be assumed that even under these stronger dilutions, the content of amino groups on the surface is still too high to be accessible by fluorescence intensity determination, since fluorescence quenching hampers the measured intensities. The high uncertainty of the contact angle measurements, that was interpreted as an indication of domain formation of the individual silanes, is also found in F for **BE1** and **BF1**. The finding of similar fractions of amino groups on **BC** and **BD** in the contact angle measurements is not supported by labelling with **1**, yet this effect might be attributable to a fundamental difference in these two techniques: Whereas fluorescence serves to compare the relative *contents* of amino groups on different samples, the Cassie ratio determines the *ratios*

of two different components on one surface, without necessarily being sensitive to changes in the sum of the components. Despite those shortcomings it has to be pointed out that, in contrast to the earlier pure PTMS sample **AW1**, the background fluorescence on **BG1** amounts to only 147(62), which is only slightly elevated compared to the background fluorescence of that sample in the absence of **1** (42(8)). It can be concluded that the initial problems with VD could be eradicated through concise optimization.

2.4.2.3 Conclusion

The preparation of composite APTES:PTMS surfaces proofed to be in principle possible. However, compared to APDIPES:CETES, these surfaces appear to be of lesser quality in terms of homogeneity. Yet, the Cassie equation could again be successfully applied to achieve valuable insight in the silane ratios prepared. The surface functional groups were successfully labelled with **1** but it slowly appears to be a fundamental property of APTES based surfaces to exceed the amino group contents that can be quantified with fluorescence intensity based on label **1**. Despite being more interesting from an application based point of view, preparation of composite surfaces based on tri-alkoxysilanes does not appear to be the method of choice for the required reference density surfaces to evaluate the performance of **1**, either. The next logical step will be the preparation of different amino silane density surfaces based on two mono-alkoxysilanes.

2.4.3 Mixed mono-alkoxy silane surfaces

To ensure the fabrication of monolayer-like films, mono-alkoxysilanes apparently have to be chosen, as the tri-alkoxysilanes tend to form multilayer-type structures through self-condensation.[91,150] The silanes used here are (3-aminopropyl)diisopropylethoxysilane (APDIPES) as the functional and (3-cyanopropyl)dimethylmethoxysilane (CPDMMS)) as the inert component. The prior was demonstrated to be more than suitable for the desired purpose (Sec. 2.3.5 and 2.4.1). The latter was chosen because of its head-group which prior experiments based on CETES proved applicable because of its related chemical composition with different polarity and reactivity; it is also expected to be readily employable in mixtures with APDIPES. The different alkoxy residues are not expected to be of major concern; mixtures of chloro- and alkoxysilanes are more problematic because of the more pronounced chemical difference of the reactive Si–Cl and Si–OR motifs.[70,167] Only little work involving CPDMMS for functional surfaces was discussed so far.[168,183] A comprehensive overview of the silane structures and layer treatments is shown in Scheme 2.4.

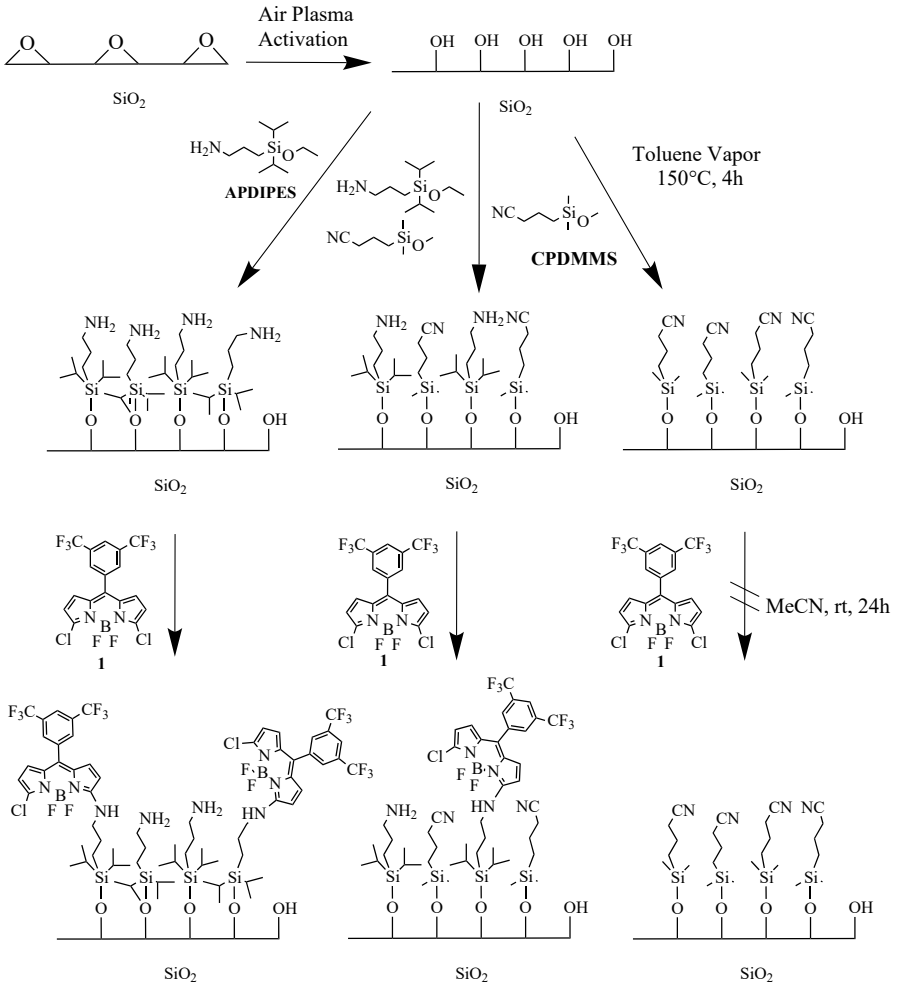

Scheme 2.4: Chemical structures of APDIPES, CPDMMS and label **1** and scheme of surface reactions

An attempt to cover a significant range of densities was made by using extremely diluted contents of amino silane: The following fractions of APDIPES with respect to the total silane content (the total silane concentration was kept at 10 % v/v in Tol) were used in the vapour deposition: 100 % (**BH**), 40 % (**BI**), 13.3 % (**BJ**), 3.3 % (**BK**), 1.3 % (**BL**), 4.4 % ¸ (**BM**), 1.1 % ¸ (**BN**), 0.4 % ¸ (**BO**), 0.1 % ¸ (**BP**) and 0 % ¸ (**BQ**). Unfortunately, an unexpected problem with the applied bottle lids occurred, as they apparently tend to soften at elevated temperatures. The bottles of **BJ** and **BM** were found open after the vapour deposition, for the remainder it is uncertain if they were sufficiently sealed throughout the process. Since these samples were prepared for scheduled ToF-SIMS experiments, a repetition of the entire experiment was not possible within the time frame and the samples were kept to see the effect of such disturbed vapour deposition.

2.4.3.1 Contact angle analysis

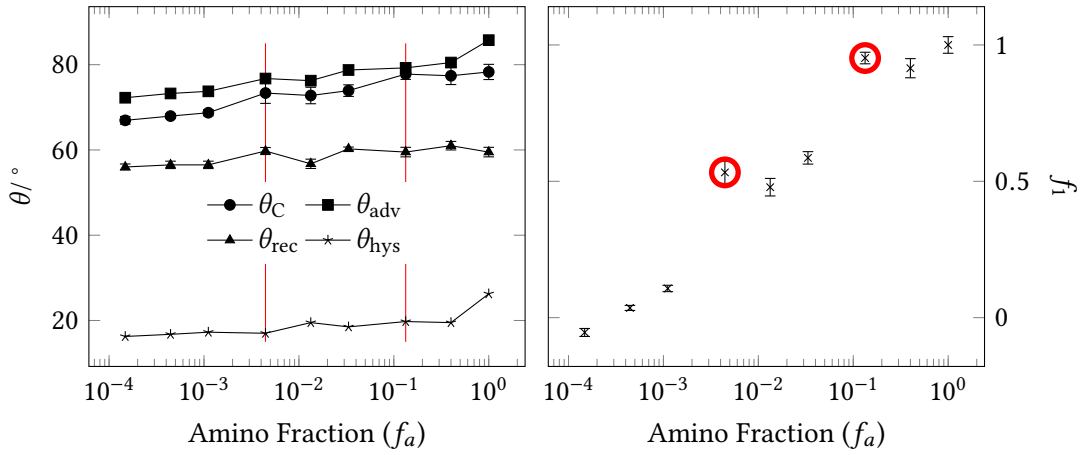

Figure 2.18: Static (θ_C) and dynamic (θ_{adv}, θ_{rec} and θ_{hys}) of mixed APDIPES/CPDMMS samples **BH-BQ** vs the fraction of APDIPES applied to the VD (f_a) and the calculated amino fraction from Cassie's Law (f_1 vs f_a); a logarithmic scale is used for f_a to account for the vast range covered; outliers due to preparation problems marked in red

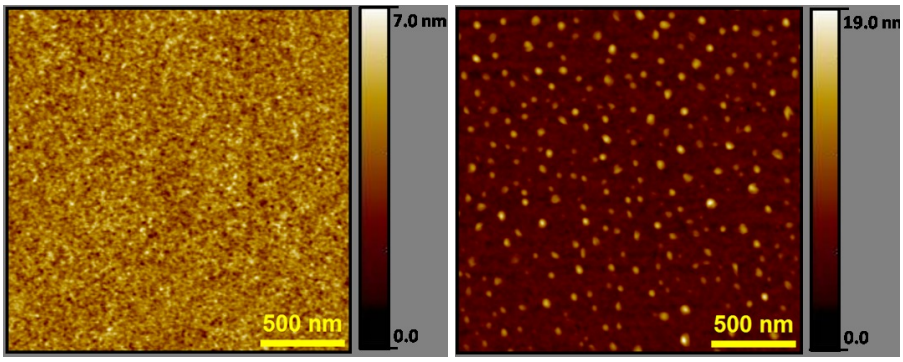

Figure 2.19: AFM images of clean glass (left) and **BH** (right)

The samples **BH-BQ** were investigated by contact angle measurements (Fig. 2.18). Due to the wide range of amino silane fractions used, the measured data are shown over a logarithmic f_a scale. It can be seen that, in agreement with the previous experiments containing APDIPES, the contact angle reduces with reducing amino fraction. θ_C spans from 78(2)° for **BH** to 66.9(9)° for **BP** and 67.5(9)° for **BQ**. θ_{adv} and θ_{rec} change nearly constantly with decreasing amino fraction, only the pure APDIPES shows a notably higher hysteresis. Noteworthy, θ_{rec} changes only slightly, indicicating that this angle is mostly governed by the polar Si–O–Si bonds, which are comparable for both silanes. The hysteresis changes from 26° for **BH** to only 15° for **BQ**.

Determination of the Cassie ratio reveals that the samples **BJ** and **BM** indeed deviate significantly from the expected trend shown in Fig. 2.18. Apart from those obvious outliers, the amino fraction seems to follow a non-linear trend, as seen earlier. However, due to the aforementioned problems during the vapour deposition, the assumptions to be drawn on the silane films based on the available methods is comparatively precarious, as the structure is not necessarily mono-layer like.

AFM images were recorded at NPL of **BH** in comparison to a cleaned glass slides, Figure 2.19 depicts one exemplary image for each sample. Whereas the clean glass slide is fairly smooth with an RMS roughness of 0.6(1) nm, it increases under strong spot formation to 1.6(2) nm if the APDIPES layer is added.

2.4.3.2 Fluorescence Analysis

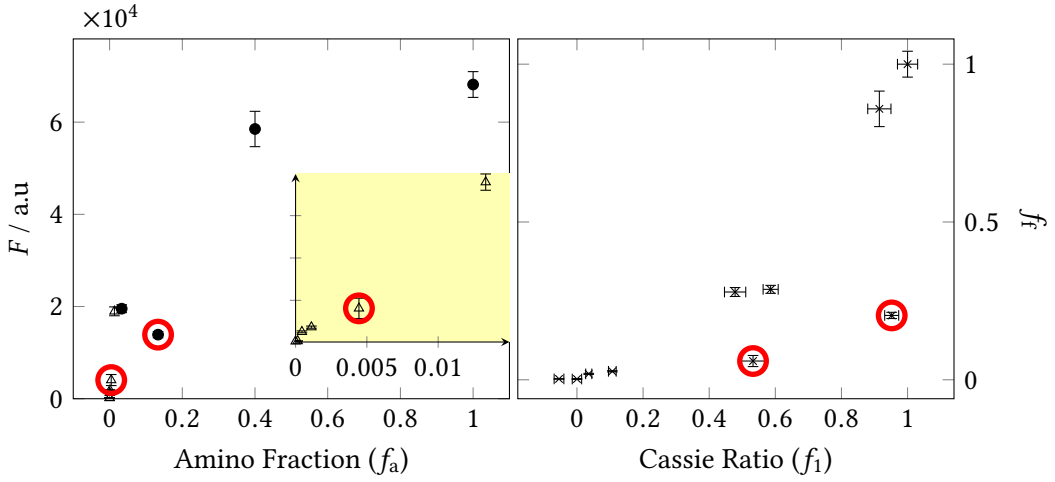

Figure 2.20: Absolute fluorescence intensities vs the applied APDIPES fraction (f_a) for samples **BH1-BQ1** (left, with magnification of the lower f_a region, λ_{Ex} = 488 nm; λ_{Em} = 550 to 600 nm) and normalized fluorescence intensity (f_f) vs the amino fraction determined by Cassie's Law (f_1) , outliers **BJ1** and **BM1** marked in red

Despite the structural shortcomings, the effect of labelling with **1** was investigated, following the previous procedure, to yield sampels **BH1**, **BI1**, **BJ1**, **BK1**, **BL1**, **BM1**, **BN1**, **BO1**, **BP1** and **BQ1**. Figure 2.20 depicts the fluorescence intensity recorded with the microarray scanner in comparison to the applied amino fraction (f_a) and the component ratio determined by Cassie (f_1). As it was previously seen for APDIPES mixtures, the fluorescence intensity (F) shows a decreasing trend with decreasing amino fraction. It is obvious that **BJ1** does not compare to the other samples. Since F is lower than expected, yet θ_C is higher, it can be tentatively assumed that exposure to air during the VD led to an oxidative decomposition of the silane. **BM1** does

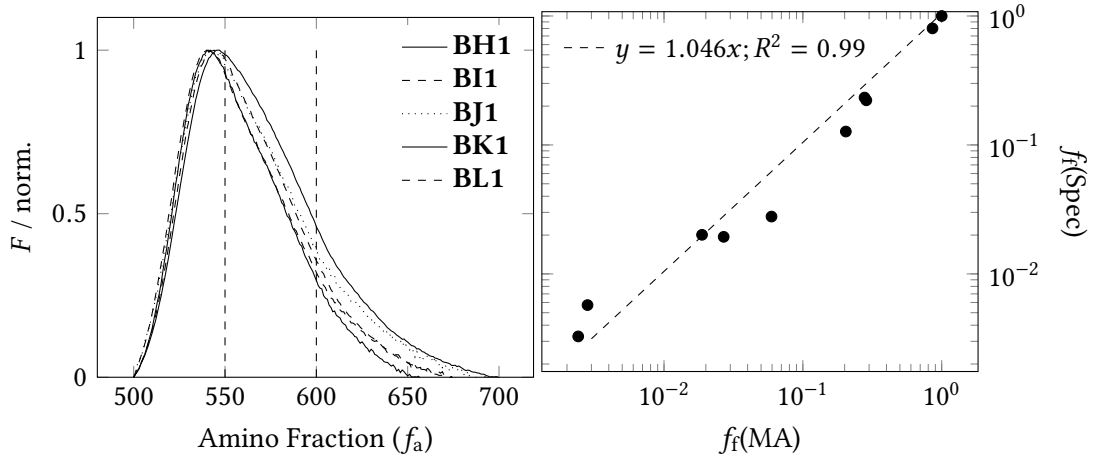

Figure 2.21: Normalized fluorescence spectra of selected samples (left, $\lambda_{Ex} = 488$ nm; dashed lines indicate integrated region for f_f(Spec)) and normalized fluorescence intensity determined by integrating steady-state fluorescence spectra (f_f(Spec)) vs the normalized fluorescence intensity recorded with the microarray scanner (f_f(MA)); including linear regression

not outlie as significantly when compared to f_a, yet the determined f_1 appears to be too high. It can be assumed that the already comparatively low content did not change significantly upon exposure to air. However, the determined f_1 is again higher than expected. Additionally, f_f does not follow f_1, even under exclusion of the obvious outlier, linearly. These findings emphasize the sensitivity of the Cassie equation to changes in the silane layer structure which makes a stringent control of the preparation prerequisite for this method to be applied.

One of the main advantages of fluorescence intensity based quantitative determination is the adaptability of the method to the available instrumentation. The currently used microarray scanner for example is an ideal instrument for quantitative measurements as it provides stable sample positioning and highly repeatable intensity measurements. The high spatial resolution down to 5 µm in combination with comparably high scanning speed of 2 to 20 min, depending on the resolution, for a single excitation wavelength and the large scan area is difficult to be found in other instrumentation. However, it is very limited in terms of sample dimension as it exclusively accepts the standard microscope slide format. Although the laser/filter combination applied in the instrument is paramount for the reliable and sensitive performance, it clearly limits the obtainable information, e.g. spectrally resolved data is hardly available, let alone temporally resolved.

To prove the versatility of the fluorescence intensity method, the samples **BH1**-**BQ1** were additionally investigated on a steady-state fluorescence spectrometer. The samples were measured in a front face geometry involving a lens collecting the emission from the surface to enhance the sensitivity and reduce the reflection background. The recorded spectra were subtracted with a blank slide reference spectra and remaining background manually corrected using a baseline approximation. Figure 2.21 shows the normalized spectra of **BH1**-**BL1**. Despite no clear sign of fluorescence quenching was seen in the intensity based measurements, a slight bathochromic shift in combination with spectral broadening can be seen for **BH1** (less for **BI1**). However, it can also be seen that this shifts the spectra into the 550 to 600 nm region, which is selected for intensity measurements in the microarray scanner. It is reasonable to assume that coincidentally, the effect of fluorescence intensity decrease due to self-quenching is partially annihilated in the measurement by shifting the spectra into the evaluated region.

Figure 2.21 additionally compares the normalized fluorescence intensity determined using the microarray scanner (f_f(MA)) with the normalized fluorescence intensity based on integrating the corrected fluorescence spectra from 550 to 600 nm (f_f(Spec)). The two different ratios show a clear linear correlation, which evinces that fluorescence intensity determination based on the steady-state spectra is possible if sufficient care is taken in background correction and sample positioning. However, as the absence of error bars indicate, the uncertainty of the method is difficult to access and generally higher than using the microarray scanner, as the time required to evaluate a single scan equals or exceeds the time required to evaluate a full scanner measurement, in which each pixel can be treated as single measurement. This yields a result based on 2×10^6 to 60×10^6 data points, whereas a the spectrometer only yields a single data point without spatial resolution.

2.4.3.3 ToF-SIMS analysis

Through a collaboration within the SurfChem project, an opportunity was given to acquire ToF-SIMS spectra of selected samples on state-of-the-art equipment at ION-TOF (Münster). The samples **BH1**-**BQ1** were selected for that task. Positive and negative ion spectra were recorded by averaging the scans over a 200 µm × 200 µm area with a pulsed Bi_3^+ beam. The scans were analysed and peaks selected that changed between the samples. Representative signals for the individual silane components were found: $SiC_4H_8N^+$ (m/z = 98.04) for CPDMMS and $SiC_3H_7O^-$ (m/z = 102.94) for APDIPES. Although not expected, a signal clearly identifying the surface labelled compound **1** was found: $C_{17}H_8N_3BClF_8^-$ with m/z = 452.03. This fragment shows an isotope pattern characteristic for a molecule containing one (not two) chlorine and one boron atom (see Fig. 2.23) which substantiates the allocation to the surface bound, meaning reacted, form of the label compound rather than the unreacted containing two chlorine atoms.

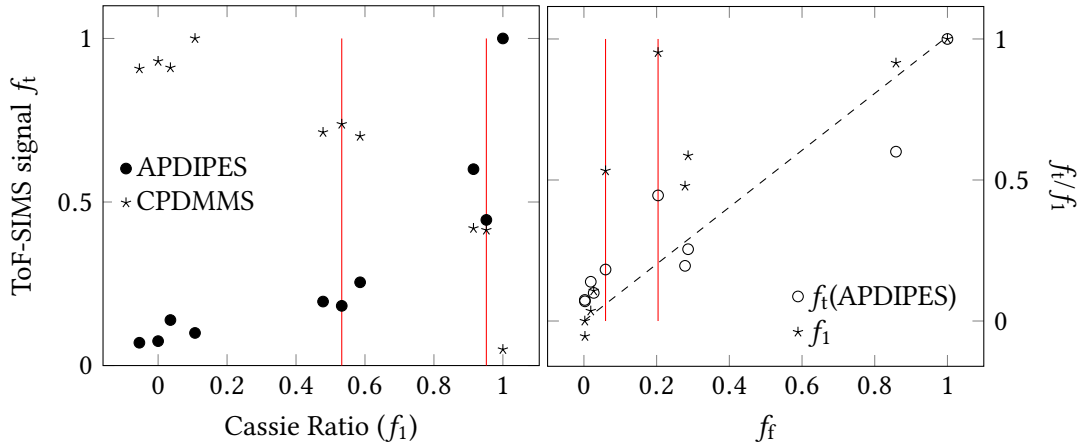

Figure 2.22: Relative signal intensities for $SiC_3H_7O^-$ (m/z = 102.94, f_t(APDIPES)) and $SiC_4H_8N^+$ (m/z = 98.04, f_t(CPDMMS)) in comparison to the amino ratio determined via Cassie's law (f_1) (left) and comparison of the (f_t(APDIPES)) and f_1 versus the normalized fluorescence intensity (f_f) ; points belonging to outliers **BJ1** and **BM1** marked by red line

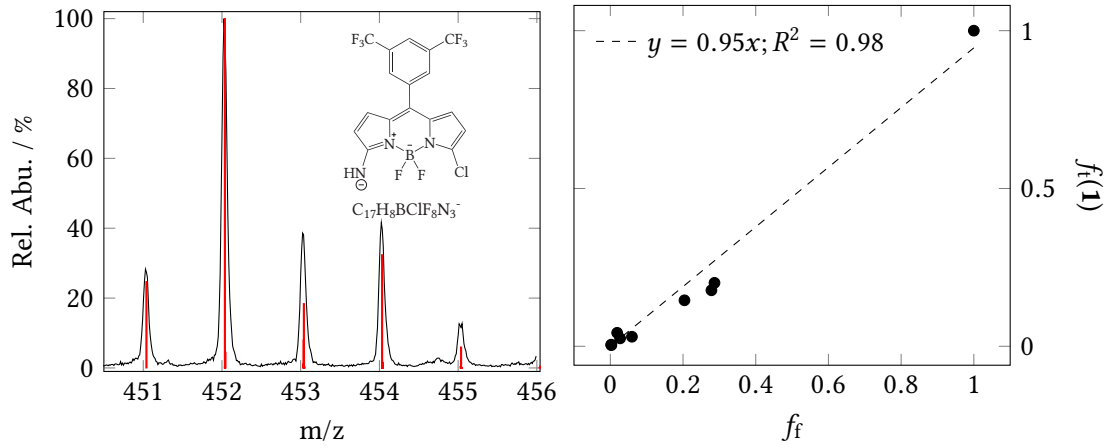

Figure 2.23: Exemplary ToF-SIMS spectrum of the surface bound **1** fragment $C_{17}H_8N_3BClF_8^-$ (m/z = 452.03) including theoretical peak intensities (red) (left) and relative signal intensity for this fragment vs the fluorescence ratio (f_f)

The signal intensities of the relevant fragments were evaluated by integrating the respective mass peak area. As the different fragments show strongly differing ion yields, the intensities were normalized with respect to highest signal of each sample set. In analogy to the component fraction determined by fluorescence (f_f), the normalized intensities are treated as component fraction of the respective component (f_t). Given that the surfaces compose of a binary system, the sum of the two components should be one, if the individual traces can be treated as component fraction and indeed, it is found that f_t(APDIPES)+f_t(CPDMMS) = 0.98(7) for all samples. Figure 2.22 depicts the traces for both components versus the amino ratio determined by Cassie's Law (Eq. 2.3). f_t(APDIPES) increases with increasing f_1 and f_t(CPDMMS) decreases accordingly. However, as shown in Figure 2.20, the Cassie ratio has to be treated with care on these samples. The fraction determined by fluorescence labelling (f_f) is probably more suitable, although being affected by the deviation of sample **BJ1**. Accordingly, Figure 2.22 also compares f_1 and f_t. The amino component ratio determined from the ToF-SIMS signals obviously shows a significantly higher correlation with f_f than f_1, roughly following a linear relationship. Additionally, the offset of samples **BJ1** and **BM1** is less severe for f_t(APDIPES) vs f_f. This shows the potential that carefully analysed ToF-SIMS measurements hold in understanding composite organic surfaces on glass. The fragment allocated to label **1** was extracted from the sample spectra in a similar fashion to the previous fragment to yield the component fraction f_t(**1**). Unfortunately, an experimental error lead to a false orientation of **BI1** during the measurements that resulted in this sample being measured on an area unreacted with dye. Accordingly, this point is excluded from analysis. Figure 2.23 shows the correlation between f_t(**1**) and f_f which can be satisfyingly approached with a linear regression. Noteworthy is the relatively good correlation in the lower f range, which shows that the sensitivity of ToF-SIMS is, in contrast to XPS, comparable with the fluorescence intensity measurement.

2.4.3.4 Conclusion

The results obtained from samples **BH**-**BQ** prove the feasibility of the composite surface preparation using mixed silane solution comprised of mono-alkoxy silanes. However, the limits of contact angle based analysis of such surfaces are also encountered: interpreting these measurements in terms of chemical composition is only possible if the parameters affecting the contact angle are kept constant between the different samples. Paramount for this condition to be met is ambient control of the vapour deposition and optimization of the applied material.

The fluorescence intensity based analysis could be enhanced instrumentally by front-face measurements on a steady-state spectrometer, proving the versatility of the fluorescence method. The application of further instrumentation like fluorescence microscopy is envisioned.

The mass-spectrometric analysis using ToF-SIMS was found to show very promising results. Although the analysis of these measurements is significantly more demanding, as is the acquisition, compared to XPS, fluorescence or contact angle measurements, the method provides insight into the chemical structures on the surface beyond the capabilities of XPS, especially in terms of sensitivity. The matrix effects that usually limit the application of ToF-SIMS for quantitative analysis are of lesser concern for the composite silane samples as they apparently are for the contact angle measurements. Detailed studies with a more stringent combination of the different analytical methods promise potential in applying ToF-SIMS, with its wide-spanned dynamic range, as a bridge between XPS and fluorescence, as it would allow to transfer absolute quantification obtained from an elemental surface analysis onto the linear range of the fluorescence intensity measurement of labelled surfaces species.

2.5 Dual-Mode labelling on variable functional group density surfaces

The work presented in this chapter was published in ref. 65. As the previous section has shown, controlled surface functionalization with two different monoalkoxy silanes is feasible. Based on the new protocol for silane-derived surface functionalization, it is possible to produce monolayers with a controlled density of functional groups in a simple one-step co-deposition process of a binary silane mixture. In contrast to previous work,[77,154,159] this method enables the control over a wide range of densities in a single step (see Scheme 2.4).

The combination of APDIPES and CPDMMS proved suitable for this process, if rigorous humidity control is employed during the vapour deposition.[78,184] The characterization of the ratio of silanes actually bound to the surface can then be performed in a facile manner through contact angle (CA) measurements using the Cassie equation.[181,182] For an estimation of the number of surface functional groups, labelling with **1** allows quantification by fluorescence and chemical derivatization XPS (CD-XPS) on one and the same sample.[88] Application of **1** to the mixed-silane layers revealed that fluorescence and XPS can show comparable results, allowing for a direct linking of quantitative fluorescence analysis to XPS quantification. As XPS yields relative atomic compositions of the analysed surfaces, reference-free total reflection total reflection X-ray fluorescence spectroscopy (TXRF) can be employed for traceable quantification of nitrogen in the silane layer and, based thereupon, of surface amino groups. The TXRF measurements were performed and analysed by Cornelia Streeck and Andreas Nutsch from PTB. The approach enables absolute calibration of XPS which may be used to finally provide an absolute reference for quantitative fluorescence measurements through a traceable measurement chain.

The key to surfaces with monolayers of controlled molecular composition prepared from more than one chemical precursor is a deposition procedure that yields a homogeneous distribution of the partners on the surface without clustering or domain formation. For a better understanding of the characteristics of single-silane layers prepared from the individual reagents with respect to the mixed layers, pure APDIPES and CPDMMS reference films were deposited on glass and silicon and analysed by atomic force microscopy (AFM), CA measurements, SR-XPS and TXRF.

2.5.1 Single-silane layers

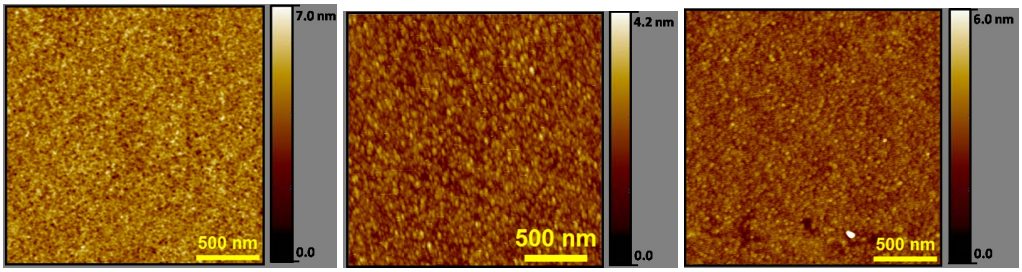

Figure 2.24: AFM images of clean glass (left), **CC** and **CL** (right)

2.5.1.1 AFM

To ensure that a different lid to the bottles, made of rigid poly(p-phenylene sulfide) (PPS) indeed provides the conditions required for dry vapour deposition, the pure silane samples were investigated with AFM. The microscopic topographies of the glass slides individually functionalized with APDIPES (**CC**) or CPDMMS (**CL**) show no remarkable differences to the bare substrate and to each other as disclosed (Fig. 2.24). This indicates dense monolayer formation with RMS roughnesses <0.70 nm, in contrast to prior experiments. Further characterization of the slides with CA measurements revealed that the surface with the 100 % APDIPES film is significantly less polar than the pure CPDMMS surface with a static contact angle of 97(3)° vs 75(4)°, respectively. This reduced polarity is attributed to the higher hydrophobicity of the isopropyl groups of APDIPES compared to the methyl residues of CPDMMS.[91] Especcially in contrast to the prior experiment with these two silane, a significant increase in quality was obtained.

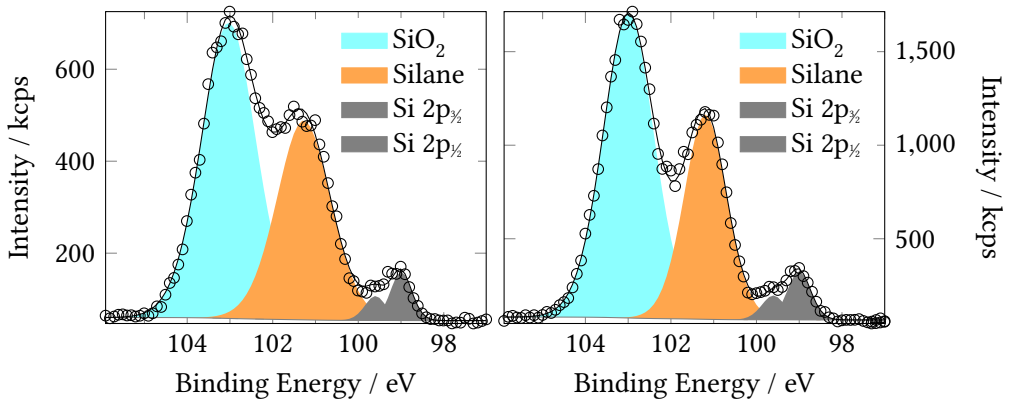

Figure 2.25: Fit of the measured Si 2p core-level spectrum recorded on a pure APDIPES (left) or CPDMMS (right) layer on oxidized silicon at $z_{95} \approx 1.2\,\text{nm}$ ($h\nu = 210\,\text{eV}$, $\theta = 60°$) including the Si 2p components Si_0 (Si wafer), $R_3Si(O)_1$ (silane), and SiO_2 (native oxide on Si wafer).

2.5.1.2 SR-XPS

For a better chemical insight into the single-silane layers, SR-XPS measurements were performed by Paul Dietrich from BAM, allowing for maximum surface sensitivity and the clear differentiation of silane, oxide, and silicon substrate-related components in highly resolved Si 2p spectra of pure APDIPES and CPDMMS films. Maximum surface sensitivity here means that the information depth z_{95} (see ref. 60) was as low as 1 nm when using an excitation energy of 210 eV and an electron emission angle of 60° with respect to the surface normal.[58,60] The Si 2p core-level spectrum of a pure APDIPES layer on oxidized silicon is shown in Figure 2.25 which demonstrates the ability of SR-XPS to provide information about different coexisting silicon species within silane monolayers on oxidized silicon surfaces.

Here, elemental silicon Si^0 at a binding energy of 99.0 eV is a minor species and the main peak at ~103.0 eV originates from the native oxide layer (SiO_2).[45] Additionally, the presence of a third component at ca. 101.3 eV is evident. This component, belonging to $R_3Si(O)_1$, is assigned to the central silicon atom of the employed silanes, anchoring them to the surface by a siloxane (Si–O–Si) bond.[34,152,185] The component peak areas of SiO_2, $R_3Si(O)_1$ and Si^0 are 56.1 %, 38.4 % and 5.5 %, respectively. Si 2p core-level spectra with comparable component peak areas (SiO_2 59.8 % $R_3Si(O)_1$ 33.6 %, and Si^0 6.5 %,) were obtained for the pure CPDMMS layers. Simulations of the Si 2p core-level spectra using SESSA software[186] can be used to estimate thicknesses of single-silane layers, yielding values of 0.8 and 0.5 nm for the APDIPES and CPDMMS films, respectively.[65] The obtained overlayer thicknesses correspond well to reported data on aminosilane layers and clearly suggest monolayer formation.[91] According to Shircliff et al., the silane surface density can be estimated from the fraction of the $R_3Si(O)_1$ component peak area related

to the total Si 2p peak area.[34,68,152] This approach of considering only SiO_2 and silane species can be applied in our case since the ~5 % Si_0 contributions can be neglected. From the XPS data surface densities of 3 and 4 molecules nm^{-1} were determined for APDIPES and CPDMMS, respectively, using the measured $R_3Si(O)_1$ Si 2p component peak area.[65] Comparable silane surface densities of 2 molecules nm^{-2} for both APDIPES and CPDMMS were estimated from the silane layer thicknesses.[68] Obviously, both methods yield reasonable values for the silane surface density when compared to the reported number of silanol groups available for silane attachment on silica surfaces.[151]

2.5.1.3 XPS

Table 2.12: Laboratory XPS compositional data of pure APDIPES and CPDMMS silane layers on glass

	C 1s at%	N 1s at%	O 1s at%	Si 2p at%	F 1s at%
APDIPES	18.8	1.0	55.7	24.6	0
CPDMMS	13.9	1.0	59.2	25.9	0

Laboratory XPS measurements of the single-silane surfaces on glass are in good agreement with those on oxidized silicon. Compared to an APDIPES surface, APDIPES containing a higher stoichiometric amount of carbon, CPDMMS shows a lower relative carbon content (Table 2.12). Silicon and oxygen signals are dominated by substrate contributions, since these elements are major glass components (other substrate-related elements like Na and Ca are also visible in the XPS spectrum, but were not considered for analysis since they do not provide significant information). Both signals show a stronger attenuation for APDIPES which is consistent with the higher layer thickness of APDIPES compared to the CPDMMS layer.[46]

From the results obtained individually for both silanes it can be concluded that application of APDIPES and CPDMMS under rigorously controlled atmosphere results in a similar surface coverage close to a monolayer. The only difference is the slightly increased thickness of the APDIPES layer (0.8 vs 0.5 nm) which is ascribed to the isopropyl moieties forcing the 3-aminopropyl unit to point away from the surface (see Figure 2.31b for an illustration). In contrast, CPDMMS is more comparable to (3-aminopropyl)dimethylethoxysilane with a reported thickness of 0.6 to 0.7 nm.[34,91] To verify the comparability of the system on glass and SiO_2/Si and to provide a traceable amount for the number of functional groups on single-silane-modified glass slides and silicon wafers reference-free TXRF was employed. The functional groups were

quantified via the amount of nitrogen, as nitrogen is the only constituent exclusively found in the functional silanes, but not in the substrates themselves. For all single-silane films, i.e., APDIPES and CPDMMS on glass as well as silicon, a constant value of 2 to 3 functional groups per nm^2 was determined using the measured absolute mass deposition of nitrogen giving 2 to 3 atoms per nm^2.

2.5.2 Mixed-silane layers

2.5.2.1 Contact angle measurement

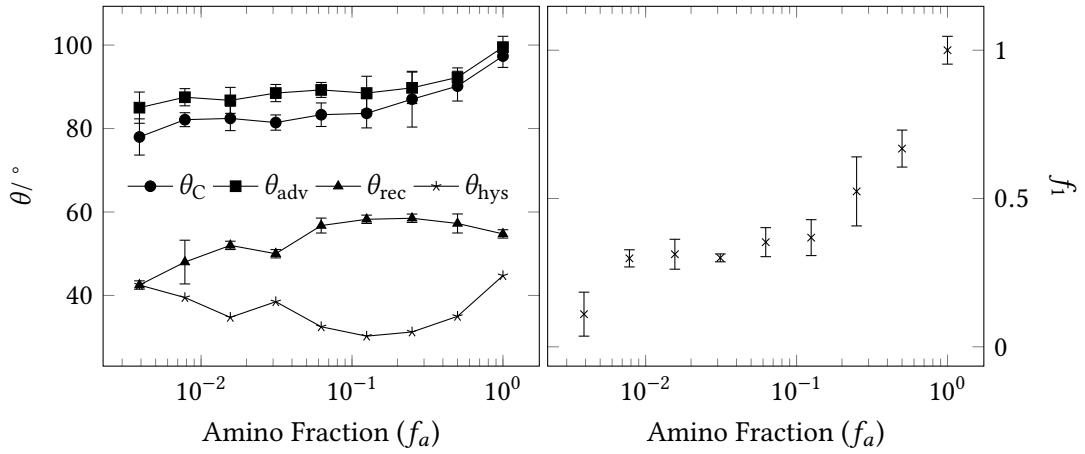

Figure 2.26: Static (θ_C) and dynamic (θ_{adv}, θ_{rec} and θ_{hys}) of mixed APDIPES/CPDMMS samples **BH-BQ** vs the fraction of APDIPES applied to the VD (f_a) and the calculated amino fraction from Cassie's Law (f_1 vs f_a); a logarithmic scale is used for f_a to account for the vast range covered

The central aspect of this work is the control of the surface functional group density. A batch of eight different glass slides with silane films originating from the CVD process at various ratios of APDIPES:CPDMMS, namely 50 % (**CD**), 25 % (**CE**), 21.5 % (**CF**), 6.25 % (**CG**), 3.13 % (**CH**), 1.56 % (**CI**), 0.78 % (**CJ**) and 0.39 % (**CK**) of APDIPES relative to the total silane content was thus prepared.

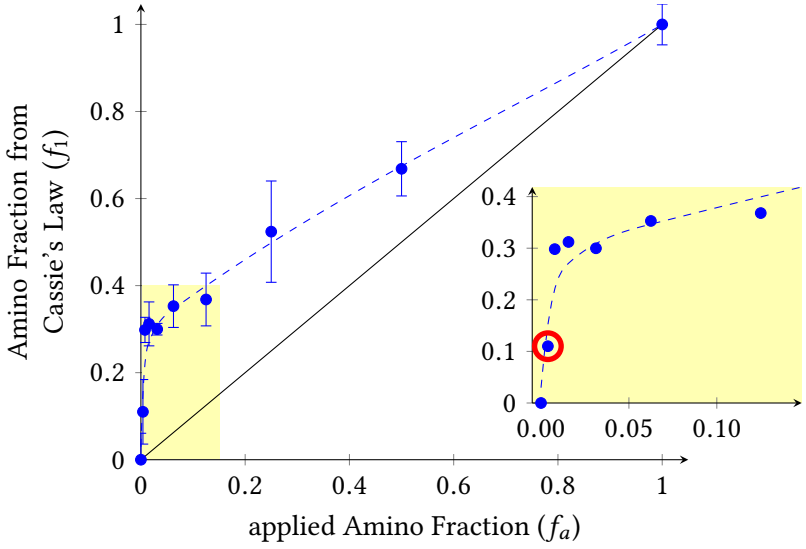

Figure 2.27: Amino fraction calculated from the static contact angles (f_1) vs the fraction applied in CVD (f_a) (dotted line as guide to the eye, black line would correspond to an ideal ratio of f_1/f_a with a slope of 1); magnification of the region with $f_a \leq 12.5\,\%$ in inset, the entry marked red corresponds to a frustrated APDIPES sub-monolayer when too few silane is offered, see text for explanation (right)

The slides were first characterized and compared by CA measurements. The contact angles of the different dilutions lie between those of the single-silane samples, i.e., between 97(3)° for **CC** and 75(4)° for **CL**. Again, the contact angles do not correlate in a straightforward manner with the applied silane ratio. It can be assumed that differences in binding kinetics of the two silanes are the main reason for the observed behaviour, a lack of literature data on CPDMMS precluding a closer assessment. However, especially amino silanes are known to react very rapidly with silica surfaces.[150,156] To estimate the ratio of the two silanes, Cassie's Law (Eq. 2.4) was again employed.

$$\cos\theta_c = f_1 \cos\theta_1 + f_2 \cos\theta_2 \tag{2.4}$$

Those fractions directly relate to the chemical ratios, as other parameters affecting the contact angle like surface morphology or density of surface modification – very similar surface coverage has been found for both species, vide supra – have not been altered in the experiments and are thus identical for both silanes, in contrast to prior experiments in this work. In addition, quantification of the nitrogen content of a mixed-silane surface via TXRF supports this assumption, yielding coverages of two silanes nm^{-2}, in excellent agreement with the TXRF results on the single-silane films. Figure 2.27 shows how the calculated amino fraction (f_1) and

the amino fraction applied in the VD experiments (f_a) correlate. Presumably due to the different reaction kinetics of the two silanes, and under the assumption that aminosilanes react faster with surface silanol groups than cyanosilanes, the fraction of aminosilanes on the surface exceeds that of the aminosilanes employed. The behavior shown in Figure 2.27 suggests that two major steps are involved in the formation of the composite silane layer. Approaching the data from 100 % CPDMMS (**CL**, $f_a = 0$), an increase in aminosilane fraction up to 12.5 % (**CF**) leads to the formation of an APDIPES sub-monolayer of rather constant constitution with an APDIPES coverage of ~30 %, when the surface created upon application of pure APDIPES (**CC**) is taken as the 100 % reference. A further increase in the silane ratio beyond $f_a > 12\,\%$ then leads to the completion of the (mixed) monolayer with an apparently linear dependence on the ratio of both silanes. Only for the lowest applied silane ratio of **CK** ($f_a = 0.4\,\%$), which corresponds to APDIPES:CPDMMS 0.4:99.6, does the initially observed behaviour deviate from the constant value of $f_1 \approx 30\,\%$ (red circle in Figure 2.27). Obviously, the very minor amount of APDIPES employed in that reaction is too little for the surface area offered to create an apparent monolayer under the preparation conditions employed. Based on a model illustrated in the Figure 2.31 the tentative assumption is that before binding to the surface, the aminosilane coordinates primarily with its amino group to the silanol groups on the surface.[91,135,150,158,177,179] This step is eventually followed by alcohol-water condensation of another surface silanol group with the ethoxy moiety of APDIPES, releasing ethanol and forming the Si–O–Si bond to covalently anchor the silane at the surface. It is reasonable to conclude that the initial coordination step facilitates bonding of APDIPES over CPDMMS. However, upon reaching ~30 % coverage, steric hindrance might prevent further condensation according to this model (Figure 2.31d). The amino groups of the surface-bound silanes rather coordinate to the oxygen of the RCH_2–O–Si bond of an approaching silane and promote the condensation reaction when the latter's alkoxy residue is facing the surface.[150,170] This step seems virtually independent of the terminal residue and follows the stoichiometric ratio of the vapour. It has to be kept in mind that the information obtained by CA measurements allows only a relative comparison (with considerable error) of the samples.

2.5.3 Dual-Mode XPS and fluorescence quantification

A chemically more significant and reliable (yet indirect) approach of characterization that allows for the comparison of functional group densities is based on the chemical labelling of a specific type of surface entity, amines in this case. When a dual-mode label such as the amino-specific fluorophore **1** (Scheme 2.4) is available, quantitative surface chemical analysis by both XPS and fluorescence techniques is possible.[88] Since reliable fluorescence intensity measurements on silicon could not be obtained and are in general difficult to interpret quantitatively because of interference effects at the SiO_2/Si interface,[169,187–189] XPS was used to provide comparable data for silane films on both materials. Table 2.13 summarizes fluorescence and XPS data obtained for the glass slides.

2.5.3.1 Fluorescence

The 100 % APDIPES film shows an intense fluorescence signal for excitation at 488 nm, whereas very minor fluorescence originates from non-specifically bound marker molecules on the 100 % CPDMMS film. For the mixed silane films, the fluorescence intensity reduces with a reduction in the fraction of amino groups f_1 in the film on the surface. This points to little to no fluorescence quenching occurring for this sample, in line with the previously reported findings. Additionally to the results obtained from microarray scanning, a selection of **1** labelled samples was re-measured using an epifluorescence microscope. The correlation between the relative intensities obtained by both techniques is shown in Figure 2.30. Noteworthy are the significantly higher errors obtained from quantitative fluorescence microscopy analysis, which mainly result from variances in illumination power and focussing on the sample. These errors do not occur in the microarray scanner. Additionally, the shown data for the microscope stem from three different areas of ~500 µm × 500 µm, whereas the entire surface of the slide can be analysed in the fluorescence scanner.

2.5.3.2 XPS

Comparing the XPS results of the APDIPES film without (Table 2.12) and with (Table 2.13) label **1**, the atomic fraction of carbon increases after labeling and organic fluorine appears. The atomic fractions of carbon and organic fluorine then decrease with a decreasing amino group fraction. Pure CPDMMS films treated according to the labelling procedure finally show the absence of a fluorine signal. Based on the atomic fractions of C and F of **1** compared with the silanes (Scheme 2.4), such a behaviour is expected when fewer reactive surface functional groups for anchoring of **1** are offered thus leading to a reduction in the amount of surface-bound **1**. Accordingly, because the dye mainly contributes carbon yet the nitrogen content of

Table 2.13: XPS (elemental atomic fractions in at%) and fluorescence scanning (normalized intensities, I_f) data for glass slides vs amino group fraction (f_a) in the mixture used for film deposition, reacted with label **1** (amino group fractions f_1 determined by CA measurements are included for comparison)

Sample	f_a	f_1	C 1s	N 1s	O 1s	Si 2p	F 1s (CF_3)/(F^-)	f_f
CC1	1.00	1.0	21.0	1.3	52.7	24.1	0.8/0.2	1.00
CD1	0.5	0.7	16.4	1.3	56.0	25.7	0.5/0.1	0.67
CE1	0.25	0.5	18.0	1.1	55.1	25.2	0.4/0.1	0.43
CF1	0.13	0.4	15.0	1.3	57.1	26.1	0.3/0.1	0.31
CG1	0.06	0.4	13.2	1.3	58.4	26.7	0.3/0.1	0.27
CH1	0.03	0.3	13.8	1.4	57.8	26.6	0.3/0.1	0.19
CI1	0.015	0.3	13.9	1.4	57.7	26.7	0.3/0.1	0.20
CJ1	0.008	0.3	13.9	1.4	58.0	26.4	0.3/0.1	0.19
CK1	0.004	0.1	14.2	1.5	57.7	26.5	0.1/0.0	0.12
CL1	0.00	0.0	12.3	1.5	59.3	26.9	0.0/0.0	0.01

CPDMMS and APDIPES is similar, a *reduction* in the labelling rate is also reflected in an *increase* of the nitrogen atomic fraction. A similar trend is found for the atomic fractions of oxygen and silicon which belong to the substrate and indicate a decreasing thickness of the organic surface layer, again especially in comparison to the pure APDIPES film not labelled with **1** (Table 2.12). As the glass contains varying trace amounts (around the limit of detection) of fluoride, F 1s core-level spectra were recorded for each sample and the contribution of organic fluorine (belonging to the CF_3 groups of **1**) and inorganic fluoride (F^-, the F atoms of the BF_2 group and the background contribute to this signal) were determined by peak component fitting (Figure 2.28). The total F amount determined from the survey scan was allocated to F_{CF_3} and F_{F^-} based on the peak area ratio obtained from high-resolution F 1s XPS spectra.

For a determination of the amino group fraction from the XPS results, the F_CF_3/N ratio can be used. The fraction of amino groups reacted with dye **1** ($x_{NH+\mathbf{1}}$) can be calculated taking the mass balance $Si(C_3H_7)_2{-}(CH_2)_3{-}(NH_2)_y + y(CF_3)_2C_6H_3(C_9H_4BF_2N_2)Cl_2 \longrightarrow HCl + C_{9+17y}N_{1+2y}(F_{CF_3})_{6y}B_y(F_{F^-})_{2y}H_{21+7y}Cl_y$ (see Scheme 2.4) for this reaction into account (Eq. 2.5).

$$x_{NH+\mathbf{1}} = \frac{F_{CF_3}}{(6[N] - 2[F_{CF_3}])} \tag{2.5}$$

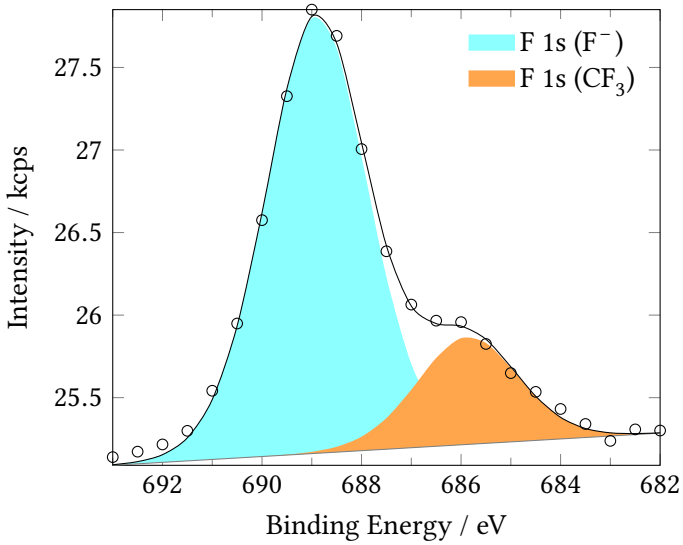

Figure 2.28: High-resolution F 1s core level spectrum of a 100 % APDIPES film on glass labeled with dye **1**

Here, [N] is the nitrogen atomic fraction content and $[F_{CF_3}]$ the atomic fraction of organic fluorine (both in at%) which are obtained from XPS survey combined with high-resolution F 1s spectra. The coupling yield calculated as fraction of dye-labelled amino groups compared to the total amount of amino groups is then obtained to $x_{\mathrm{NH^+}\mathbf{1}} = 0.12$ for $f_1 = 1$ (100 % APDIPES). This value is rather low and likely limited by the reaction itself rather than by steric crowding on the 100 % APDIPES surface (Figure 2.31a). It is thus reasonable to conclude that the coupling efficiency is independent of the amino content of the surface and important to note that quantitative labelling is neither wanted nor required here, because high dye densities would result in significant self-quenching.

The assumption of a constant coupling efficiency allows the calculation of the amino group fraction f_x of the remaining samples from XPS data according to Eq. 2.6:

$$f_x = \frac{6[\mathrm{N}] \cdot x_{\mathrm{NH^+}\mathbf{1}} - 2[\mathrm{F}_{\mathrm{CF_3}}] \cdot x_{\mathrm{NH^+}\mathbf{1}}}{[\mathrm{F}_{\mathrm{CF_3}}]} \tag{2.6}$$

On the basis of a constant coupling yield, for the fluorescence data, the normalized intensity (norm. I_f in Table 2.13) is also directly correlated with the amino group fraction (f_f). Figure 2.29 shows a plot of f_x and f_f vs the amino fraction f_1 determined from Cassie's Law, revealing the good agreement of the ratios obtained by the different methods. To the best of my knowledge, this is the first time that the determination of variable amounts of surface functional

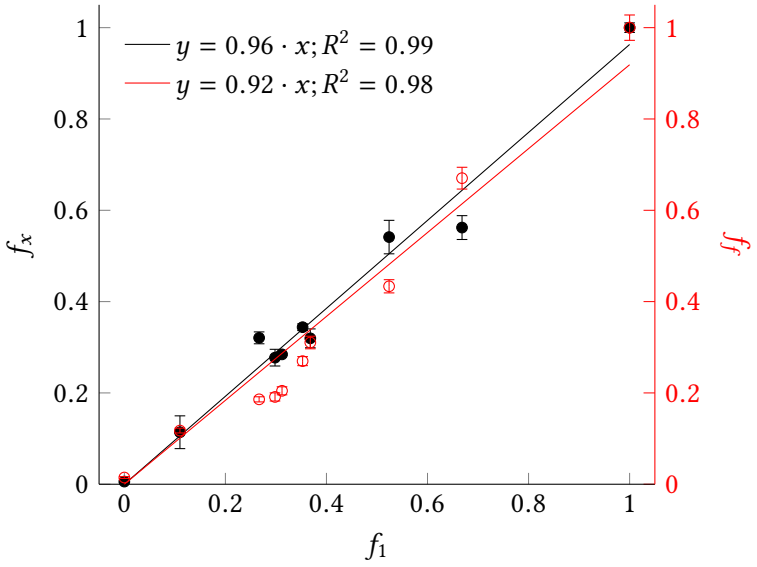

Figure 2.29: Amino fraction calculated from XPS F/N ratios after labelling with dye **1** (f_x; see Eq. 2.6; black) and normalized fluorescence (f_f; red) vs fraction (f_1) derived from Cassie's law

groups was performed by using a single label for both fluorescence and XPS measurements. To confirm the method of determination of f_x and to obtain information about the robustness of our XPS approach, the labelled samples measured with the laboratory XPS at BAM were measured again after two months of storage with a laboratory XPS at National Physical Laboratory (NPL), and the data were evaluated with the same procedure. The resulting ratios were found to be in good agreement with the initially determined f_x values (Figure 2.30). [The **1** labeled APDIPES/CPDMMS layers showed excellent stability when stored at −18 °C under an Ar atmosphere with unaltered fluorescence intensities over more than 4 months.] For XPS, the LOD for the functional group determination can be retrieved from the general LOD for fluorine in XPS (0.1 at%) to be around 0.2 amino groups per nm^2 which is the same for reference-free TXRF, here mainly limited by the superposition of the oxygen signal in the spectra. The LOD for optical fluorescence measurements significantly depends on the sensitivity of the instrument used. For the microarray scanner in this study, the LOD was determined to ca. 0.04 amino groups per nm^2 based on the background fluorescence of the 100 % CPDMMS sample after treatment with **1**. The linear range depends on the maximum label density that can be achieved. For fluorescence, self-quenching of fluorescence at high labelling densities generally has to be considered as an additional factor of uncertainty.[81] APTES was shown to form multilayers of higher thickness (roughly 2 nm from XPS)[46] because of pronounced crosslinking through the three alkoxy groups. Circumventing this limitation of self-quenching with the present silanization approach renders this technique even more advantageous. The amino

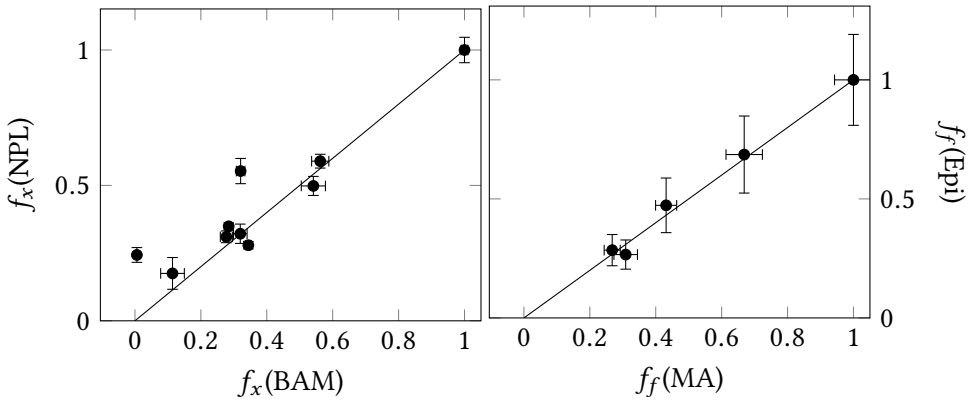

Figure 2.30: Amino silane fraction determined from re-measured data (f_x(NPL)) vs original determination (f_x(BAM)) (left) and fluorescence fractions determined from normalized intensities obtained from Epifluorescence Microscopy (f_f(Epi)) vs the fluorescence fraction obtained from microarray scanning (f_f(MA)) (right)

ratio determined by fluorescence is thus not limited by the measurement but only by the repeatability of the labelling, with the analysis times being fast (<2 min per sample) and sampling statistics excellent (72 mm × 22 mm at 20 µm resolution). Moreover, SR-XPS and reference-free TXRF methods enable an absolute determination of the functional group density on samples which can then be used as transfer standards for the other laboratory-based methods.

The application of ToF-SIMS could only be endeavoured on an older instrument at NPL. Unfortunately, the previously encountered fragments could not be measured with a sufficient signal-to-noise ratio, probably due to a lower sensitivity of the older analyser. Although comparative analysis of the spectra found signals following the expected intensity change, no reasonable fragments could be allocated to those signals.

2.5.4 3D representations of the surfaces

Based on the results concerning the silane and dye labelling density, the following 3D graphics were created to illustrate the surface structures and processes. The model substrate is a fully oxidized Si surface sized 2.2 nm × 2.5 nm. Figure 2.31a shows **1** (highlighted in green) bound to a pure APDIPES surface (SiOH substrate in turquoise). It can be seen that even at this highest density the dye has enough space to avoid dye-dye interactions. Figures 2.31b and 2.31c show APDIPES and CPDMMS surfaces at high silane density, respectively. Figure 2.31d shows a free APDIPES (highlighted in blue) approaching a surface with ~30 % silane coverage.

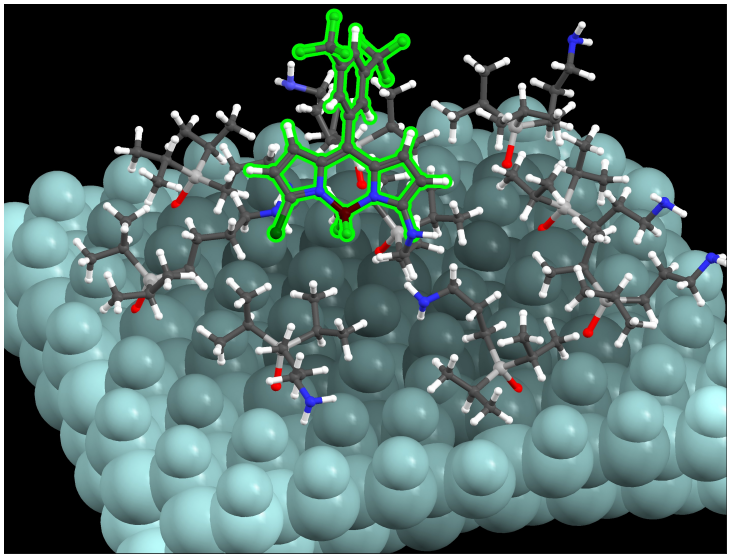

(a) 1 on pure APDIPES surface

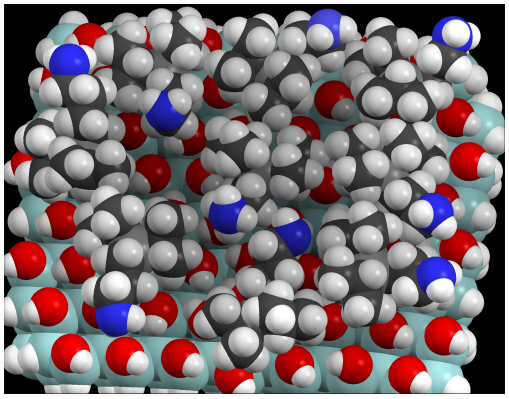

(b) Pure APDIPES surface

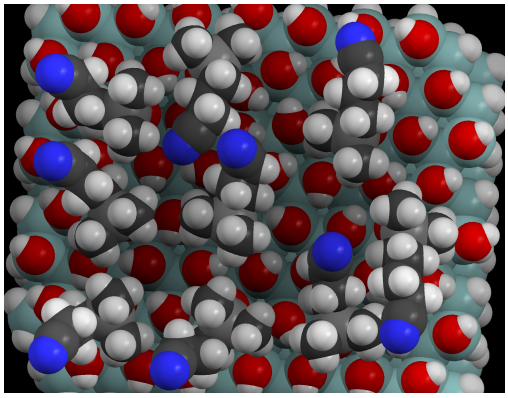

(c) Pure CPDMMS surface

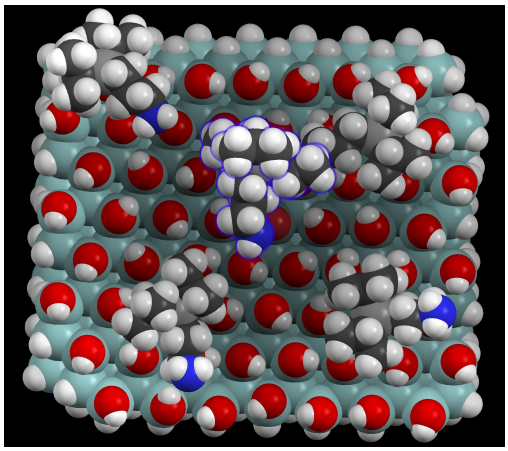

(d) Reduced APDIPES surface

Figure 2.31: 3D representations of different silane surfaces

2.5.5 Conclusion

The co-deposition method of surface modification finally allows the control of the functional amino group density of silane monolayer-like systems by simple dilution with a second, chemically closely related yet inert silane employing a rather facile CVD preparation process. In addition, careful analysis of a series of mixed monolayers by various analytical techniques allowed the deduction of first mechanistic insight into the formation process of such deposited layers, which however needs to be verified and refined with other appropriate methods. The application of the dual-mode label **1** enables a detailed quantification via XPS and allows the transfer of this quantification to readily available fluorescence measurements, which can be performed on a number of different instruments. The XPS results were verified by independent repetition and combination with reference-free TXRF allowed for a traceable calibration, finally linking a high-throughput, fast fluorescence scanning approach to these quantitative methods. These experiments have exemplary shown the potential of the combination of surface analytical techniques with appropriate labels and surface chemistry for some of the most widely used surfaces, i.e., aminated glass supports.

2.6 Multimode Surface Functional Group Determination: Combining Steady-State and Time-Resolved Fluorescence with X-ray Photoelectron Spectroscopy and Absorption Measurements for Absolute Quantification

The work presented in this chapter was published in ref. 190. The previous section finally introduced a simple and robust vapour deposition method for the preparation of surfaces with variable functional group density.[65] These surfaces were employed in the verification of the performance of a dual-mode label dye that enables the correlation of fluorescence intensity measurements with XPS contents via the unique fluorine content of the dye. Although the mono-alkoxy silanes employed for our previous study, APDIPES and CPDMMS, provided smooth monolayers with comparable silane density, such layers are only seldomly used in actual (bio)chemical applications of functional slides.[34] The by far most commonly employed silane for amino surfaces is APTES that, due to its three alkoxy residues, is known for its challenging binding chemistry and the formation of multi-layer like structures.[42,66,78,91,135,143,144]

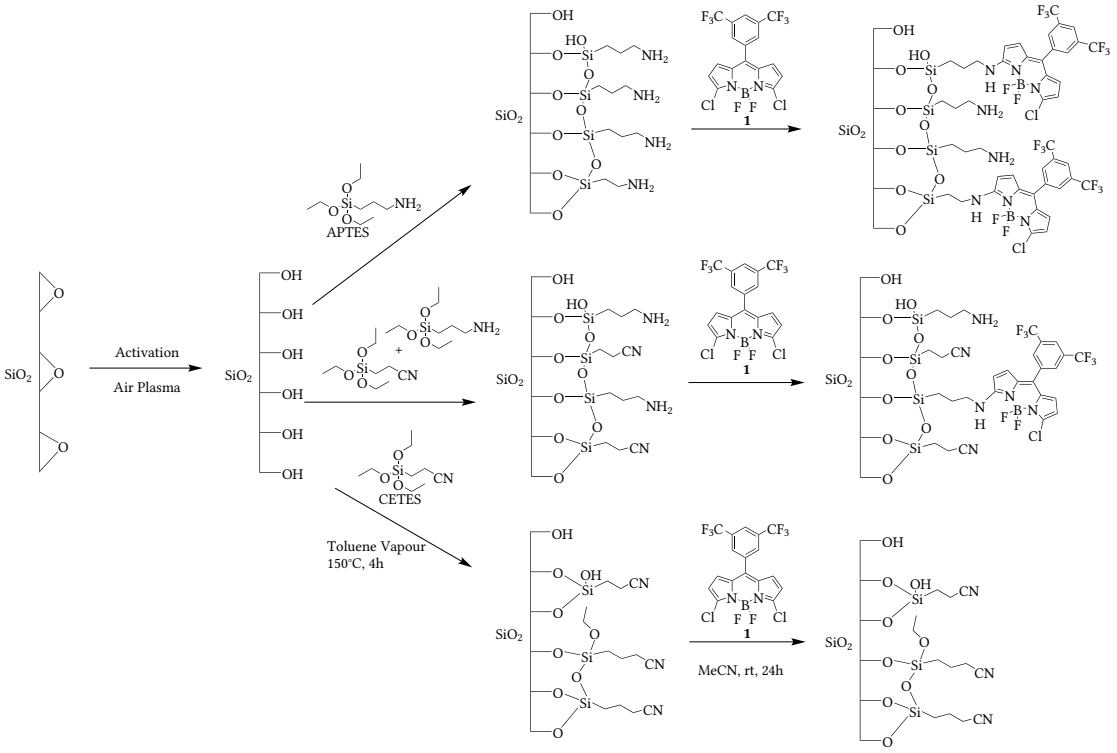

Scheme 2.5: Chemical structures of APTES, CETES and label **1** and scheme of surface reactions actions

To extend the approach of adjusting the functional surface group density through the use of a functional and an inert silane in a co-deposition process to industrially more relevant surfaces, the work returned to APTES with CETES as the inert component. Given the obtained experience in silane layer formation, a significant increase in the quality of the obtained layer is expected. The characterization of the resulting surfaces relies again on **1**, the results of which can be directly linked to traceable methods, as shown previously.[65]

In contrast to the well-defined monolayers of the APDIPES:CPDMMS system, the fluorescence intensity alone can be a misleading parameter when dye **1** is used with the multilayer-forming APTES:CETES system, as significant fluorescence quenching occurs at higher labelling ratios (see Sec. 2.1.4). Since the previous chapter has shown that **1** is capable of quantifiable functional group labelling, surmounting the drawbacks of fluorescence quenching is paramount in terms of the practical application of fluorescence labelling.

A known method to account for concentration-dependent fluorescence self-quenching is the application of fluorescence lifetime measurements.[191,192] Excited-state interaction of dye with the surface amino groups (like photoinduced electron transfer (PET)) is unlikely as no indication of such a process was found in the previous chapter.[65] The main processes leading to self-quenching of dyes attached to (solid) surfaces are dimer formation and homo-energy transfer.[84,193] In solution, collisional self-quenching needs to be taken into account as well, yet such interactions are not expected on solid surfaces since the dyes are covalently bound to the surface and therefore restricted in motion. Most factors diminishing the fluorescence intensity can be accounted for in a simple manner by relating the intensity in the presence (I_Q) and the absence (I_0) of quenching to the lifetime in the presence (τ_Q) and the absence (τ_0) of quenching.[192]

$$\frac{I_Q}{I_0} = \frac{\tau_Q}{\tau_0} \tag{2.7}$$

Here, I_Q and τ_Q are the fluorescence intensity and lifetime measured for the actual sample. τ_0 can be determined for the sample with the lowest content of dye. Although this might not necessarily be the "true" unquenched value of an unperturbed dye molecule in an ideally diluted state, the defined sample with the least amount of anchored dye can serve as a reasonable reference point. In general, for fluorophores bound to a surface, distributed lifetimes can be expected rather than strictly mono-exponential decays, simply because the microenvironment around each and every fluorophore cannot be considered as identical or homogeneous. A suitable way to analyse such data thus invokes the stretched exponential (or Kohlrausch) function.[191,194,195]

$$I(t) = A + B \cdot e^{\left(-\frac{t}{\tau}\right)^{\beta}} \tag{2.8}$$

Unfortunately, dimer formation cannot be determined using this method.[193] This equation is commonly used for approximating lifetime distributions on surfaces, as it rather conveniently provides a lifetime τ and factor β describing the distribution. For details on the distribution provided by β see ref. 195 and 196. Because possible single processes contributing to the non-exponential decay, such as dimer formation, homo-energy transfer or interaction with surface groups/adsorbed water, cannot be easily disentangled or specified for our present system, β needs to be variable rather than fixed to a particular model. A second dye, Rhodamine B isothiocyanate (RITC) will be applied to surface labelling, to verify the concept with an independent compound.

A second novel method is considered to be successfully applied given the achieved quality of the silane surfaces prepared with the optimized process, especially concerning the transparency of the slides. That is the quantitative determination of the dye content via UV/Vis spectrophotometry. In combination with the labelling ratio as determined by XPS, quantification of surface functional groups on amino slides should be possible.

The same procedure was used as described in section 2.5, only replacing APDIPES and CPDMMS with APTES and CETES. Based on the kinetic effects seen in that section the following ratios of APTES:CETES were used: 1:0, 1:1, 1:3, 1:7 and 0:1 (providing samples **CM**, **CO**, **CP**, **CQ** and **CR**, in the respective order)

2.6.1 Characterization of the silane surfaces

2.6.1.1 Contact Angle Measurement

The bare silane films were analysed by means of water contact angle measurements. θ_C was found to span from 73(1)° for the pure amino silane surface to 56(2)° for the pure cyano silane surface. In agreement with the previous work on monoalkoxysilane-derived model surfaces, the static contact angle θ_C decreases with reduced content of APTES in the deposited vapour. Accordingly, the ratio of the two silane components was calculated again using the Cassie equation for a simple two component model (Eq. 2.4).

Although the determined ratios (Table 2.14) show the expected trend of decreasing amino ratio, it may be doubted that Cassie's Law can be applied straightforwardly to those samples. One major requirement is that the two components mix without differences in structure or silane density compared to the pure surfaces.

2.6.1.2 X-ray photoelectron spectroscopy

The elemental compositions of the bare silane surfaces of **CM**-**CR** were determined with XPS to identify if the different silanes form layer of comparable density. Careful examination of the data obtained for the different silane layer shows that the surfaces containing (various amounts of) APTES exhibit a comparable content of nitrogen (4 to 5 at%), accompanied by a slight decrease in carbon content, whereas the pure CETES-derived surface shows a significantly lower carbon (~10 at% vs 20 to 25 at%) and nitrogen content (~2 at% vs 4 to 5 at%). This indicates that the layer thickness is significantly lower in the case of CETES. In combination with the higher relative contents measured for the substrate elements (Si and O), it is reason-

able to assume that the structure of the pure CETES layer deviates significantly from that of the APTES-containing layers, especially in terms of the substrate contribution to the measured contact angle, and Cassie's equation cannot be reliably employed. Only minor amounts of ca. 10 % of amino silane appear sufficient to catalyze condensation reactions yielding a thicker silane layer.[42,70,77,91,143,150,170]

It is also noteworthy that compared to the previous work on vapour deposition of APTES (ref. 88 and Sec. 2.1.4), the more rigid control of the atmosphere during the process yields thinner and more homogeneous aminosilane layer.

Table 2.14: Laboratory XPS compositional data of pure and mixed APTES:CETES samples (all in at%) and determined Cassie Ratio f_1

APTES (f_a)	C 1s	N 1s	O 1s	Si 2p	f_1
100 % (**CM**)	26.2	4.2	42.4	27.2	1.00(2)
50 % (**CO**)	24.3	5.1	42.4	28.2	0.45(2)
25 % (**CP**)	22.3	4.8	43.9	28.9	0.43(4)
12.5 % (**CQ**)	18.2	4.2	47.4	30.2	0.24(2)
0 % (**CR**)	9.5	1.7	56.1	32.7	0.00(3)

2.6.2 Characterization of surfaces labelled with 1

Table 2.15: Laboratory XPS compositional data (in at%) and fluorescence intensities, fluorescence lifetimes and β values of pure and mixed APTES:CETES samples after labelling with **1**

APTES (f_a)	C 1s	F1s	N 1s	O 1s	Si 2p	F / 10^4 a.u.	τ_F / ns	β
100 % (**CM1**)	27.3	1.3	4.1	41.9	25.4	17.4	0.34	0.52
50 % (**CO1**)	27.1	0.6	4.9	41.3	26.1	22.5	0.79	0.59
25 % (**CP1**)	21.5	0.3	4.0	46.0	28.1	24.4	1.19	0.64
12.5 % (**CQ1**)	19.5	0.2	3.8	46.8	29.6	22.2	1.70	0.69
0 % (**CR1**)	11.2	0.0	1.6	55.3	31.8	0.7	-	-

The samples were treated with the label dye **1** according to the commonly used procedure involving cleaning the surfaces with Soxhlet extraction to yield samples **CM1**, **CO1**, **CP1**, **CQ1** and **CR1**. The fluorescence intensities were recorded with the fluorescence scanner. Figure 2.32 reveals that the relative fluorescence intensity increases slightly from the lowest applied amino content (12.5 %) to 25 % followed by a decrease for 50 % and 100 %; the pure CETES slide does not show any significant emission. Since the XPS data of the silane layer without the dye (Table 2.14) do not suggest an increase in amino groups on the surface with a reduced fraction of

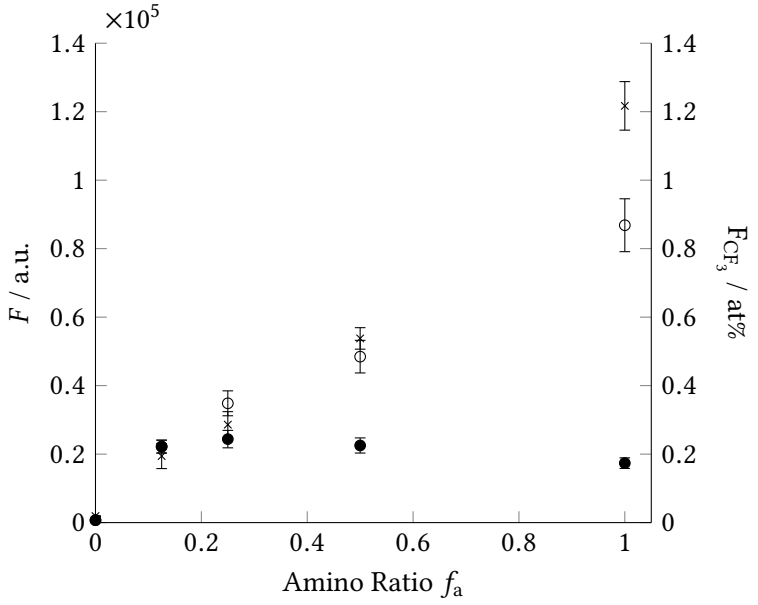

Figure 2.32: Relative contents of organic fluorine (×) and fluorescence intensities (without (●) and with (○) lifetime correction) for mixed silane substrates labelled with **1** (λ_{Ex} = 488 nm; λ_{Em} = 550 to 600 nm)

APTES in the vapour deposition process, the negative correlation can be ascribed to significant fluorescence quenching at higher dye concentrations, similar to the earlier finding (Sec. 2.1.4). To analyse the actual amount of bound dye, XPS spectra of the samples were measured and the content of organic fluorine was determined (Table 2.15). As shown in Figure 2.32, these contents correlate well with the applied APTES ratio. It appears as if, in contrast to the previous findings on APDIPES/CPDMMS, the silane ratio on the substrate follows the silane ratio used in the vapour deposition process. However, the amino/cyano ratios that showed the strongest deviation between the applied and the resulting ratio (0.4 to 6 % relative aminosilane content) in the prior work were not considered here. Additionally, none of the present surfaces can safely be considered mono-layer like, as even little amounts of water will lead to self-condensation of the tri-alkoxysilanes, especially in the presence of the catalysing amino group. The deviation between the XPS and fluorescence data clearly suggests that an increase in amino content entails enhanced fluorescence quenching.

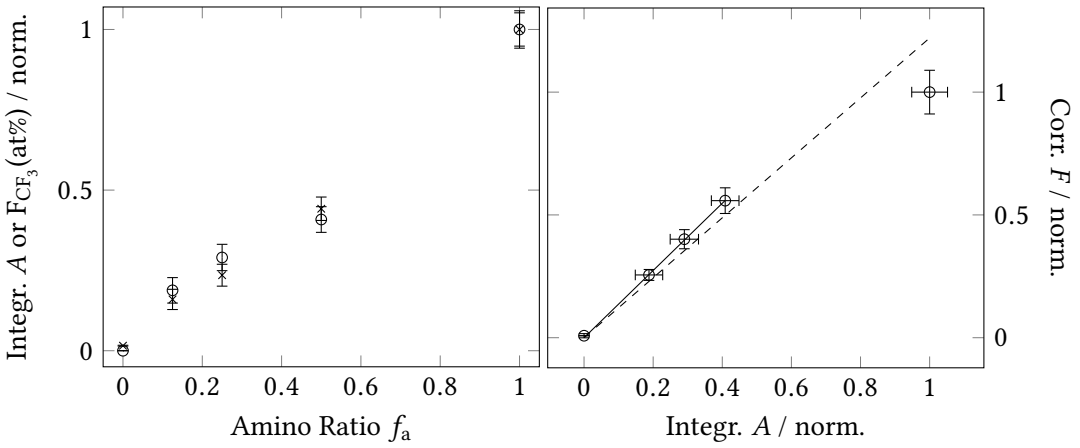

Figure 2.33: Comparison of relative dye contents determined from normalizing integrated absorption (○) and organic fluorine contents from XPS (×) (left) and correlation of lifetime corrected fluorescence intensity with integrated absorption (both normalized, linear fits with ($y = 1.2x$; $R^2 = 0.970$; - - -) and without ($y = 1.4x$; $R^2 = 0.999$; ——) considering the highest point, right) for samples **CM1-CR1**

Figure 2.32 compares the measured fluorescence intensity and the lifetime-corrected intensity with the applied amino ratio and the relative content of organic fluorine. It is obvious that the relative signal increase for the region of lower amino ratio shows a good overlap between the corrected fluorescence intensity and the XPS content. Only in the 100 % APTES case, for which τ is significantly reduced by a factor of five, the correction is insufficient (Table 2.15). A tentative explanation for the insufficient correction includes the appearance of (non-fluorescent) dimer formation at such high labelling densities that leads to a reduction of the overall fluorescence intensity without affecting the fluorescence lifetime.

To allow for an unambiguous interpretation of the results, another optical method is required to link the contents of fluorine to the emission behaviour of the fluorophoric system. That is why the possible use of conventional absorption spectroscopy was carefully examined.

As Figure 2.34 shows, especially at higher labelling densities, the spectra can be readily measured with acceptable signal-to-noise ratio. It is noteworthy that in contrast to the commonly used UV-absorbing label nitrobenzaldehyde, label **1** shows absorption in the visible range, where the transparency of the glass and the silane film is considerably higher and the measurement therefore less distorted. Especially below 300 nm, already thin silane films shows a pronounced absorption and tend to hamper or cut off such measurements. Advantageous for this method is also the fact that the preparation procedure covers both sides of the slide with a silane film so that the subsequent labelling reaction also leads to substrates that are equally functionalized with dye on both sides. In contrast to tightly focused fluorescence scanning

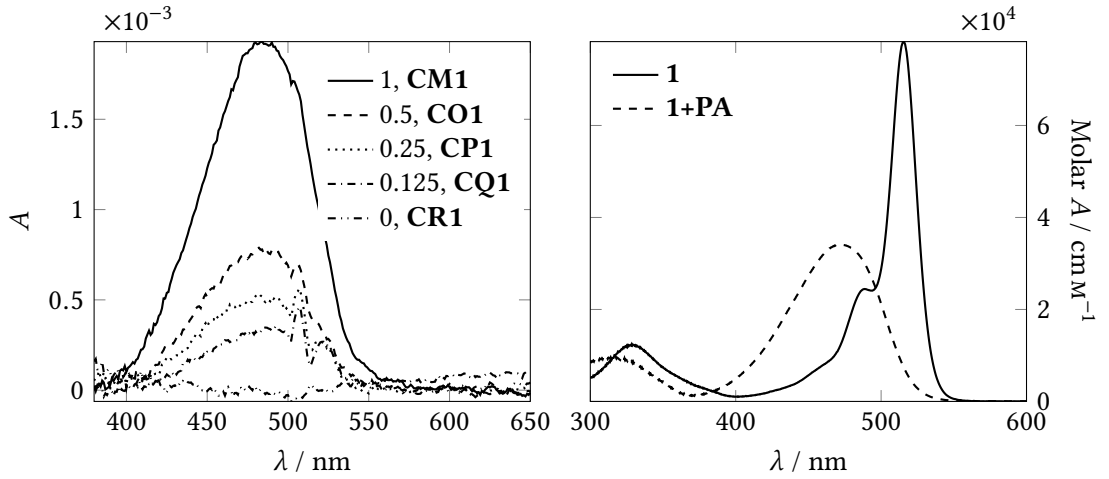

Figure 2.34: Absorption spectra of slides labelled with **1**, f_a given in legend (an instrumental artefact can be seen at ~510 nm, left) and molar absorption spectra of label **1** (——) and label **1PA** (- - -) in MeCN (**1**+ 10 equ. Pentylamine, reaction time ~10 min, right)

analysis, the absorbances measured thus contain contributions from twice the amount of dye. To compare the contents determined by XPS and absorption spectroscopy, the F(CF_3) at% and integrated absorption, respectively, were normalized to the highest (100 % amino) value and plotted in Figure 2.33. It can be seen that both datasets show the same correlation with the applied amino content.

Comparison of the UV/Vis absorption with the lifetime-corrected fluorescence data shows a similar trend as seen in the comparison of XPS and corrected fluorescence: a good correlation for the mixed silane surfaces, yet a clear deviation for the pure APTES-derived surface with the corrected fluorescence intensity being lower than expected (Figure 2.33).

In addition to the good correlation of XPS and absorbance data, it is also interesting to recall that absorption spectroscopy is a rather reliable technique for absolute measurements. To quantify the dye density applying the Beer-Lambert law, the absorption coefficient ε of the dye after the labelling reaction was determined by dissolving label **1** (which ε is known)[88] in acetonitrile and quantitatively transferring it to the mono-amino substituted dye by adding 10 equ. Pentylamine (**PA**) following this reaction: **1** + **PA** ⟶ **1PA** With $\varepsilon_{\mathbf{1},\lambda(\max)}$ (absorption coefficient of label **1** at its respective absorption maximum (λ(max) = 515 nm) known we can calculate the initial concentration of label **1** ($c_{\mathbf{1}}$).

$$c_{\mathbf{1}} = \frac{A_{\mathbf{1},\lambda(\max)}}{\varepsilon_{\mathbf{1},\lambda(\max)} \cdot d} \tag{2.9}$$

Given the quantitative transfer of dye **1** to the mono-amino substituted form (**1PA**) upon addition of Pentylamine we can assume:

$$c_{\mathbf{1}}(\text{before reaction}) = c_{\mathbf{1PA}}(\text{after reaction})$$

With $c_{\mathbf{1PA}}$ known we can know calculate the absorption coefficient for **1PA** at its according absorption maximum ($\varepsilon_{\mathbf{1PA},\lambda(\max)}$, with $\lambda(\max) = 472\,\text{nm}$):

$$\varepsilon_{\mathbf{1PA},\lambda(\max)} = \frac{A_{\mathbf{1PA},\lambda(\max)}}{c_{\mathbf{1PA}} \cdot d} \tag{2.10}$$

Figure 2.34 shows the molar absorption spectra of **1** and **1PA**.

The oscillator strength f (Equation 2.11) was calculated from the molar absorption coefficient to achieve a solvent independent value.[197]

$$f = \frac{mc_0^2 \ln 10}{N_a \pi e^2 n} \int \varepsilon(\tilde{\nu}) d\tilde{\nu} \tag{2.11}$$

The absorption coefficient of reacted label **1** on the slides was then calculated by assuming a solvation in air ($n = 1$). The fact that this is not necessarily true and a certain amount of water contributes to salvation was accounted for as an additional factor in the uncertainty of the derived absorption coefficient. The dye density on the surface in molecules cm^{-2} can be determined by transforming the Beer-Lambert law:[141]

$$A = \varepsilon \cdot c \cdot d \tag{2.12}$$

With c in $\text{mol}\,\text{l}^{-1}$ and d in cm. In the case of molecules on surfaces, the molecules can be considered being contained in an infinitesimal layer and not in a volume. Instead of having a certain mount amount of dye distributed at certain spatial concentration (c) along a certain length of the beam (d), this amount (n in mol) is confined on a certain surface area (S in cm^2). Since the amount of dye is the same irrespective of being distributed in a volume or confined to a surface we can replace $c \cdot d$:

$$c \cdot 10^{-3} \cdot d = \frac{n}{S} \tag{2.13}$$

The commonly used areal density of molecules (N) on the surface area (S) can be calculated from the absorption by combining 2.12 and 2.13 and converting n to N by multiplication with the Avogadro constant (N_A):

$$\frac{A}{\varepsilon} \cdot N_A \cdot 10^{-3} = \frac{N}{S} \tag{2.14}$$

As the dye does not show a quantitative reaction with the surface amino groups, this number cannot be equivalent to the density of surface amino groups. However, the nitrogen-to-fluorine ratio from the XPS measurements of the labelled 100 % APTES surface allows the determination of the labelling ratio, as nitrogen as well as fluorine are unique to the organic entities of the surface layer and only negligibly present in glass. This in turn provides access to the absolute functional group density. The values thus derived are given in Table 2.16. It has to be pointed out that the uncertainties are uncertainties of measurement and do not include any possible systematic errors. Given the prior experience in repetitive determination of labelling density on different instrumentation it is assumed that the error of that value is around 25 %.[65] Albeit this appears quite high, it is actually precise compared to most other labelling based quantification techniques that assume a complete labelling. This assumption would for example lead to an underestimation of a factor of 10 to 20 in the current case. The deviation resulting fluorescence quenching can additionally account to a factor of more than 5 which would finally result in an error of nearly two orders of magnitude if only steady-state fluorescence intensity is considered. The data in Table 2.16 further reveal that the functional group density determined in the previous (~2 functional groups cm^{-2}) is very similar for most of the present samples and only exceeded by the pure APTES surface (~4 functional groups cm^{-2}). Since, in contrast to the mono-alkoxysilane-derived surfaces in ref. 65, notable fluorescence quenching is encountered on the present surfaces functionalized with tri-alkoxysilanes and even dimer formation of dye molecules seems to play a role for the highly dense samples, nanometric scale a clustering of APTES on the surfaces seems to occur. The latter however could not be resolved with the available analytical methods.

Table 2.16: Functional group and label densities for the investigated surfaces, given errors are only experimental

APTES (f_a)	dyes $\cdot 10^{12} cm^{-2}$	functional groups $\cdot 10^{14} cm^{-2}$
100 %	23(2)	4.1(3)
50 %	9(1)	1.7(2)
25 %	7(1)	1.2(1)
12.5 %	4(1)	0.8(1)
0 %	0.0	0.0

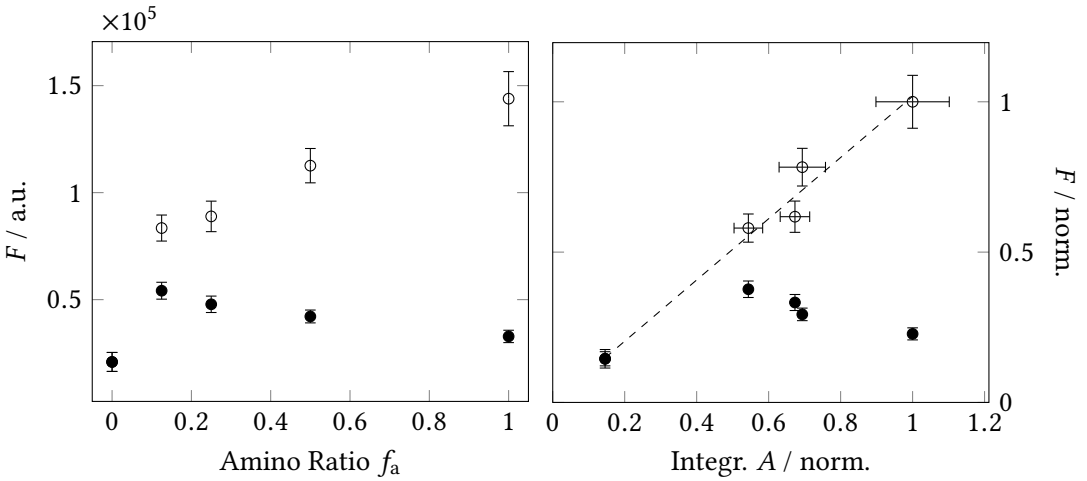

Figure 2.35: Correlation of lifetime corrected (○) and uncorrected fluorescence intensity (●)) with applied amino ratio (f_a, left) and with integrated absorption for RITC (both normalized, linear fit: $y = 1.02x$; $R^2 = 0.993$, right)

2.6.3 Characterization of surfaces labelled with RITC

Based upon the knowledge gained on the determination of surface functional group densities with the net uncharged and comparatively lipophilic dual-mode label dye **1** and XPS, fluorescence and absorption measurements, the suitability of different, commercial and broadly popular label dyes is investigated. Because such dyes are mainly used in the context of (bio)chemical applications in aqueous environment, many of them are charged to render them water-soluble. Accordingly, the choice was made to use the cationic dye Rhodamine B isothiocyanate (RITC) carrying a reactive group that targets amino-expressing surfaces. The major advantage of RITC in comparison with **1** is its applicability in buffered aqueous solution for cases in which substrates might be sensitive to organic solvents.[78,179] Additionally, its fluorescence intensity is widely insensitive to the environmental pH, in contrast for instance to fluorescein-derived labels such as Fluram or FITC. The latter is important for the aspired application since the microenvironmental pH of functional silane mono- or multilayers, and its local fluctuations, on solid supports is generally not known and difficult to determine. To ensure comparability between the two dyes, each slide was split in halves and one half each subjected to label **1** (vide supra, Samples **CM1**-**CR1**) each other half labelled in an adapted procedure applying

RITC in phosphate buffer for 4 h followed by thorough cleaning with acetone (Samples **CNR**, **COR**, **CPR**, **CQR** and **CRR**). Characterization then proceeded in analogy to the procedure described above for label **1**. XPS analysis was not endeavoured as RITC does not contain a unique XPS-sensitive element such as fluorine and the method would thus only provide little insight as compared to layers labelled with **1**.[80]

Figure 2.35 depicts the trends in fluorescence (as measured and after lifetime correction). The lifetime was determined using the stretched exponential function (Eq. 2.8). The lifetime-corrected fluorescence intensity correlates well with the integrated absorbances of the lowest-energy transition of RITC (Figure 2.35). Despite the fact that the lifetime correction seems to work well over the entire concentration range when compared to absorption, the actual amino group ratios deposited during the preparation process are only qualitatively reproduced (Figure 2.35). Tentatively, a certain amount of non-covalently bound RITC produces an offset that is difficult to correct. This is supported by the high fluorescence signal of the virtually amino-free surface derived from pure CETES. The effect of more rigorous washing conditions like prolonged exposure to buffer solution and Soxhlet extraction with ethanol was that under those conditions not only the electrostatically bound RITC was removed but also the silane film itself was altered, most likely by hydrolysis.[91,135] The applicability of dyes such as RITC thus seems to be limited for reliable quantification of surface amino groups on glass.

2.6.4 Conclusion

This section showed that a multi-mode surface functional group label such as **1** can also be used to quantitatively characterize multi-layer-like, highly dense functional silane surfaces. Although a simple fluorescence intensity-based read-out is not possible for such systems, the deviations from linearity can be corrected to a certain extent through fluorescence lifetime measurements. On the other hand, XPS and absorption spectroscopy provide reliable data for higher surface functional group densities and are not sensitive to changes in the nanostructure of the sample. A combination of XPS and spectrophotometry allows the determination of the functional group density with a comparatively high precision for a simple laboratory method. Stepping on from the BODIPY-type labelling dye to a commercial Rhodamine B derivative, the fluorescence lifetime correction was shown to be highly efficient, yet presumably due to the charged nature of the dye, a significant amount of unspecific signal hampers reliable quantification.

2.7 Comparison of substrates

The promising application of the developed silanization process and quantification methods towards a reference system for functionalized surfaces challenges the suitability of the applied substrate, namely standard soda-lime glass obtained from Corning. Different substrates, mainly for microarray application, were obtained and compared to the Standard Corning glass. The used substrates were Ultraclean slides from Thermo Fisher, Glass B from Nexterion and fusion-drawn slides from Corning. Apart from Glass B, which is a boro-silicate glass, all slides consist of soda-lime glass. In contrast to the standard Corning slides, the special Corning slides are prepared with a Fusion-Draw process and subjected to surface hardening that supposedly results in smoother surface. Nexterion glass B is prepared via a float process and also assumed to be smoother. Apart from the bare glasses, the APDIPES and CPDMMS functionalized versions were investigated.

2.7.1 Bare substrates

The main differences between the different substrates are expected in the surface quality and the transparency. Accordingly, the substrate were first investigated by AFM and spectrophotometry.

2.7.1.1 AFM

The bare substrate samples were investigated by AFM, Figure 2.36 shows exemplary images for each substrate, with the average roughness calculated from ten individual scans at different magnifications. The Corning Fusion-Draw glass is the smoothest, both in the absolute roughness as well as in deviation from the average (Fig. 2.36b). Comparing the Corning Standard with the Thermo Fisher Ultraclean (Fig. 2.36a and 2.36d) shows that both have a comparable average roughness, however, Thermo Fisher Ultraclean comprises a higher deviation, which is due to the presence of a significant number of irregular defects. Corning standard yet showed a number of small scratches, that probably result from the tight packing of the slides. The Nexterion B glass shows the most interesting features. The majority of the surface shows a comparably low roughness, however, deep round holes of irregular size and distribution break that impression. They probably result from the float process fabrication and stem from air bubbles trapped between the liquid glass and the float bed (liquid tin).

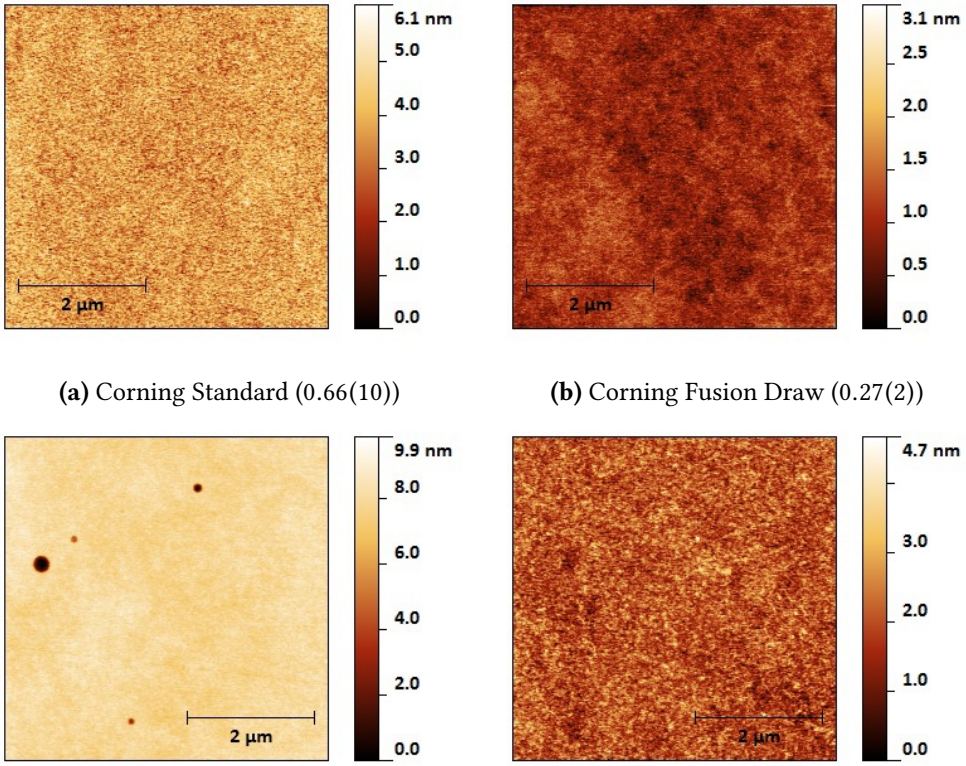

(a) Corning Standard (0.66(10))

(b) Corning Fusion Draw (0.27(2))

(c) Nexterion B (0.41(14))

(d) Thermo Fischer Ultraclean (0.59(41))

Figure 2.36: AFM images of different substrates, RMS roughness (in nm) given in brackets

From these results it is concluded, that the differences in surface quality are only marginal. As expected, Corning Fusion Draw glass is of superior smoothness, whereas Corning Standard does not show significant irregularities. Thermo Fisher and Nexterion B, both being substantially more expensive than Corning Standard, do not convince on the microscopic scale as both show a number of defects.

2.7.1.2 Spectrophotometry

The quality of a glass is usually also characterized by its transparency, especially if optical absorption measurements of surface species are endeavoured. Figure 2.37 shows the absorption spectra of the substrates, including a quartz slide for comparison. It can be seen that the soda-lime substrates show the highest absorption, which increases most rapidly below ~300 nm, only the Corning Fusion Drawn glass increases less. In the relevant range around 500 nm, all soda-lime glasses look remarkably similar. The Borofloat glass Nexterion B obviously provides

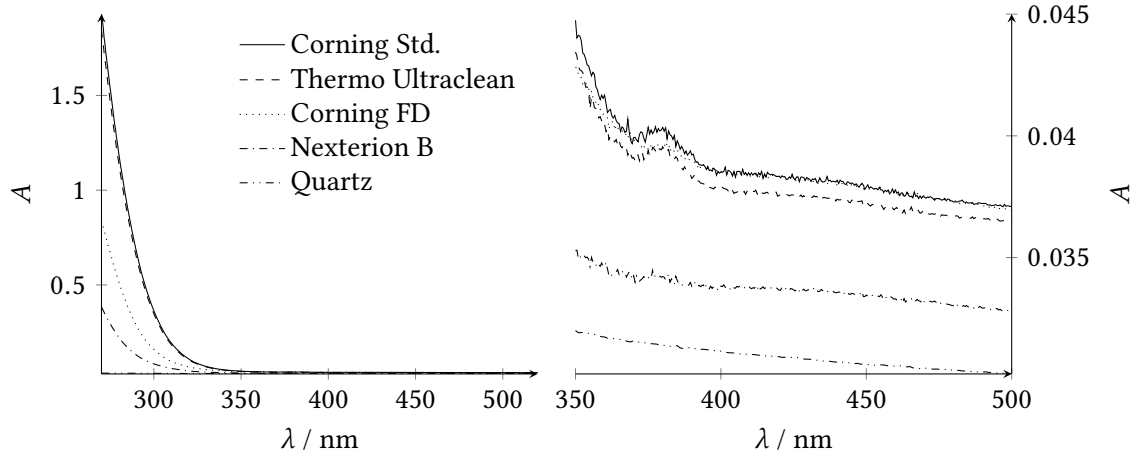

Figure 2.37: Comparison of Absorption Spectra of different microscope slide glasses

a higher transparency across the given range. The quartz slide, however, shows impeccable performance in the UV/Vis absorption measurements with an optical density <0.05 throughout the whole measured range (190 to 1100 nm). Unfortunately, quartz is unsuitable for XPS measurements and can not be used as a reference substrate. For the visible light range, which is currently the most relevant, all glasses appear suitable, as the differences are minor. The advantage of Nexterion B and even more of quartz glass is not only the lower overall absorption, but also the featurelessness of the absorption bands that simplifies background correction significantly.

2.7.1.3 XPS measurements

Table 2.17: Elemental composition of relevant elements (all in at%) recorded with XPS prior and after Ar ion cluster sputtering

	Sample	C 1s	Ca 2p	F 1s	Mg 2s	N 1s	Na 1s	O 1s	Si 2p
Cleaned	Cor. Std.	27.7	2.0	0.1	1.0	1.1	1.6	49.5	16.9
	Cor. FD	15.3	0.8	0.0	1.1	0.1	2.7	60.9	18.4
	Nex. B	15.3	0.3	0.0	0.2	0.4	0.6	61.8	21.5
	Th. Fisher	14.6	1.3	0.0	0.9	0.6	2.2	59.6	20.9
Sputtered	Cor. Std.	3.2	2.4	0.0	1.4	0.2	2.4	67.3	23.1
	Cor. FD	0.7	0.8	0.0	1.3	0.1	5.0	70.9	21.3
	Nex. B	2.6	0.4	0.0	0.2	0.3	1.1	70.91	24.6
	Th. Fisher	1.0	1.8	0.0	1.2	0.4	2.5	68.9	24.1

The penetration depth of XPS measurements is usually around 10 nm. The silane films commonly encountered in this work, however, are around 1 nm. This means that a significant part of the measured signals stems from the substrate rather than the silane layer and knowledge of the constitution of the substrate is crucial in understanding the results of silanized samples. Yet, the different surface energies of freshly cleaned and silanized glass lead to strong differences in the (immediately) formed carbonaceous overlayer of atmospheric carbon compounds deposited on the surface. Even extensive cleaning does not produce a surface completely free of carbon contaminations, if the surface is exposed to ambient atmosphere prior to the measurement.[198] A conceivable solution to measure a sample without adsorbed contamination requires cleaning of the sample in the XPS instrument. This can be done with an Ar cluster ion beam, which would gently remove the overlayer without significantly damaging the substrate. Fortunately, an XPS instrument equipped with an Ar cluster gun was available at NPL. The four different substrates were pre-cleaned by rinsing with IPA prior to transfer into the instrument. A survey scan was performed prior to and after sputtering. The samples were bombarded with ion clusters until the C 1s signal remained stable. A second survey scan was performed after complete sputtering. The results from both scans are summarized in Table 2.17. The most relevant elements for the analysis of labelled surface species are carbon, nitrogen and fluorine. The lowest residual carbon is found Corning Fusion Draw glass and a little more in Thermo Fisher Ultraclean. Nexterion B and Corning Standard contain significantly higher amounts of carbon. However, carbon is currently not involved in quantitative analysis and minor changes can be accounted for. More important is reduction to less than 10 % of the original content that points to the necessity of careful sample handling. Considering the nitrogen contents, a notable reduction is only seen for Corning Standard glass which in this measurement also comprises the highest initial carbon content. The same is found for fluorine which is only originally present on the Corning Standard glass and absent in all cases after sputtering. The higher contents of contamination are probably only experimental since the Corning Standard glass was measured first and the remaining glasses were accordingly longer subjected to the ultra-high vacuum. The residual nitrogen contents of the glasses are all very comparable and low enough to not provide a critical influence on the analysis. The alkali and alkaline-earth ion contents show changes for the different substrates to verify that they indeed compose of different glasses.

Table 2.18: Contact angles of investigated substrates (Corning Standard (Cor. Std.), Corning Fusion-Draw (Cor. FD), Nexterion B (Nex. B) and Thermo Fisher Ultraclean (Th.Fisher)) treated with APDIPES or CPDMMS and fluorescence intensity (F) after labelling with **1** (λ_{Ex} = 488 nm; λ_{Em} = 550 to 600 nm)

	Sample	θ_C/ °	θ_{adv} / °	θ_{rec} / °	θ_{hys} / °	F / a.u.
APDIPES	Cor. Std.	81.8(15)	87(1)	66(2)	21	53 700(1424)
	Cor. FD	86.6(15)	90(1)	72(1)	18	43 675(1843)
	Nex. B	78.5(8)	91(1)	62(1)	29	50 912(1393)
	Th.Fisher	80.8(9)	91(2)	65(1)	27	58 859(2468)
CPDMMS	Cor. Std.	68.7(13)	73(1)	55(1)	18	95(10)
	Cor. FD	68.7(20)	71(1)	51(2)	21	128(12)
	Nex. B	70.1(9)	74(1)	53(1)	20	807(67)
	Th.Fisher	71.7(15)	74(1)	55(1)	18	83(13)

2.7.2 Silane treated samples

The different substrates were treated with APDIPES and CPDMMS following the optimized vapour deposition process. The characterization followed the common procedure applying contact angle measurements and fluorescence labelling with **1**. The results are listed in Table 2.18.

2.7.2.1 Contact Angle Measurements

The contact angle measurements only show pronounced differences, especially in θ_{hys}, for the amino-silane treated samples, whereas the values for CPDMMS mostly compare. It is reasonable to assume that the amino-silane, given its more complicated binding mechanism, lacks a certain reproducibility in layer formation. For CPDMMS, only the Corning Fusion Draw shows slightly reduced dynamic contact angles, with an insignifcantly higher contact angle hysteresis. Yet this glass shows consistently higher errors in θ_C for both silanes. Nexterion B on the other hand shows consistently low errors of <1°. However, θ_{hys} for the APDIPES samples is lowest for both Corning glasses.

2.7.2.2 Fluorescence Analysis

The different silanes on the four substrates were also treated with **1**. For the amino silanes, the most notable differences are the lower relative errors of APDIPES on Corning Standard and Nexterion B. Thermo Fisher shows the highest fluroescence intensity, followed closely by Corning Standard and Nexterion B. Only the Corning Fusion Draw shows a significantly lower intensity with a high relative error. This substantiates the assumption that the Corning Fusion Draw glass does not show the same silanization. The fluorescence intensity of the CPDMMS treated samples after exposure to **1** and careful cleaning shows only a significantly higher background fluorescence for Nexterion B. This finding, however, is consistent with other measurements and presents a significant drawback of this glass.

2.7.3 Conclusion

The comprehensive analysis of various important parameters of glass composition, structure and silane layer formation provided valuable insight on the influence of the glass on the experiment. These findings show that the substrate is only of little influence on the formed layer and there is no immediate need to change the applied substrate, which is economically much more favoured. Only the tight packaging results in a scratched surface that can affect higher magnification measurements, including fluorescence microscopy. From the surface structure and the elemental composition, the Corning Fusion Draw glass is most favourable. This glass was provided by Corning on special request for a highest quality soda-lime glass of high reproducibility and is currently not commercially available. However, the positive results are not fully reflected after vapour deposition which indicate a less favourable layer formation on the Corning Fusion Draw glass. Further experiments have to be done to conclusively identify the potential of Corning Fusion Draw glass as substrate for surface functional group density reference systems.

2.8 Application of platform dyes

The application of dye **1** has provided valuable insight in the properties of silan-based functionalized surfaces. The methodology used to analyse such fluorescently labelled surface was expanded by numerous methods, including UV/Vis absorption and fluorescence lifetime analysis. The validation of the obtained results could satisfyingly be achieved via XPS based on the dual-mode properties of **1**. However, **1** is limited in the addressed analyte, namely amino groups, the environmental limits of application, namely being inapplicable in aqueous environments, and the spectral range it can be addressed with. To expand this approach without being required to perform a complete characterization for every single dye and addressed functional

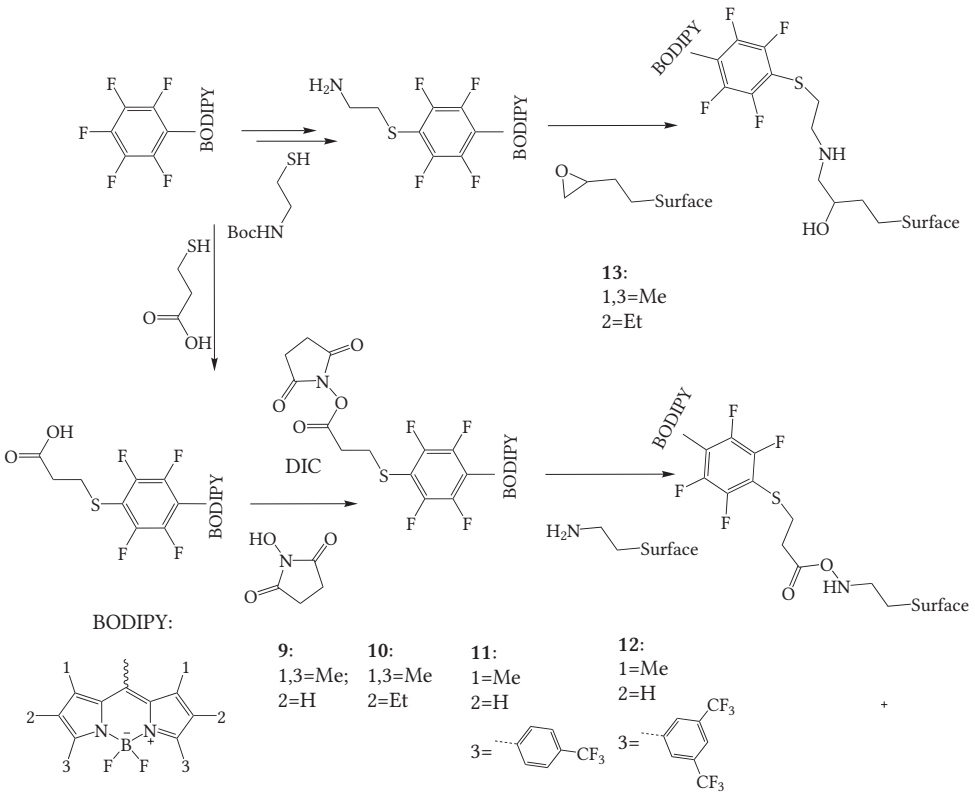

Scheme 2.6: Example derivatization reactions to transfer the pentafluorophenyl dyes **2**-**5** into label dyes (for epoxy (top) or amino groups (bottom) and structures of prepared compounds **9**-**13**

group, the dye platform based on the pentafluorophenyl moiety was developed. This fragment can easily be incorporated at the meso position of a BODIPY dye without putting restrictions on the remaining dye structure. Accordingly, a significant spectral range can be covered with differently substituted BODIPY systems, as shown with **2**, **3**, **4**, **5**, **6** and **7** in section 2.1.1. These dyes span a range of 300 to 800 nm in excitation and emission, from the blue spectral region to the deep red.

As shown with **4** and **5**, the fluorine content of the dye can be increased to at least 28 % by concise manufacturing of highly fluorinated pyrrole precursors. The pentafluorophenyl residue introduces organic fluorine for XPS quantification into the molecule and serve as a versatile derivatization unit following simple substitution chemistry at the same time. Although the direct application of the pentafluorophenyl substituted dyes as amino labels was unsuccessful due to the insufficient reactivity of the pentafluorophenyl unit towards surface amino

groups, several substitutions with thiol-based linker systems are possible to prepare selective surface functional group labels. As the majority of application that require a quantitative characterization of the target surface functional groups are based on bio-chemical experiments, involving for example proteines or DNA, it is beneficial if the chemistry of the labelling process is comparable.

2.8.1 Amino reactive dyes

Among the most common chemical methods in surface binding of amino groups is the *N*-hydroxysuccinimide (NHS) ester based chemistry.[199] Here, a carboxyl group is transferred into its reactive NHS ester by activation with a carbodiimid reagent. Subsequently, the NHS is cleaved by an amino group of the target molecule or surface under formation of an amide bond. To follow that chemistry, a carboxylic acid needs to be included into the label dye to render it an active labelling component. Accordingly, **2**, **3**, **4** and **5** were treated with mercaptopropionic acid in DMF under addition of K_2CO_3 to yield compounds **9**, **10**, **11** and **12** (see Scheme 2.6 for a comprehensive overview of the involved chemistry).

Table 2.19: XPS compositional data of mixed silane **CS-CW** samples labelled with **11** and **12**, including f_x ratio determined from F/N ratio

Sample	f_a	XPS contents / in at%						f_x	F /	τ_F /	β
		C 1s	F 1s	N 1s	O 1s	Si 2p	F 1s (CF_x)		10^4 a.u	ns	
CS11	1.0	18.1	2.7	1.6	55.2	22.3	2.3	1.00	1.43	0.73	0.69
CT11	0.5	18.6	1.2	1.7	55.9	22.7	1.1	0.23	4.22	2.77	0.96
CU11	0.25	16.3	0.8	1.8	57.8	23.3	0.6	0.11	3.18	3.81	1.00
CV11	0.125	16.5	0.5	1.6	57.8	23.7	0.4	0.08	3.48	4.87	1.00
CW11	0.0	12.4	0.3	1.4	61.6	24.2	0.2	0.04	0.48	-	-
CS12	1.0	14.6	1.2	1.1	51.8	31.3	1.2	1.00	0.71	0.64	0.69
CT12	0.5	16.3	0.7	1.5	50.8	30.6	0.7	0.38	2.38	3.58	0.96
CU12	0.25	14.8	0.5	1.5	51.6	31.7	0.5	0.27	2.41	4.29	0.94
CV12	0.125	13.4	0.3	1.8	52.8	31.7	0.3	0.14	1.68	5.21	1.00
CW12	0.0	11.7	0.2	1.3	55.0	31.8	0.2	0.10	0.08	-	-

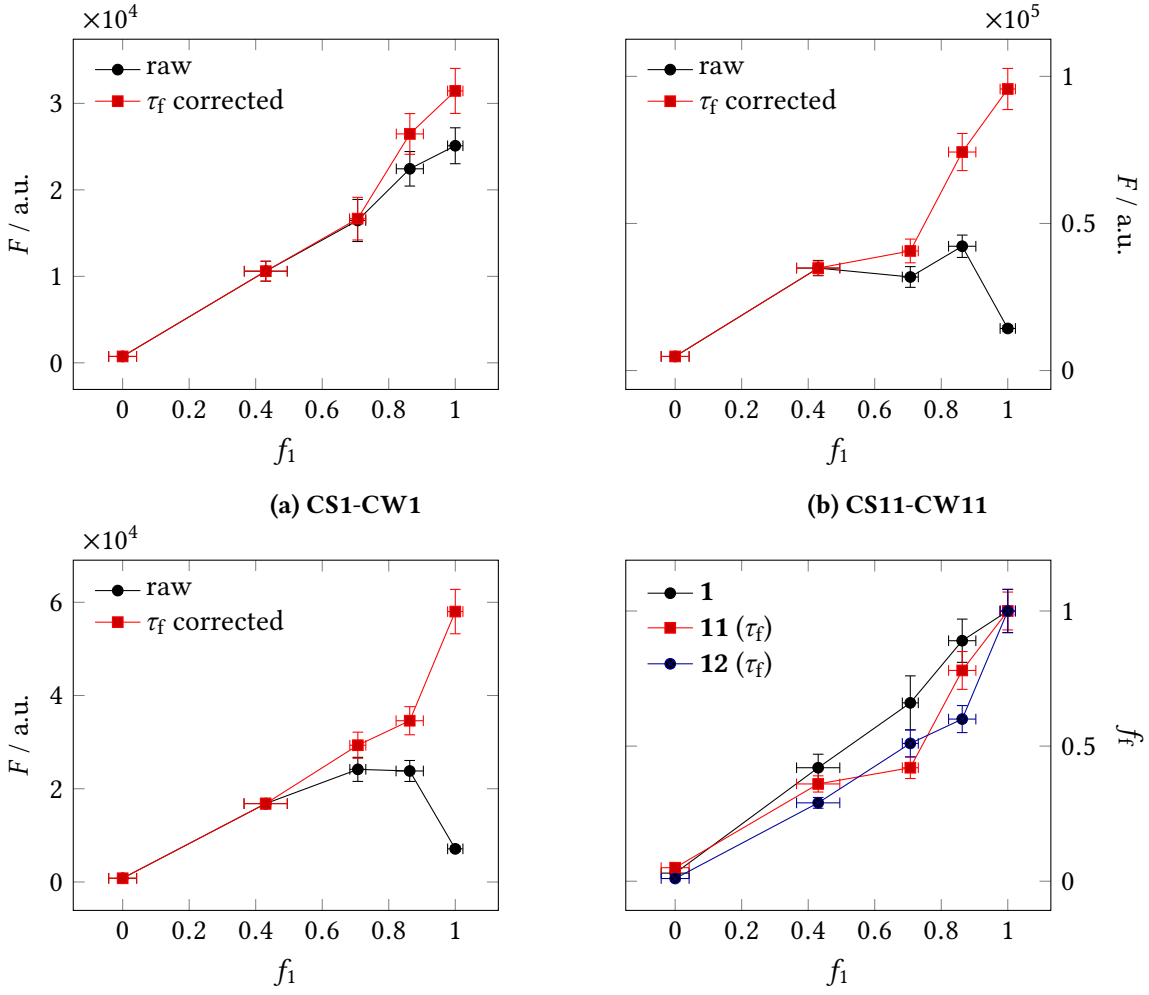

Figure 2.38: Comparison of uncorrected (raw) fluorescence intensities and lifetime corrected values for samples labelled with **1** (a), **11** (b) and **12** (c) and comparison of different functional group ratios determined through the corrected fluorescence intensity (2.38d)

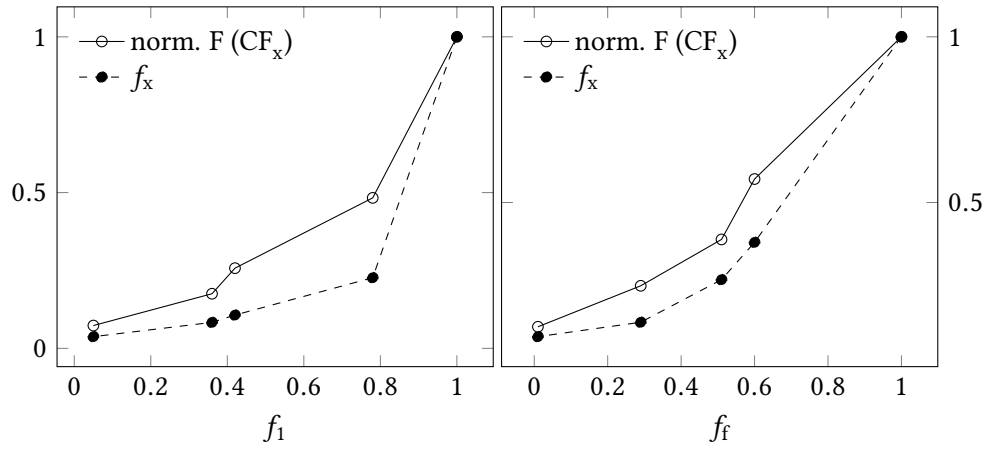

Figure 2.39: Comparison of f_x and normalized organic fluorine contents with relative corrected fluorescence intensity (f_f) for **CS11-CW11** (left) and **CS12-CW12** (right)

9 was used to optimize the coupling procedure in solution using different coupling reagents and active esters and 1-pentylamine as a model amine. *N,N'*-diisopropylcarbodiimide (DIC) and NHS in MeCN were found to be the most efficient pair to achieve a fast and complete amide formation. The dyes **10**, **11** and **12** were applied to sample surfaces obtained from mixed APDIPES:CPDMMS preparation, comparable to 2.5. The applied amino ratios f_a were 1, 0.5, 0.25, 0.125 and 0, the unlabelled surfaces were satisfyingly characterized by contact angle measurement to obtain the Cassie ratio (f_1). **1** was also applied following the usual procedure as a comparison.

The dye labelled surfaces were investigated via microarray scanning. The recorded fluorescence intensities are shown in Fig. 2.38. It can be seen that the fluorescence intensities obtained from **1** labelled surfaces increases linearly with the amino content, as previously shown (see Sec. 2.5). The fluorescence intensities of **CS11-CW11** and **CS12-CW12** show an initial increase, followed by a decreasing intensity for the higher functional group densities. There is a pronounced difference between the fluorescence intensities obtained from **11** and **12**, although the solution data of the dyes indicated a similar fluorescence behaviour (see Sec. 2.1.1).

CS10-CW10 show only a very weak fluorescence intensity and are not shown. The reason for this can only be speculated, especially since prior experiments (not included) showed normal binding for **10**. A likely explanation is an impurity in the compound, namely the starting material mercaptoproprionic acid, that is competing with the label dye for the surface functional groups. The samples **CS1-CW1**, **CS11-CW11** and **CS12-CW12** were additionally investigated by fluorescence lifetime measurements to calculate the corrected fluorescence intensities similar to the procedure shown in section 2.6.2).

Figure 2.38 compares the uncorrected and the corrected fluorescence intensities. It can be seen that in agreement with prior findings, the lifetime correction is not necessary for **1** on mono-alkoxy silane derived surfaces, as no significant changes in the fluorescence lifetime occur. Contrary is the situation encountered for **11** and **12**. In both cases, the fluorescence lifetime correction significantly enhances the correlation between f_f and f_1. It can be concluded that **11** and **12** show a significantly higher quenching effect than **1** upon surface labelling. Independently obtained results point to similar quenching for **9** and **10**. The possibilities in terms of an application of these dyes are severely limited by this enhanced quenching, as prior findings indicated that the fluorescence lifetime based correction also has limited dynamic range and cannot account for intense quenching. These experiments were performed prior to the introduction of the UV/Vis absorption (see Sec. 2.6) for dye quantification and no such analysis was performed.

To evaluate the dual-mode labelling properties, the samples **CS11-CW11** and **CS12-CW12** were additionally analysed by means of XPS survey scanning. Table 2.19 lists the relative contents of the important elements. Both dyes show comparatively high contents of organic fluorine. Surprisingly, **11** shows a two times higher amount than **12** (2.7 at% vs 1.2 at%), despite containing significantly less fluorine. Accordingly, the calculated labelling density of **CS11** amounts to 20 %, compared to only 7 % for **CS12**. This again indicates that the binding of the two different dyes is not as comparable as predicted. In contrast to the prior samples containing **1**, the other elements relevant two the surface layer, namely carbon and nitrogen, do not show the expected obvious trend, with decreasing carbon contents as the content of dye and APDIPES reduces, accompanied by a relatively stable nitrogen content. On the contrary, the carbon content is lower for the 100 % APDIPES sample than for the one prepared with 50 % APDIPES, as is the nitrogen content, which is rather fluctuating between the different samples. A closer examination of the fluorine contents reveals that in both cases the dye-labelled pure APDIPES sample shows an exceptionally high amount of fluorine, compared to the first mixed sample. Accordingly, the resulting amino group ratio determined via the F/N ratio (f_x) through the adopted equation 2.6 is lower than expected for the mixed samples. Comparing f_x with f_f (see Fig. 2.39) shows that f_x may follow the same trend as the τ_f-corrected fluorescence intensity, yet does not correlate very well. Looking only at the contents of organic fluorine rather than f_x, to evaluate the amount of dye rather than the amino group fraction, yields an improved, albeit not perfect, correlation between the XPS and the corrected fluorescence data for **CS11-CW11** and **CS12-CW12**.

The origin of the discrepancy between the XPS and the fluorescence data can not be conclusively found based on the performed experiments, but the distinct difference between the pure APDIPES and the mixed silane samples, including the exceptionally high fluorine content point to differences in binding of the label dye on the pure and mixed surfaces. It is conceivable that electrostatic interactions, that are enhanced due to the positively charged nature if the pure amino surface, play a pivotal role in the binding of the dye.

These experiments were repeated on different sample set without achieving a significant increase in quality of the results, which hinds at problems in the application of such early platform dyes.

2.8.1.1 Conclusion

The platform dyes could successfully be transferred into amino reactive label dyes in a single step. The resulting dyes were found to show selective binding to amino surface functional groups, however, quantification via fluorescence or XPS was not possible. Especially the reproducibility of the binding proved challenging. Possible reasons are remnants of the starting materials that affect the labelling density of the dye and the sensitivity of the DIC/NHS chemistry on the relative amounts of the components. A possible solution to this problem is to prepare and purify the NHS-ester separately and apply it directly to the surface. But since the discrepancy in the XPS data points to an unclear relationship between the bounded dye and density of surface functional group, a finding that was reproduced in the repetition of these experiments, no further afford was spent on this labelling procedure.

2.8.2 Epoxy reactive label dye

A label dye for epoxy surface functional groups, which are of great relevance in the surface binding of biomolecules, was prepared based on **3**. The latter was treated 2-(boc-amino)-ethanethiol following the same procedure as used for **10** to yield **13**. The protecting group prevents the amino group from reacting with pentafluorophenyl moiety, facilitates handling and increases the stability of the resulting dye. Prior to surface labelling, the protection group can be removed under treatment with TFA followed by aqueous extraction with $NaHCO_3$. The resulting dye contains an amino group capable of reacting with a surface epoxy group. Preliminary experiments on mixed (3-glycidoxypropyl)trimethoxysilane (GOPTMS)/CETES surfaces revealed, however, that the binding is mainly governed by electrostatic interaction rather than covalent binding and a selective labelling in exploitable yields could not be obtained.

2.9 Cavity ring-down spectroscopy on microscope slide surfaces

2.9.1 Introduction

Based on the promising results obtained using UV/Vis absorption spectroscopy, alternative methods were sought out that could provide an enhanced sensitivity and at best spatial information in absorption spectroscopy. A known method for highly sensitive absorption measurements is the laser-based cavity ring-down spectroscopy (CRDS), which was introduced by O'Keefe and Deacon in 1988.[200] In CRDS, a pulsed light source is coupled into a high-finesse optical cavity.[201] The light pulse travels back and forth in the cavity and a small fraction of its light is transmitted each time it is reflected. This fraction can be recorded as a temporal intensity decay following a mono-exponential decay. If the light is attenuated inside the cavity by absorption or scattering, the decay time will by shortened accordingly and the absolute absorption can be determined by via the rate of absorption rather than the ratio of light intensity like in conventional absorption spectroscopy. This renders the technique resistant to fluctuation in the light intensity of the incident beam. As the light beam is travelling back and forth in the cavity, the effective path length can be as long as several kilometres. Compared to other laser spectroscopy experiments, CRDS is comparatively simple to set up. The limiting components are mainly the highly-reflective mirrors for the desired wavelength region. The absorption inside the cavity can be calculated according to:

$$A = \frac{d}{c} \cdot \left(\frac{1}{\tau} - \frac{1}{\tau_0} \right) \tag{2.15}$$

With d being the distance between the two cavity mirrors, c the speed of light and τ and τ_0 the decay time in presence and absence of sample, respectively. The major part of CRDS experiments deals with the determination of gaseous analytes as they can be introduced without distorting the cavity and the sensitivity of the setup easily be adjusted via the size of the cavity, with cavity length of up to 270 cm being reported.[202]

For non-gaseous analytes, the CRDS is considerably more complex as usually additional interfaces are required that significantly influence the decay time. Different designs have been demonstrated for measuring cavity ring-down decays in liquid phase: the simplest approach is to fill the cavity with analyte solution. Yet this approach is greatly hampered by integrating the highly-reflective surfaces in the liquid cell and the limited stability of the mirror coatings to reactive liquids. Especially for flow based measurements, special cells have been realised where the cuvette is either placed in the normal of the incident beam and reflections at the air/glass and liquid/glass interfaces appear in plane of the beam or in a brewster-angle configuration, where the cuvette is adjusted in the brewster angle to minimize the reflection of the p-polarized

beam.[203,204] The latter is limited for liquid measurements as the refractive index of the solvent needs to be matched with the cuvette material. For interfacial studies, measurement in an evanescent field using total internal reflection at the solid/liquid or solid/glass transition in different prisms were shown.[205] For the samples in question in this work, the measurement at a solid/gas interface is required. Although the evanescent wave based measurement seems favourable as it would even allow dynamic determination of the dye density at the interface, its limitation to purpose-made prisms is challenging to combine with the current substrates.

An approach that allows CRDS measurements on flat, plano-parallel samples like the commonly used microscope slides is the measurement in Brewster's angle geometry. This approach was demonstrated already for the investigation of monolayer dye films on high-quality optical glass.[206] It had been shown that a number of glass materials are suitable for measurement in Brewster's Angle, as long as they show limited absorption in the investigated wavelength region.[207]

2.9.2 Design of the CRDS setup

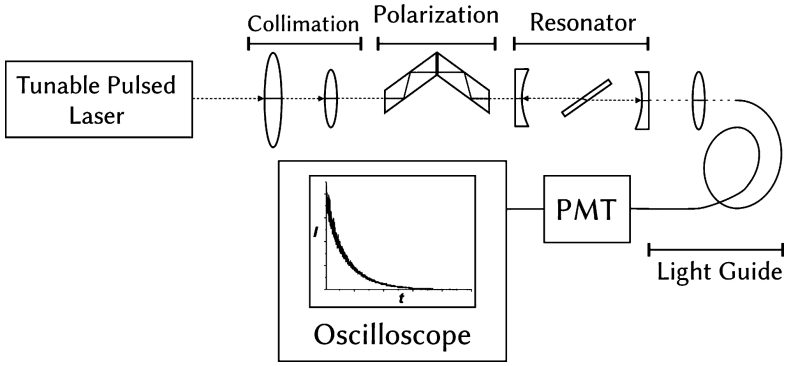

Figure 2.40: Experimental setup for scanning CRDS on microscope slides

The feasibility of CRDS on slides was investigated with the setup shown in scheme 2.40. The tunable output from the OPA was re-collimated with a two-lens setup and directed on the cavity with a periscope optic using two pinholes for adjustment. A $\lambda/2$ Fresnel Rhomb Retarder was used to adjust the polarization of the beam before coupling into the cavity. The optical cavity consisted of two highly-reflective mirrors ranging from 380 to 420 nm, mounted with five degrees of freedom each, three translational and two angular. The output was coupled into a 400 µm fiber and directed on a photomultiplier tube (PMT) which was read-out using a 200 MHz oscilloscope.

Prior to the measurement on the slide, the cavity is adjusted. First, the back reflection of the first cavity is superimposed with the incoming beam by adjusting the angular alignment. Secondly, the reflections inside the cavity are superimposed using the two translational and the two angular axis of the second mirror. Than, the fibre coupling lens is positioned to achieve maximum signal. When the Cavity ring-down signal is visible on the oscilloscope, the translational positions of both mirrors and the angular position of the second mirror are incrementally adjusted until maximum decay time is reached. For analysis, each decay consists of 128 averaged measurements and is stored directly on a USB flash drive and analysed with a mono-exponential decay in OriginPro. Typical decay times for the empty cavity were around 1.5 µs at 410 nm.

2.9.3 Scanning CRDS on slides

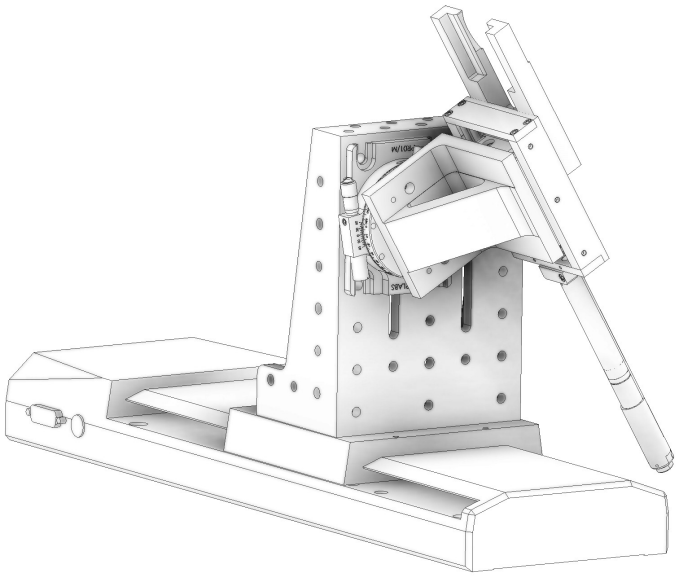

Figure 2.41: Drawing of Slide Holder, with axis 1 mounted on the rotational stage and the whole mounted on the axis 2 stage

The complete sample holder provided three adjustable axis, with the two translational axis being step-motor driven (see Fig. 2.41). A microscope slide holder was mounted on a translational stage with 25 mm travel range which was mounted in 90° on a rotational stage to position the slide in Brewster's angle. As the pitch moves the whole translational stage, the step distance of the translation stage always equals the step distance of the incident beam spot. The translation/pitch setup itself is mounted on a long-distance stage providing 300 mm of travelling

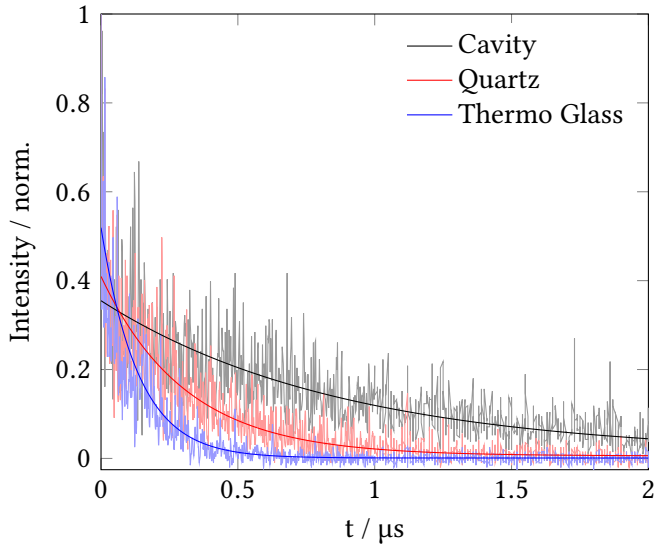

Figure 2.42: Decay profiles with mono-exponential fit of the empty cavity (τ = 870(20) ns), with quartz glass (τ = 307(7) ns) and with ThermoFisher Ultraclean glass (τ = 135(2) ns)

Table 2.20: Cavity ring-down times (τ) at 410 nm and absolute absorption (according to Eq. 2.15) on Quartz from three measurements on one spot and single measurements on six spots (Empty Cavity: τ = 1.2(1) µs)

spots	meas./spot	τ [µs]	Abs ($\cdot 10^{-3}$)
1	3	0.450(2)	2.01(1)
6	1	0.39(5)	2.6(5)

range for automated translation along the non-tilted axis. A slight disadvantage of this design is that the slide central axis is not on the rotational axis, so that a compensation by moving the slide holder on the y-axis translation stage is necessary. The slide is introduced in the adjusted cavity and the angle optimized, until maximum decay time is reached (Brewster's angle). If no cavity ring-down decay is visible, adjustment of the polarization plane might be necessary. Afterwards, the second cavity mirror is adjusted incrementally. The programs of the two translation stages are used to move the sample. To access the feasibility of single-wavelength CRDS on glass substrates, quartz slides and high-quality glass slides were investigated in comparison to an empty cavity (see Fig. 2.42). As it can be seen, both materials reduce the cavity ring-down time significantly. This is most likely due to absorption in the glass itself. In agreement with the transmission spectra of the different glasses (Sec. 2.7), quartz glass shows less absorption than soda-lime glass. Yet, CRDS measurements appear to be possible on both materials.

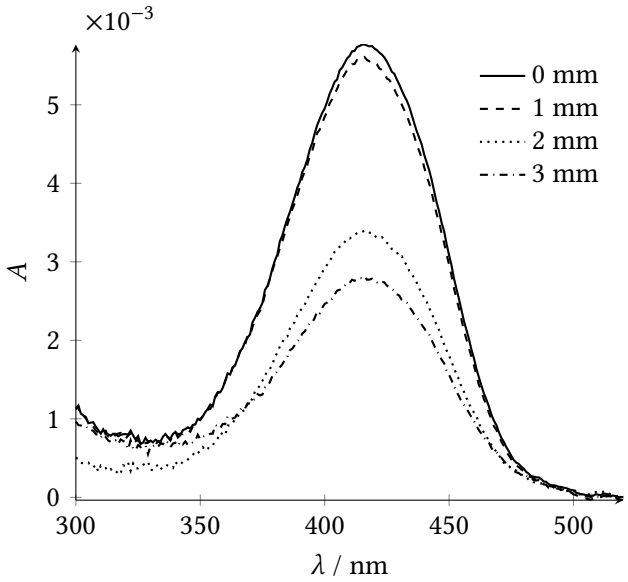

Figure 2.43: Absorption spectra (background subtracted) of the third region on the Coumarin 153 test slide

The limitation in conventional spectrophotometry are not only the sensitivity of the instrument, but also the error in the background contribution to the measured absorption spectrum. Fortunately, this background can be approximated in spectra containing regions where the dye in question does not absorb. To estimate the error provided by the pure materials, different glasses were scanned.

Table 2.20 shows the values for the repeatability of a single spot and multispot measurements. Although the single spot measurement shows a good precision, the stability across the slide leaves much to be desired. However, this fluctuation is consistent with differences in background contribution seen in conventional spectrophotometry, although additional reduction due to a slight change of alignment upon moving the slide have to be considered as well.

To evaluate the capabilities in determining the amounts of dye on a slide surface, a test quartz slide with Coumarin 153 was prepared. A cotton stick was dipped into a solution of Coumarin 153 in ethanol and wiped across the slide, three stripes were prepared in this fashion (see Fig. 2.45).

The Coumarin 153 slide was scanned in the spectrophotometer. The design of the spectrophotometer only permits scanning at the ends of the slide, whereas the microscope slide holder for CRDS only allows scanning in the central region. Accordingly, direct comparison of the results is not possible since they are obtained on different regions.

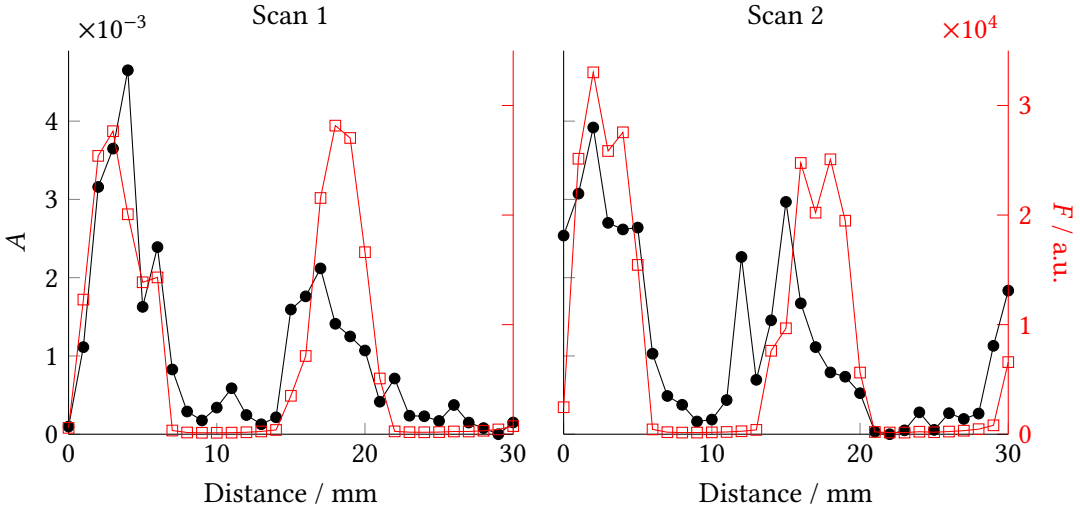

Figure 2.44: Optical absorption (A) at 400 nm as determined by CRDS (—●—) and fluorescence intensity (λ_{Ex} = 488 nm; λ_{Em} = 500 to 550 nm)(—□—) versus the scan distance for the first (left) and second (right) scan

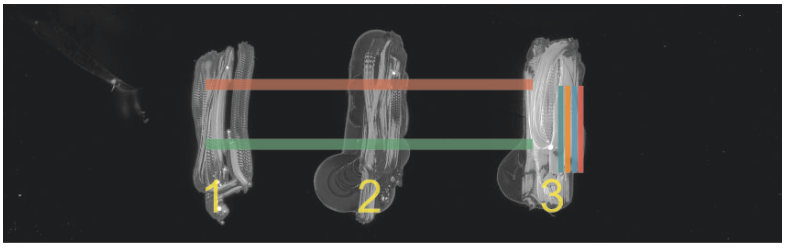

Figure 2.45: Microarray scanner image of the Coumarin 153 test slide (λ_{Ex} = 488 nm; λ_{Em} = 500 to 550 nm), first (red) and second (green) CRDS-scan trails and region numbers

Figure 2.43 shows four absorption spectra taken at different positions within the region three of the test slide. the absorption reduces going to the edge in accordance with the fluorescence scan. Two scans were performed with CRDS, each spanning 3 cm with a step length of 1 mm. The measured decay times varied from τ = 200 ns for regions with dye to 550 ns for the highest background decay time. The empty cavity showed a decay time of τ_0 = 1.32 µs. To calculate the absorption on the slide, the longest decay time per profile was used as τ_0 in Eq. 2.15 which is equivalent to a background subtraction of the quartz slide contribution to the measured decay time. To compare the measured absorption to the fluorescence intensity, an intensity profile was extracted along the estimated scan path using ImageJ and averaging the pixels to a step size 1 mm × 1 mm.

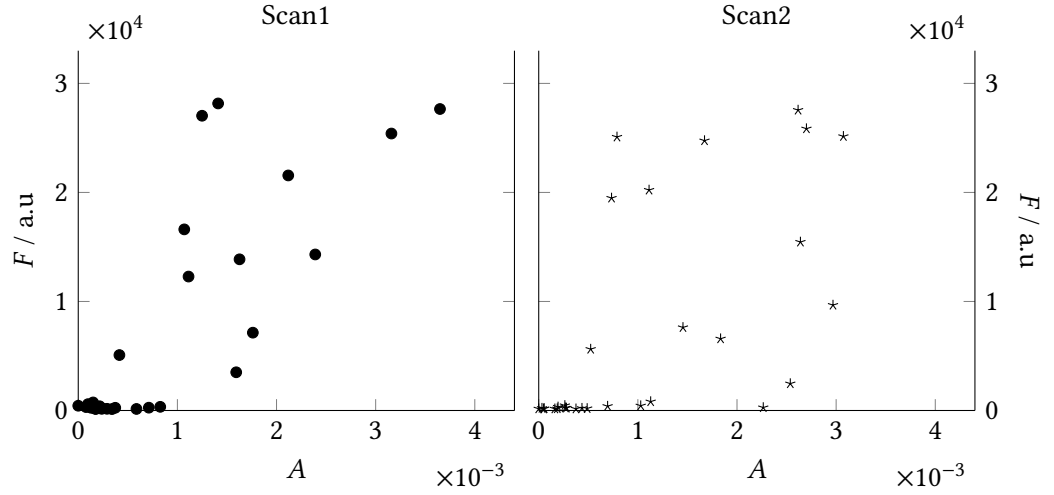

Figure 2.46: Fluorescence intensity (λ_{Ex} = 488 nm; λ_{Em} = 500 to 550 nm) vs optical absorption (A) at 400 nm (CRDS) for the first (left) and second (right) scan

Figure 2.44 shows the absorption as determined by CRDS and the fluorescence intensity extracted from the microarray scan versus the scan distance for both scans. Especially the first scan shows a good overlap of fluorescence and absorption, whereas the second scan seems to contain some outliers, probably from dust speckles on the slide. The correlation between fluorescence and absorption is shown in Figure 2.46. The first scan along the slides obviously shows a better correlation with the points scattering along the linear line, the second scan shows a comparable trend, yet with a significantly higher error. A certain deviation can be explained by the errors in the spatial reconstruction of the two methods, as the *relative* position in CRDS is significantly less precise (around ±0.5 mm) as in the microarray scanner, whereas the *absolute* position in the microarray scan is not perfectly determined, since the scanner only scans an area of 72 mm × 22 mm from a slide with the dimensions of 75 mm × 25 mm, cropping ~1.5 mm at each edge. Additionally, changes of scattering on the slide and in the efficiency of the Brewster transmission account for errors in the CRDS absorption. Careful examination of the two scans shows that, in contrast to the measured fluorescence, which is roughly the same in the different regions, the absorption appears lower in the second region, so does the background at the end of the scan. This can originate from imperfections in the slide or slight variations in the sample alignment, which would result in an decrease of the decay due to unaccounted angular misalignment. Since the procedure to prepare the test slide for this experiment is not as sophisticated as the one used for the surface functionalized samples of the earlier sections, it can be expected, that this effect is less severe for such samples. A clear evaluation of the CRDS for quantitative surface analysis would require a measurement of the employed surface label,

yet label **1** shows only marginal absorption at 400 nm (see Figure 2.34) and can not be measured with the given system. Apart from suitable mirrors, further experiments require a concept for efficient background correction if substrates like common glass slides are used, since their imperfection results in an unstable background contribution. If spectrally resolved data are available, as it is the case for the spectrophotometer, this work already showed how the background can be accounted for (see Section 2.6.2). In the single-wavelength CRDS experiment such a correction is not possible and the variation of the background can not be straightforwardly assessed, but different procedures are conceivable to be employed if suitable mirrors are installed:

Stepwise change of the absorption wavelength is possible with the applied laser setup and would allow scanning at different wavelengths. The disadvantage is that the adjustment has to be done manually for each wavelength. Since the laser is based on femtosecond Ti:Sapphire laser, supercontinuum generation is possible which in combination with a streak camera could also provide a full CRDS spectrum by simultaneously recording the decay time for all wavelengths.[208,209] However, neither the supercontinuum generation nor a suitable streak camera are available. A simple way to account for the background would be to use a reference wavelength in a region where no absorption is expected and, by applying mirrors with satisfactory reflection at the desired measurement wavelength *and* the reference wavelength, determine the ring-down times for both wavelengths simultaneously by pumping the cavity with both beams in good spatial overlap and measure the intensity decay for both independently by using a beam splitter and two PMTs behind the cavity. This way, two values would be obtained for each spot. One value would correspond to the absorption of the dye plus background and the second to the background alone. The residual of the laser input at 800 nm from the optical parametric amplifier (OPA) would be an ideal candidate as reference. Most of the currently investigated dyes do not absorb at that wavelength, so that it would be only influenced by changes in alignment and scattering and this output is available without change in alignment or temporal position irrespective of the main output wavelength of the OPA. The lack of suitable mirrors, however, permitted the investigation of this approach. Nonetheless, the clear advantage of CRDS on slides is not necessarily higher sensitivity but the spatial resolution obtained with the point-scanning design. As Figure 2.44 already shows, it is possible ot correlate fluorescence and absorption at different positions with each other, whereas the absorption obtained from the spectrometer only contains very little spatial information and only averaged data can be compared.

3 Conclusion

In this work a novel dual-mode labelling of functional groups on surfaces could be developed. Different approaches for the design of highly fluorinated label dyes were realized, including a versatile modular approach. The fluorescence properties of those dyes were initially characterized to prove their suitability for the desired approach. A well-designed fluorescence probe with sufficient fluorine content to simultaneously serve as chemical label for XPS and fluorescence was applied in a novel analysis procedure to determine the relative amounts of dye on vapour deposited silane slides.

Despite proving the general feasibility of this dual-labelling method for the very first time, these early results also pointed to the strong influence of fluorescence quenching that can lead to a misleading interpretation of the fluorescence method. Only due to the dual-mode properties of the method and the non-saturated information of XPS this effect could be clearly identified.

The full potential of the dual-mode method can only be determined if the full dynamic range of both methods is known. Yet, no preparation was found that is immediately suitably to prepare the necessary surfaces of variable functional group density. From the known procedures, the silane derivatization of glass surfaces via vapour deposition was the method of choice for the fabrication variable functional group density surfaces. The measurement of static and dynamic contact angles was introduced to consecutively optimize all influential steps of the vapour deposition approach: the activation of the slides, the preparation of the vessels under an inert atmosphere, the deposition itself and the post-treatment. Numerous combinations of functionalized and inert silanes were tested towards their application in a one-step co-deposition to produce binary surfaces with controlled functional group density.

Finally, a reliable method based on the two mono-alkoxy silanes (3-aminopropyl)diisopropylethoxysilane (APDIPES) and (3-cyanopropyl)dimethylmethoxysilane (CPDMMS) was developed. The silane density of both individual silanes on surface oxidized silicon was quantified by SR-XPS via the Si 2p core-level spectra and independently by reference-free TXRF via the nitrogen content. It could be shown that both silanes produce layers with similar density of 2 to 3 silanes per nm^2. The similarity of the surfaces allowed reliable application of Cassie's Law, from which the relative fractions of the silanes on the surface could be calculated. The special

role amino-functionalized silanes could be elucidated to deepen the understanding of the formation of such silane layer. These quantified surfaces were treated with the label compound and a linear relationship between the determined functional group contents and the fluorescence intensity of the label compound, as well as the amino ratio determined via the N/F ratio in XPS could be found. This, finally, lead to a clear assessment of the LODs of XPS and fluorescence scanning and the dynamic range both methods cover. Additionally, it could be shown that such labelled samples were stable to store and analyse on different instrumentation at a later time, both in XPS and fluorescence.

Based on the obtained knowledge, the fabrication of variable functional group density slides was expanded to the application of (3-aminopropyl)triethmendeleyoxysilane (APTES) and (2-cyanoethyl)triethoxysilane (CETES). On the surfaces obtained from these tri-alkoxy silanes, the mechanistic findings of the mono-alkoxy silanes could not be reproduced, as it was reasonable to explain. The fluorescence intensity was again strongly affected by fluorescence quenching, so that a novel approach to account for such fluorescence quenching based on the measurement of the fluorescence lifetime was developed and successfully applied to significantly enhance the dynamic range of the fluorescence methods. UV/Vis photometry allowed to obtain quantifiable absorption spectra of the label compounds bound to the substrate. The quantitative nature of the underlying labelling reaction allowed to transfer the absorption coefficient of the initial labelling compound to its surface bounded state through solution reaction in the cuvette. Accordingly, the absolute amounts of dye on the surface could be obtained and subsequently, through the ratio of the labelling on the surface as it can only be obtained from XPS, transferred to an absolute quantification of the surface functional group. This combination of optical methods and X-ray photoelectron spectroscopy provides one of the most precise laboratory-based procedures known for surface functional group quantification.

The different dyes prepared containing the pentafluorophenyl moiety were transferred to amino group labels in a single step and applied to surfaces based on APDIPES:CETES. Unfortunately, their performance could not rival the one of the initial label. An epoxy label based on the same platform also showed equivocal results so that the full potential of the platform still remains to be shown.

To overcome the sensitivity limitation of UV/Vis photometry, a laser based setup to perform highly precise cavity ring-down spectroscopy (CRDS) on slides positioned in Brewster's angle was developed. A preliminary investigation of this setup provided valuable insight in the capabilities and limits of the method, especially in terms of sample quality. Concepts of different demand were proposed to enhance the capabilities of the CRDS method.

4 Outlook

The dual-mode labelling concept can now easily be transferred to a reference system for fast and reliable surface functional group quantification. The perils in fluorescence quenching that does not only originate form high surface functional group densities alone, but also from local bunching of functional entities can be identified and accounted for. Reliable quantification can be performed in combination with either fluorescence lifetime measurements, spectrophotometry and/or XPS, whichever method is available and applicable. Accordingly, the local structure of a functionalized surface can be characterized with these macroscopic measurements. The addition of ToF-SIMS, that could only be applied in a proof-of-concept, can provide a transfer from XPS to fluorescence methods, especially when using substrates that are difficult to measure with one of those methods. The high spatial resolution of ToF-SIMS can provide important information about local heterogeneity. The CRDS on the other hand provides the possibility to expand the spectrophotometric quantification to higher sensitivity and, more importantly, spatial resolution to characterize the homogeneity of the surface functional group density.

The experience that was gained in applying a multitude of label dyes on similar substrates enables the concise design of next-generation labels with even superior performance and specificity for different surface functional groups. The synthesis pathway initiated through this work following a novel gold catalysis enables the preparation of priorly hardly available pyrrole precursors.

The developed preparation of surfaces with variable surface functional group densities, although not the focus of this work, is expected to have a great impact. Showing that this simple one-step method is feasible promises to expand this concept to an application where surfaces with exactly the required density of surface functional groups can be obtained. This can not only be beneficial for microarrays that obtain maximum sensitivity, but can also be applied to particles and suspension assays. Apart from an application as an array substrate, these surfaces will be applicable in the characterization of novel quantification procedures. Also, fluorescent surfaces with high stability and different fluorescence intensities are highly required as calibration tools for surface fluorescence measurements, including microarray scanning. A tangible application is currently investigated in cooperation with Scienion AG.

5 Experimental Details

5.1 Chemicals

Chemical (Purity)	Supplier
2,4-dimethyl-3-ethylpyrrol (97 %)	Sigma-Aldrich
2,4-dimethylpyrrol (97 %)	Sigma-Aldrich
2-(boc-amino)ethanethiol (97 %)	Sigma-Aldrich
(3-aminopropyl)diisopropylethoxysilane	FluoroChem
(3-aminopropyl)triethmendeleyoxysilane (99 %)	Acros
(2-cyanoethyl)triethoxysilane (97 %)	Alfa Aesar
(3-cyanopropyl)dimethylmethoxysilane	FluoroChem
(3-glycidoxypropyl)trimethoxysilane (98 %)	ABCR
3-mercaptopropionic acid (≥98 %)	Merck
acetic acid (99.8 %)	Merck
acetone (≥99 %)	Chemsolute
acetonitrile (spectr.)	Acros
acetonitrile (analytical)	Fisher Chemical
ammonium hydroxide (32 % in water)	Merck
Coumarin 153	Lambda Physics
cylcohexane (≥99.5 %)	Chemsolute
dibutyl ether (spectr.)	Sigma-Aldrich
dichloro methane (anhydrous, 99.8 %)	Acros
dichloro methane (≥99.5 %)	Fisher Chemical
diethyl ether (spectr.)	Sigma-Aldrich
ethanol (spectr.)	Merck

Chemical (Purity)	Supplier
ethanol (≥99.5 %)	Chemsolute
ethyl acetate (≥99.5 %)	Chemsolute
n-hexane (spectr.)	Sigma-Aldrich
hydrogen chloride (37 % in water)	Merck
hydrogen peroxide (30 % in water)	Chemsolute
isopropyl alcohol (99.5 %)	Fisher Chemicals
KOH (semiconductor grade)	Sigma-Aldrich
(3-mercaptopropyl)trimethoxysilane (95 %)	FluoroChem
methanol (spectr.)	Acros
methanol (99.7 %)	Chemsolute
N-(6-aminohexyl)aminomethyltriethoxysilane (95 %)	ABCR
N,N'-diisopropylcarbodiimide (99 %)	Sigma-Aldrich
N,N-diisopropyl-ethylamin (99 %)	Sigma-Aldrich
N,N-dimethylformamide (anhydrous,99.8 %)	Sigma-Aldrich
potassium carbonate (K_2CO_3, ≥99.0 %)	Sigma-Aldrich
pentafluorobenzaldehyde (98 %)	Sigma-Aldrich
n-propyltrimethoxysilane (≥98 %)	Alfa Aesar
Rhodamine 101	Sigma-Aldrich
Rhodamine 6G	Sigma-Aldrich
Rhodamine B isothiocyanate	Sigma-Aldrich
sodium sulfate (Na_2SO_4, (≥98.5 %))	Chemsolute
sulfuric acid (95–97 %)	Fisher Chemical
tetrahydrofuran (spectr.)	Sigma-Aldrich
toluene (spectr.)	Sigma-Aldrich
toluene (anhydrous, 99.85 %)	Acros
trifluoroacetic acid (99.5 %)	ABCR

5.2 Materials

Corning plain, pre-cleaned microscope glass slides (75 mm × 25 mm) were usually were used as substrates. Other substrates were CrysTec silicon wafers, cut into 75 mm × 25 mm pieces, Nexterion B slides from Schott, UltraClean slides from ThermoFisher, fusion-drawn glass slides from Corning (on special request) and quartz slides from . Plasma activation was performed with a Zepto Plasma system (Diener Electronic) and sonication in an Elmasonic P 60 H (Elma Hans Schmidbauer); centrifugation of the slides was carried out in a microarray high-speed centrifuge (Arrayit). Vapor deposition was performed in 100 ml DURAN® premium bottles with high-temperature PPS lids and silicone/PTFE sealing, if not mentioned otherwise.

5.3 Analytical techniques

The instrumental uncertainties involved in the different techniques are listed for the individual instruments. Experimental errors given in this thesis are typically calculated as the standard deviation from ≥3 individual measurements.

5.3.1 Contact angle measurements

CA measurements were performed on an OCA 15Pro (Data Physics Instruments). The sample holder was a TPC 150 with a Peltier controlled temperature of 22 °C, measurements were usually performed under a mild stream of nitrogen, the flow speed was adjusted to minimal distortion of the drops. Samples were usually dried *in vacuo* prior to measurement, if not indicated otherwise. The liquid dosing was performed electronically, whereas the sample table was manually adjusted in three axes via high-precision mechanics. Drop shapes were analysed with SCA20 software (Data Physics). At least ten drops (2 µl each) of MilliQ water were measured per slide for the static contact angle. For the ARCA measurement, the needle was placed in a drop of ≈5 µl and 10 µl were added at a speed of $0.2\,\mu L\,s^{-1}$. After a resting time of 2 s, the same volume was removed and the grow/shrink process was repeated after another 2 s rest. The videos recorded were with a frame rate of 3.5 Hz. The measurements were analysed with SCA20 by determining the contact angles of the drop in every frame. The dynamic contact angles were determined under aid of the drop base diameter, θ_{adv} is marked by the point at which the drop base diameter stops increasing, θ_{rec} is read just before the diameter decreases again. Those points are chosen since the drop is not moving to limit the distortion on the drop

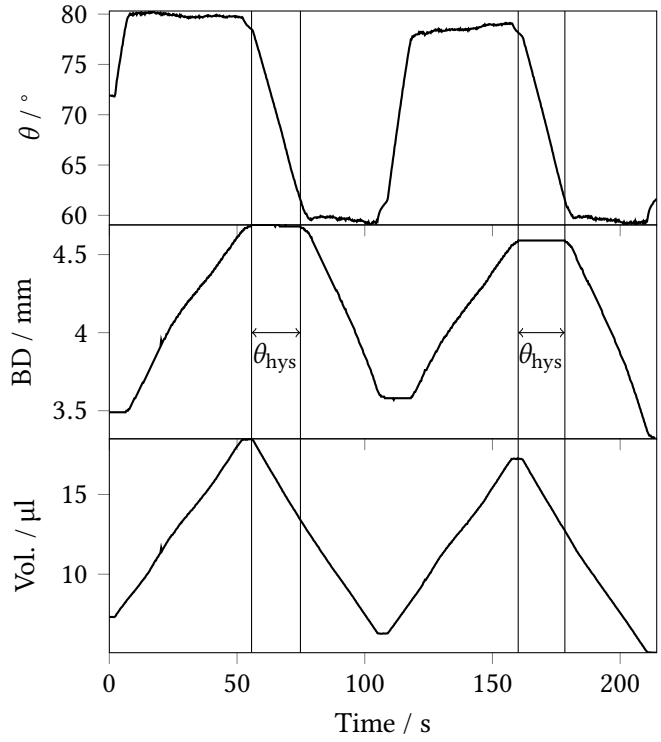

Figure 5.1: Comparison of changes in contact angle (θ), drop base diameter (BD) and drop volume (Vol.) during the advancing and receding contact angle (ARCA) measurement. The according dynamic contact angles are read at the indicated lines

shape. Figure 5.1 compares the changes in contact angle, the drop base diameter and drop volume during the ARCA measurement. For both methods the uncertainty of the video system amounts to ±0.1° while determination of the drop shape with the software is associated with ±0.2°. The lowest contact angle that can be determined automatically is 5°, lower contact angles require manual adjustment and are associated with a higher arrow.

5.3.2 Fluorescence scanning

Slides were scanned with 488 and 532 nm laser excitation (λ_{Exc}) and a green (λ_{Em} = 550 to 600 nm) or blue (λ_{Em} = 500 to 550 nm) emission filter (see Fig. 5.2) using a Molecular Devices Axon GenePix 4300A fluorescence scanner at 20 µm (occasionally 5 µm) resolution and 16-bits-per-pixel signal collection. The images were either analysed with GenePix Pro 7.1 software (Molecular Devices) or with ImageJ. For analysis with GenePix, a grid of spots with a spot diameter of 1 mm, which size was adjusted to the coloured area, but contained at least 100 spots, was used to obtain the mean intensity per spot. The averaged signal was obtained by

averaging over all spots. For analysis with ImageJ, a frame filling the coloured area, minus 1 mm at each edge was used to average over all pixels inside the frame. The results obtained with both programs are comparable. The slides were scanned prior and after reacting with label dyes and the fluorescence intensity of the dye is obtained by subtracting the average intensity from the unlabelled slide from the measured average intensity. It is noteworthy that surfaces of higher quality do not comprise significant background fluorescence. The scan of an entire slide (max. scan area = 72 mm × 22 mm, one λ_{Exc}) at 20 µm resolution is completed within 90 s. The repeatability of measurements at a given spot is ±2 %, signal variation across a uniform slide lies within 5 %. The high reproducibility of the fluorescence scanner allows to treat each pixel as an individual measurement, so that averaged intensity and its standard deviation are typically based on $>10^6$ measurements.

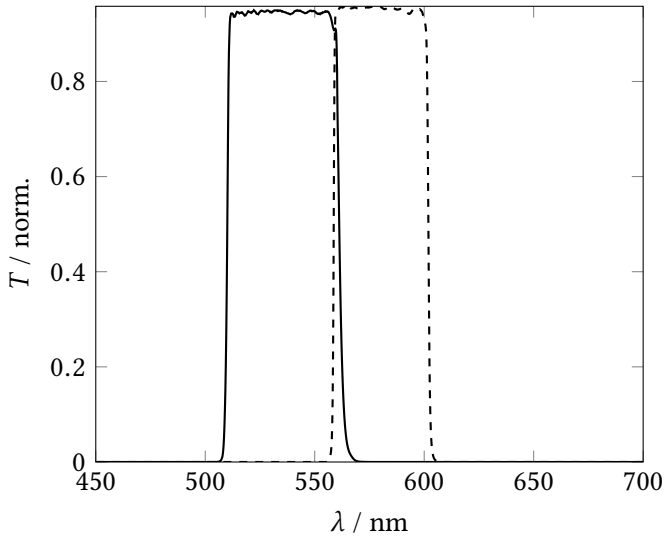

Figure 5.2: Transmission spectra of the Standard Blue (——, λ_{Em} = 500 to 550 nm) and the Standard Green (- - -, λ_{Em} = 550 to 600 nm) emission filter installed in the GenePix microarray scanner

5.3.3 X-ray photoelectron spectroscopy.

XPS measurements were carried out with a Kratos Analytical AXIS Ultra DLD photoelectron spectrometer both at BAM and NPL. XPS spectra were recorded using monochromatized Al Kα excitation at pass energies of 80 eV for survey and 20 eV for high-resolution core-level spectra. The charge neutralizer was used. The electron emission angle was usually 0° (with respect to the surface normal) and the source-to-analyzer angle was 60°. Occasionally, an electron emission angle of 60° was used to enhance surface sensitivity. However, problems with charge

compensation at that angle permitted stringent use. Survey scans and high resolution Si 2p, C 1s, N 1s, O 1s and F 1s core-level spectra were analyzed with CasaXPS (Casa Software). For curve fitting of the core-level spectra, a Gaussian/Lorentzian product function peak shape model was used in combination with a Shirley background. Samples were cleaned by rinsing with IPA and drying under an Ar-jet prior to transfer into the instrument.

Regarding the uncertainty of the quantitative XPS measurements a combined uncertainty of measurement for the quantification of the atomic fraction of Fe in a Fe-Ni alloy was recently determined to 3.3 at%.[180] The relative uncertainty of an overlayer thickness measurement was determined to 15 % for SiO_2 overlayers on Si(100) with nominal thicknesses of 4, 6 and 8 nm.[210] The uncertainties for quantification of atomic fractions and overlayer thicknesses are expected to be distinctly higher (e.g. twice as much) for non-ideal samples such as thin organic silane films on silicon oxide surfaces as investigated in this thesis.

5.3.4 Epifluorescence microscopy

Wide-field fluorescence images were recorded at NPL on an IXZ-1 microscope (Olympus) equipped with an EMCCD DV887 (Andor Technology) and a mercury vapour lamp, using 10× or 50× magnification. The filter cube was an U-MWIB3 Filter Cube from Olympus which is roughly comparable to the Standard Blue Filter in the fluorescence scanner. A neutral density filter was used to reduce the lamp intensity for minimized photo-bleaching. Small defects or peckles on the surface were used to adjust the focus. The recorded images were analysed with ImageJ, the entire image was used to create the averaged intensity. The signal variation across an image was ~10 %

5.3.5 Atomic force microscopy (AFM) imaging.

AFM imaging was performed on either a Cypher or a MFP-3D system (both Asylum research) at NPL. All measurements were carried out in intermittent contact (tapping) mode using PPP-NCHR-type cantilevers (Nanosensors™) at room temperature. To enhance the reflectivity of the laser beam, the cantilever is coated with 30 nm thick Al on the detector side. Typical values of resonance frequency and quality factor of the cantilevers were ca. 280(30) kHz and 440(60) kHz, respectively.

5.3.6 Time-of-flight secondary ion mass spectrometry (ToF-SIMS)

ToF-SIMS measurements were performed on a TOF.SIMS 5 from ION-ToF and were analysed using the SurfaceLab 6 software provided by the manufacturer.

5.3.7 Spectrophotometry

Absorption spectra were recorded on an Analytik Jena Specord 210 Plus spectrophotometer. According to the manufacturer, the instruments provides a wavelength accuracy of ±0.1 nm, a wavelength reproducibility of ≤0.02 nm, a photometric reproducibility of ≤0.0005 A and noise level of ≤0.0001 A at 500 nm.

Liquid samples: Solution spectra were obtained in 1 cm Hellma quartz cuvettes using solvents of spectroscopic purity at room temperature. In a typical experiment, a cuvette filled with the according solvent is used as a reference. For dye spectra, the cuvette for the dye is scanned filled only with solvent prior to adding the dye in concentrated solution and this reference spectra is manually subtracted using OriginPro. The spectra are recorded with a slid width of 1 nm, a resolution of typically 0.5 nm and an acquisition speed of 50 nm s^{-1}.

Solid samples: Glass slides were scanned by recording spectra on ten different areas (approx. spot size: 1 mm × 15 mm) using the automated scanning accessory. A cleaned and otherwise untreated slide was used as reference. The spectra were averaged and any background remaining from differences in scattering distortion was subtracted manually using the background correction from Origin 9.1Pro. Spectra were recorded with a slid width of 2 nm at 1 nm resolution and acquired with 10 nm s^{-1}.

5.3.8 Fluorescence spectroscopy

Fluorescence spectra were obtained on a FluoroMax4P spectrometer from HORIBA Jobin Yvon. According to the manufacturer, the instrument provides a wavelength accuracy of ±0.5 nm and a signal-to-noise ratio of 3000:1.

Liquid samples and quantum yields: Solution spectra were obtained in 1 cm Hellma quartz cuvettes using solvents of spectroscopic purity at room temperature. The cuvettes were placed in 90° excitation-to-emission geometry. Emission and excitation spectra were background corrected with a spectrum of a solvent-only cuvette. Emission spectra were corrected with the spectral sensitivity correction provided by the manufacturer. Quantum yields were determined using the method described in ref. 211, with Rhodamine 6G with Φ_f = 0.95 in EtOH as primary standard.[212]

Solid samples: Solid samples were analysed in a Front-Face setup with a collecting lens in 45° to the excitation beam and the sample in 60° with respect to the surface normal. The spectra were obtained from five averaged scans and an according scan of an cleaned and otherwise untreated slide was used as a background correction. Remaining background was corrected in OriginPro comparable to the absorption spectra.

5.3.9 Time-correlated single photon counting

Fluorescence lifetimes were determined with a unique customized laser impulse fluorometer with picosecond time resolution. The 80 fs pulses provided at 800 nm with a repetition rate of 82 MHz by a frequency-doubled Nd:YVO_4 laser (Spectra Physics Millennia Xs) pumped Ti:sapphire laser (Spectra Physics Tsunami) were used to seed a regenerative amplifier (Spectra Physics Spitfire P-5K), whereby pulse amplification was obtained by pumping with a frequency-doubled Nd:YLF laser (Spectra Physics Evolution X) operated at 5 kHz. The typically 90 fs long output pulses were fed into an OPA (Spectra Physics OPA-800-F-HGII) and used to generate the respective excitation light by frequency quadrupling the idler of the OPA.

The laser beam was attenuated with a double prism attenuator from LTB and typical excitation energies were in the nanowatt-to-micro-watt range (average laser power). The fluorescence was collected at a 90° angle through a subtractive double monochromator (AMKO Model 01-002S). The fluorescence decay curves were recorded with a time-correlated photon counting setup employing a microchannel plate photomultiplier tube (Hamamatsu S4753 with amplifier Hamamatsu C4267), two constant fraction discriminators (modified Tennelec C4267) and a time-to-amplitude converter (Tennelec TC864). After A/D conversion, the signals were stored in a micro channel analyser (Ortec Spectrum ACE 4K). With typical response functions of 30 to 50 ps (full width at half maximum), the time division was 1.2 ps. The experimental accuracy was determined to ±3 ps. The fluorescence lifetime profiles were analysed using the Horiba Scientific software package DAS 6.The accuracy of the fit of the single decays, as judged by reduced chi-squared (χ_R^2) was always acceptable yielding values of $\chi_R^2 < 1.2$ for solution measurements. Slightly higher χ_R^2 values were accepted for multi-exponential decay measurements on surfaces. The uncertainty of the fitted lifetime is usually associated with <0.5 %.

Solid, flat samples were measured in front-face configuration with a 30° angle of incidence and an angle of 60° between surface normal and observation axis.

5.3.10 Photostability

The photostability of dyes was measured with a customized irradiation setup. The beam of a frequency-doubled Nd:YVO_4 laser (Spectra Physics Millennia Xs) operating in controlled power mode is directed on an SH05 beam shutter operated with a SC10 shutter controller (both from Thorlabs). This allows precise control of the irradiation time on the sample. Behind the shutter, the beam is directed on a cuvette holder (CVH100, Thorlabs) in a 30 mm cage setup, the beam is adjusted to cage centre, which ensures optimum illumination of the cuvette. The fluorescence is collected with an optical fiber and directed on an HR4000 spectrometer (Ocean Optics) and the intensity trace of the integrated fluorescence band is recorded with SpectraSuite program provided by the manufacturer. The measurements were either performed in 50 µl quartz cuvettes (Hellma) or in Eppendorf UVette cuvettes filled with 100 µl. In either case the entire solution is irradiated by the laser beam to ensure reliable measurements. The optical absorption was adjusted to $A = 0.1$ at 532 nm to ensure comparability of the measurements for the different dyes. The laser output power is adjustable between 0.2 to 6 W. Since the measurements were only compared qualitatively, a detailed analysis of the involved uncertainties was omitted.

5.3.11 Cavity ring-down spectroscopy

Cavity The output of the OPA at 410 nm described in 5.3.9 was directed on a periscope, which was used to align the laser beam on the cavity with the aid of two pin-holes. This free-space coupling involves long beam paths of >2 m. Alternatively, the beam can be coupled into a small-core (10 µm) multi-mode fiber and the beam re-collimated with a convex lens ($f = 4.5$ mm) with fibre coupling mounted on a five-axis positioning stage (Newport) for fast beam alignment. The input and the output optics of the cavity, including pin-holes, Fresnel rhomb and fibre coupling, are mounted on small optical bread-boards, elevated from the table level by ~20 cm. A $\lambda/2$ Fresnel Rhomb Retarder (FR600HM, Thorlabs) was used to tilt the polarization plane of the laser beam. Highly reflective mirrors (HR, 0°, 380 to 420 nm, plano-concave, $r = 25$ cm both sides coated) from LayerTec were mounted in kinematic mirror mounts with differential adjustment (KS1D. Thorlabs), to provide pitch and yaw, on a XYZ dovetail translation stage (DT12XYZ, Thorlabs), to provide the three translational adjustments. The pitch and yaw of the first cavity mirror is adjusted so that the back-reflex of the laser beam overlaps with original laser beam, e.g. that the incoming light beam is perpendicular to the flat rear of the mirror. The second mirror was mounted in a distance of ~50 cm to yield a concentric configuration of the cavity. The mirror is aligned so that all reflexes overlap with the central beam. The output of the cavity is coupled into a fiber with a fiber coupler (PAF-SMA-11-A, aspheric FiberPort for SMA Con-

nector, $f = 11$ mm, Thorlabs). A blue coloured glass filter in combination with a pin-hole and a short lens-tubing is used to limit the amount of scatters light coupled into the fibre. The output is collimated in a custom-made PMT housing with a SMA fibre connector on a PMT (E1761-04 with a C4710-01 HV supply, both Hamamatsu), the detector signal is analysed directly with a TDS2000 oscilloscope (Tektronix) with 200 MHz and 2.5 gigasamples per second. The cavity is optimized by adjusting all parameters of the output mirror and the translational parameters of the input mirror iteratively until maximum decay time is reached. For an individual decay time measurement, 128 decays were recorded and automatically averaged. The resulting decay was stored on an USB flash drive and analysed with Origin9.1Pro. A 6 GHz oscilloscope (TDS820, Tektronix) was also employed, but decay analysis of those decays is cumbersome since the individual pulses of each pass through the cavity are base-line separated on this instrument and apparently difficulties in triggering lead to a non-exponential signal being recorded. The uncertainties involved with the different components were not determined.

Sample holder On a large, motorized high-precision linear translation stage (M-511, PI), a large angle bracket (AP90RL, Thorlabs) is mounted to hold a directly attached rotation stage (PR01, Thorlabs). A second, smaller, motorized linear translation stage (PT1-Z8, Thorlabs) is mounted with a small angle bracket on the rotation stage. The microscopy slide holder (MAX3SLH, Thorlabs) is directly attached to the small translation stage. The rotation stage allows precise adjustment of the Brewster angle, the small translation stage allows motion along the short axis of the slide, with the relative step of the beam spot being independent of the angle. The large stage moves the whole setup to allow motion along the slides' long axis. A drawing of the setup can be found in Figure 2.41. After introducing the slide in the approximate Brewster angle into the cavity, the angle and the five parameter of the output axis are optimized iteratively.

5.4 3D representations of silane surfaces

The illustrations were created with Freemaestro from Schrödinger. The silane densities on the surface were adjusted to ~2 silanes per nm^2 for 100 % silane coverage and a labelling density of ~10 % for **1**.

5.5 Synthesis

1, **2**, **3** were synthesized according to 88. **6** and **7** were synthesized as described earlier.[120,121] **4** and **5** were synthesized by Linda Lempke according to ref. 125.

General procedure for BODIPYs 2 and 3: The corresponding aldehyde (4.0 mmol, 1.0 equiv) and pyrrole (8.0 mmol, 2.0 equiv) were dissolved in dry CH_2Cl_2 (70 ml) under argon. A few drops of trifluoroacetic acid (TFA) were added and the solution was stirred at RT in the dark until total consumption of the aldehyde (monitored by thin layer chromatography (TLC)). Tetrachloro-p-benzoquinone (983.5 mg, 4.0 mmol, 1.0 equiv) was added and the mixture was stirred for an additional 5 min. The reaction mixture was then treated with *N,N*-diisopropylethylamin (DIPEA) 5.0 ml, 28.0 mmol, 7.0 equiv) and $BF_3{\cdot}OEt_2$ (5.5 ml, 44.0 mmol, 11.0 equiv). After stirring for 15 min, the dark solution was washed with H_2O (3 ml × 50 ml). After extraction of the aqueous phase with CH_2Cl_2 (3 ml × 50 ml), the combined organic solutions were dried over Na_2SO_4, filtered and concentrated *in vacuo*. The crude product was purified by silica-gel flash column chromatography (CH_2Cl_2/petrol ether (PE) or toluene (Tol) as eluent).

8-(2,3,4,5,6-Pentafluorophenyl)-1,3,5,7-tetramethyl-4,4-difluoro- 4-bora-3a,4a-diaza-*s*-indacene (2): Compound **2** was obtained as orange crystals (414 mg, 25 %): mp: 231 °C; ^{1}H NMR (500 MHz, $CDCl_3$): δ (ppm) = 1.62 (s, 6H, 2 CH_3), 2.57 (s, 6H, 2 CH_3), 6.06 (s, 2H, 2 CH); ^{19}F NMR (471 MHz, $CDCl_3$): δ (ppm) = −159.77 (dt, 2F, J = 21.3, 7.0 Hz; 2 F_{ar}), −150.77 (t, 1F, J = 20.9 Hz, F_{ar}), −146.39 (dd, 2 F, J = 64.5, 32.1 Hz, BF_2), −139.50 (dd, 2F, J = 21.9, 7.3 Hz, 2 xF_{ar}); MS (ESI+): m/z [M+H]+ calculated for $C_{19}H_{14}BF_7N_2$: 415.122, found: 415.128.

8-(2,3,4,5,6-Pentafluorophenyl)-1,3,5,7-tetramethyl-2,6-diethyl-4,4-difluoro- 4-bora-3a,4a-diaza-*s*-indacene (3): Compound **3** was obtained as orange-red crystals (1.04 g, 55 %): mp: 206 °C; ^{1}H NMR (400 MHz, $CDCl_3$): δ (ppm) = 1.02 (t, 6H, J = 7.6 Hz, 2 CH_2), 1.51 (s, 6H, 2 CH_3), 2.34 (q, 6H, J = 7.6 Hz, 6.06 (s, 2H, 2 CH), 2.55 (s, 6H, 2 CH_3); ^{19}F NMR (471 MHz, $CDCl_3$): δ (ppm) = −159.77 (dt, 2F, J = 21.3, 7.0 Hz; 2 F_{ar}), −151.30 (t, 1F, J = 20.6 Hz, F_{ar}), −145.96 (dd, 2 F, J = 65.4, 32.2 Hz, BF_2), −139.47 (dd, 2F, J = 22.7, 7.0 Hz, 2 F_{ar}); MS (ESI+): m/z [M+H]+ calculated for $C_{23}H_{22}BF_7N_2$: 471.1837, found: 471.1836.

General procedure for BODIPYs 10, 11 and 12: To a solution of 0.212 mmol of dye in 5 to 10 ml DMF are added 1.212 mmol (111 µl, 6 eq.) 3-mercaptopropionic acid and 0.127 mmol (18 mg, 0.6 eq) K_2CO_3. The mixutre was reacted over night at room temperature under an argon atmosphere. After controlling a quantitative consumption of the starting dye via TLC, the reaction is stopped through addition of water. The aqueous phase was extracted with CH_2Cl_2, the resulting organic phase was washed three times with water, dried over Na_2SO_4, filtered and concentrated *in vacuo*. The crude product was purified by silica-gel flash column chromatography using cyclohexane/ethylacetate (gradient) with 5 % acetic acid as eluent.

8-((4-((2-carboxyethyl)thio)-2,3,5,6-Pentafluorophenyl)-1,3,5,7-tetramethyl-2,6-diethyl-4,4-difluoro- 4-bora-3a,4a-diaza-*s*-indacene (10): Compound **10** was obtained as orange-red powder (51 mg, 86 %): ^{1}H NMR (400 MHz, $CDCl_3$): δ (ppm) = 1.01 (t, 6 H, J = 7.6 Hz, 2 CH_3), 2 CH_2), 1.52 (s, 6H, 2 CH_3), 1.67 (t, 2H, J = 7.9 Hz, CH_2), 2.33 (q, 4H, J = 7.7 Hz, 2 CH_2), 2.54 (s, 6H, 2 CH_3), 3.27 (t, 2H, J = 7.5 Hz, CH_2); ^{19}F NMR (471 MHz, $CDCl_3$): δ (ppm) = −146.25 (dd, 2F, J = 66.1, 32.6 Hz, BF_2), -139.82 (dd, 2F, J = 24.3, 12.2 Hz Hz, 2 F_{ar}), −132.71 (dd, 2F, J = 23.3, 11.8 Hz, 2 F_{ar}); MS (ESI+): m/z [M-F]+ calculated for $C_{26}H_{27}BF_6N_2O_2S$: 537.181, found: 537.180; MS (ESI-): m/z [M-H]- calculated for $C_{26}H_{27}BF_6N_2O_2S$: 555.171, found: 555.171

8-((4-((2-carboxyethyl)thio)-2,3,5,6-Pentafluorophenyl)-3,5-bis-(4-(trifluoromethyl)phenyl)-1,7-dimethyl-4,4-difluoro-4-bora-3a,4a-diaza-*s*-indacene (11): Compound **11** was obtained as dark red powder (81.1 mg, 71 %): ^{1}H NMR (400 MHz, $CDCl_3$): δ (ppm) = 1.26 (s, 6H, 2 CH_3), 1.77 (s, 6H, 2 CH_3), 2.74 (t, 2H, J = 7.1 Hz, CH_2), 3.33 (t, 2H, J = 7.0 Hz, CH_2), 6.43 (s, 2H, 2 CH), 7.67 (d, 4H, J = 8.4 Hz, 4 CH), 7.92 (d, 4H, J = 8.2 Hz, 4 CH); MS (ESI-): m/z [M-H]- calculated for $C_{34}H_{21}BF_{12}N_2O_2S$: 759.115, found: 759.114

8-((4-((2-carboxyethyl)thio)-2,3,5,6-Pentafluorophenyl)-3,5-bis-(3,5-bis(trifluoromethyl)-phenyl)-1,7-dimethyl-4,4-difluoro-4-bora-3a,4a-diaza-*s*-indacene (12): Compound **12** was obtained as dark red powder (72.2 mg, 65 %). MS (ESI+): m/z [M+H]+ calculated for $C_{36}H_{19}BF_{18}N_2O_2S$: 897.105, found: 897.106; MS (ESI-): m/z [M-H]- calculated for $C_{26}H_{27}BF_6N_2O_2S$: 895.090, found: 895.091

8-((4-((2-((*tert*-butoxycarbonyl)amino)ethyl)thio)-2,3,5,6-Pentafluorophenyl)-3,5-bis-(3,5-bis(trifluoromethyl)phenyl)-1,7-dimethyl-4,4-difluoro-4-bora-3a,4a-diaza-*s*-indacene (13(Precursor)): The **13** precursor was prepared with boc-cysteinamine as thiol compound. It was obtained as orange-red powder (61 mg, 86 %) MS (ESI+): m/z [M+H]+ calculated for $C_{30}H_{36}BF_6N_3O_2S$: 628.260, found: 628.261

8-((4-((2-aminoethyl)thio)-2,3,5,6-Pentafluorophenyl)-3,5-bis-(4-(trifluoromethyl)phenyl)-1,7-dimethyl-4,4-difluoro-4-bora-3a,4a-diaza-*s*-indacene (13): **13** was obtained after treating the precursor with diluted TFA for 4 h in CH_2Cl_2 and purification of the final product by aqueous extraction against $NaHCO_3$ solution. The purity was checked using TLC and NMR. ^{1}H NMR (400 MHz, $CDCl_3$): δ (ppm) = 3.30 (dd, J = 11.8, 6.0 Hz, 2H, CH_2), 3.12 (t, J = 6.3 Hz, 2H, CH_2), 2.54 (s, 6H, 2 CH_3), 2.3 (q, J = 7.6 Hz, 4H, 2 CH_2), 1.5 (s, 6H, 2 CH_3), 1.01 (t, J = 7.6 Hz, 6H, 2 CH_3)

5.6 Surface treatments

The initial and the final protocols are given, amendments to these procedures are comprehensibly mentioned in the according results section.

5.6.1 Silane depositions

5.6.1.1 Dip-coating of silanes

Commercial glass slides were activated with freshly prepared piranha solution (conc. H_2SO_4 : H_2O_2 3:1 v/v) for 2 h, washed thoroughly with MilliQ water and stored under water, no longer than one week prior to use. They were dried by centrifugation prior to usage. A solution of 5 % silane in EtOH with 1 % acetic acid was prepared and left for 30 min. The cleaned and dried slides were dipped in the solution and carefully rinsed with EtOH to produce a self-assembled layer of silane on the surface. The slides with adsorbed silane were cured for two hours at 120 °C. and carefully rinsed afterwards.

5.6.1.2 Initial procedure for silane vapour deposition

Commercial glass slides were activated with freshly prepared piranha solution (conc. H_2SO_4 : H_2O_2 3:1 v/v) for 2 h, washed thoroughly with MilliQ water and stored under water, no longer than one week prior to use. 100 µl of 10 % (v/v) APTES in dry toluene were added into a 100 mL glass bottle under protecting gas and two activated and carefully dried glass slides were placed in the bottle, which was heated for 2 h at 150 °C. The slides were removed from the bottle and rinsed with acetone and IPA, followed by sonication in IPA, rinsing with IPA and H_2O followed by drying with a slide centrifuge.

5.6.1.3 Optimized procedure for silane vapour deposition

The substrates (glass or silicon) were cleaned by ultra-sonication at 80 kHz in a detergent solution, followed by ultra-sonication in Hellmanex II solution, both for 15 min, and sonication in MilliQ water twice for 5 min. The slides were rinsed thoroughly with MilliQ water after each sonication step and finally dried by centrifugation. Activation was performed directly after cleaning using a low pressure air plasma for 10 min. To remove physisorbed water and minimize organic contaminations, the slides were then dried *in vacuo* (<0.1 mbar) overnight. The silane solutions (10 % (v/v) organosilane in dry toluene) were prepared under inert atmosphere in an argon filled glove pyramid. For the mixed silane solutions, an amino silane solution was diluted stepwise by adding aliquots of inert silane solution, resulting ratios are given in text for functional silane relative to the total silane content). 50 µL of each silane solution were

transferred into small open vessels inside 100 mL glass bottles under an inert atmosphere, the bottles having been cleaned with 1 M potassium hydroxide in water for 24 h and dried at 150 °C prior to use. Two dried slides were placed inside of the bottle which was carefully closed with a polytetrafluoroethylene (PTFE)-sealed PPS-lid before being transferred into an oven pre-heated to 150 °C. After 4 h at this temperature, the bottles were opened under a stream of argon, directly subjected to vacuum (<0.1 mbar) and left to cool down to room temperature (1.5 h). After removal from vacuum, the slides were rinsed with acetone, iso-propanol and water, followed by drying in a centrifuge and cleaning in a Soxhlet extractor with acetone overnight. After further rinsing with acetone, iso-propanol and water and subsequent drying in a centrifuge, the slides were stored at −18 °C under protective atmosphere.

5.6.2 Dye treatments

5.6.2.1 Initial procedure for labelling with 1

The washed and dried slides were placed in 25 mL of a 0.2 mM solution of **1** in MeCN in a 50 mL centrifuge tube and incubated overnight under stirring at room temperature. The slides were subsequently washed in the manner as after the functionalization (vide supra). The functionalized and incubated slides were stored under argon and removed from the protecting atmosphere just prior to the measurements.

5.6.2.2 Procedure for labelling of surfaces with 2 and 3

The slides were treated as described as described above for **1**, only with the addition of a few µg of K_2CO_3.

5.6.2.3 Optimized surface labelling with 1

For liquid phase reaction with **1**, the surface-modified substrates were placed in a 0.2 mM solution of **1** in MeCN for 24 h under stirring and were cleaned afterwards in a Soxhlet extractor with acetone for 24 h after rinsing with acetone, IPA and water. Rinsing has to occur immediately after retracting the slides form the dye solution, before the latter dries on the surface. After the Soxhlet cleaning, the samples are rinsed with acetone and IPA prior to drying with the Ar-Jet.

5.6.2.4 Surface labelling with RITC

For liquid phase reaction with RITC, the surface-modified substrates were placed in a 0.2 mM solution of RITC in 40 mM phosphate buffer for 4 h at room temperature under stirring, followed by rinsing with buffer, water, ethanol, IPA and acetone and concluded by cleaning with acetone in a Soxhlet extractor for 24 h. After the Soxhlet cleaning, the samples are rinsed with acetone and IPA prior to drying with the Ar-Jet.

5.6.2.5 Surface labelling with 10, 11 or 12

To a 0.2 mM solution of **10**, **11** or **12** in MeCN, DIC was added, followed by NHS. The surface-modified substrates were subsequently added and left in the solution for 24 h under stirring and were cleaned afterwards in a Soxhlet extractor with acetone for 24 h after rinsing with acetone, IPA and water. Rinsing has to occur immediately after retracting the slides form the dye solution, before the latter dries on the surface. After the Soxhlet cleaning, the samples are rinsed with acetone and IPA prior to drying with the Ar-Jet.

5.6.2.6 Surface labelling with 13

For liquid phase reaction with the **13**, the surface-modified substrates were placed in a 0.2 mM solution of **13** in MeCN for 24 h under stirring and were cleaned afterwards in a Soxhlet extractor with acetone for 24 h after rinsing with acetone, IPA and water. Rinsing has to occur immediately after retracting the slides form the dye solution, before the latter dries on the surface. After the Soxhlet cleaning, the samples are rinsed with acetone and IPA prior to drying with the Ar-Jet.

5.6.2.7 Preparation of Coumarin 153 test sample

A quartz slide was carefully cleaned as described above, including polishing with a lint-free tissue to achieve maximum transparency. A clean cotton stick was dipped in a 1.5 M solution of Coumarin 153 in EtOH (spec.) and wiped across the slide in one move to provide an even stripe of dye upon drying. Three stripes were placed in that manner.

Bibliography

[1] Watson, J. *Science* **1990**, *248*, 44–49.

[2] Cantor, C. *Science* **1990**, *248*, 49–51.

[3] Collins, F. S. *Science* **2003**, *300*, 286–290.

[4] Sanger, F.; Coulson, A. *Journal of Molecular Biology* **1975**, *94*, 441–448.

[5] Sanger, F.; Nicklen, S.; Coulson, a. R. *Proceedings of the National Academy of Sciences* **1977**, *74*, 5463–5467.

[6] Pettersson, E.; Lundeberg, J.; Ahmadian, A. *Genomics* **2009**, *93*, 105–111.

[7] Shalon, D.; Smith, S. J.; Brown, P. O. *Genome Research* **1996**, *6*, 639–645.

[8] Pease, a. C.; Solas, D.; Sullivan, E. J.; Cronin, M. T.; Holmes, C. P.; Fodor, S. P. *Proceedings of the National Academy of Sciences* **1994**, *91*, 5022–5026.

[9] Nuwaysir, E. F. *Genome Research* **2002**, *12*, 1749–1755.

[10] Mardis, E. R. *Annual Review of Genomics and Human Genetics* **2008**, *9*, 387–402.

[11] Cho, C. R.; Labow, M.; Reinhardt, M.; van Oostrum, J.; Peitsch, M. C. *Current Opinion in Chemical Biology* **2006**, *10*, 294–302.

[12] Ricke, D. O.; Wang, S.; Cai, R.; Cohen, D. *Current Opinion in Chemical Biology* **2006**, *10*, 303–308.

[13] Hoheisel, J. D. *Nature Reviews Microbiology* **2006**, *7*, 200–210.

[14] Berrade, L.; Garcia, A. E.; Camarero, J. A. *Pharmaceutical Research* **2011**, *28*, 1480–1499.

[15] Walter, J. G.; Kökpinar, Ö.; Friehs, K.; Stahl, F.; Scheper, T. *Analytical Chemistry* **2008**, *80*, 7372–7378.

[16] Jonkheijm, P.; Weinrich, D.; Schröder, H.; Niemeyer, C. M.; Waldmann, H. *Angewandte Chemie (International ed. in English)* **2008**, *47*, 9618–9647.

[17] Kusnezow, W.; Banzon, V.; Schröder, C.; Schaal, R.; Hoheisel, J. D.; Rüffer, S.; Luft, P.; Duschl, A.; Syagailo, Y. V. *Proteomics* **2007**, *7*, 1786–1799.

[18] Alhamdani, M. S.; Schröder, C.; Hoheisel, J. D. *Genome Medicine* **2009**, *1*, 68.

[19] Chaga, G. S. *Methods in Molecular Biology* **2008**, *441*, 129–151.

[20] Rivas, L. a.; García-Villadangos, M.; Moreno-Paz, M.; Cruz-Gil, P.; Gómez-Elvira, J.; Parro, V. *Analytical Chemistry* **2008**, *80*, 7970–7979.

[21] Matsumoto, E.; Yamauchi, T.; Fukuda, T.; Miura, Y. *Science and Technology of Advanced Materials* **2009**, *10*, 034605.

[22] Uttamchandani, M.; Walsh, D. P.; Yao, S. Q.; Chang, Y.-T. *Current Opinion in Chemical Biology* **2005**, *9*, 4–13.

[23] Hoever, M.; Zbinden, P. *Drug Discovery Today* **2004**, *9*, 358–365.

[24] Ma, H.; Horiuchi, K. Y. *Drug Discovery Today* **2006**, *11*, 661–668.

[25] Chen, D.; Davis, M. *Current Opinion in Chemical Biology* **2006**, *10*, 28–34.

[26] Seidel, M.; Niessner, R. *Analytical and bioanalytical chemistry* **2008**, *391*, 1521–44.

[27] Guo, Z.; Guilfoyle, R. A.; Thiel, A. J.; Wang, R.; Smith, L. M. *Nucleic Acids Research* **1994**, *22*, 5456–5465.

[28] Southern, E.; Mir, K.; Shchepinov, M. *Nature Genetics* **1999**, *21*, 5–9.

[29] Guilleaume, B.; Buness, A.; Schmidt, C.; Klimek, F.; Moldenhauer, G.; Huber, W.; Arlt, D.; Korf, U.; Wiemann, S.; Poustka, A. *Proteomics* **2005**, *5*, 4705–12.

[30] Zammatteo, N.; Jeanmart, L.; Hamels, S.; Courtois, S.; Louette, P.; Hevesi, L.; Remacle, J. *Analytical Biochemistry* **2000**, *280*, 143–150.

[31] Beier, M.; Hoheisel, J. D. *Nucleic Acids Research* **1999**, *27*, 1970–1977.

[32] del Campo, A.; Bruce, I. *Topics in Current Chemistry* **2005**, *260*, 77–111.

[33] Bhatia, S. K.; Shriver-Lake, L. C.; Prior, K. J.; Georger, J. H.; Calvert, J. M.; Bredehorst, R.; Ligler, F. S. *Analytical Biochemistry* **1989**, *178*, 408–413.

[34] Shircliff, R. a.; Stradins, P.; Moutinho, H.; Fennell, J.; Ghirardi, M. L.; Cowley, S. W.; Branz, H. M.; Martin, I. T. *Langmuir* **2013**, *29*, 4057–67.

[35] Peterson, A. W. *Nucleic Acids Research* **2001**, *29*, 5163–5168.

[36] Peterson, A. W.; Wolf, L. K.; Georgiadis, R. M. *Journal of the American Chemical Society* **2002**, *124*, 14601–14607.

[37] Arima, Y.; Iwata, H. *Biomaterials* **2007**, *28*, 3074–3082.

[38] Balboni, I.; Limb, C.; Tenenbaum, J. D.; Utz, P. J. *Proteomics* **2008**, *8*, 3443–3449.

[39] Lee, J. H.; Jung, H. W.; Kang, I. K.; Lee, H. B. *Biomaterials* **1994**, *15*, 705–711.

[40] Lee, J. H.; Lee, J. W.; Khang, G.; Lee, H. B. *Biomaterials* **1997**, *18*, 351–358.

[41] Hennig, A.; Borcherding, H.; Jaeger, C.; Hatami, S.; Würth, C.; Hoffmann, A.; Hoffmann, K.; Thiele, T.; Schedler, U.; Resch-Genger, U. *Journal of the American Chemical Society* **2012**, *134*, 8268–76.

[42] Kallury, K. M. R.; Macdonald, P. M.; Thompson, M. *Langmuir* **1994**, *10*, 492–499.

[43] Zhu, S.; Panne, U.; Rurack, K. *The Analyst* **2013**, *138*, 2924–2930.

[44] Shard, A. G. *Surface and Interface Analysis* **2014**, *46*, 175–185.

[45] Seah, M. P. *et al. Surface and Interface Analysis* **2004**, *36*, 1269–1303.

[46] Smith, G. C. *Journal of Electron Spectroscopy and Related Phenomena* **2005**, *148*, 21–28.

[47] Ray, S.; Shard, A. G. *Analytical chemistry* **2011**, *83*, 8659–66.

[48] Kallury, K. M. R.; Brennan, J. D.; Krull, U. J. *Analytical Chemistry* **1995**, *67*, 2625–2634.

[49] Batich, C. D. *Applied Surface Science* **1988**, *32*, 57–73.

[50] Gross, T.; Pippig, F.; Merz, B.; Merz, R.; Vohrer, U.; Mix, R.; Steffen, H.; Bremser, W.; Unger, W. E. S. *Plasma Processes and Polymers* **2010**, *7*, 494–503.

[51] Holländer, A. *Surface and Interface Analysis* **2004**, *36*, 1023–1026.

[52] Holländer, A.; Kröpke, S.; Pippig, F. *Surface and Interface Analysis* **2008**, *40*, 379–385.

[53] Holländer, A.; Pippig, F.; Dubreuil, M.; Vangeneugden, D. *Plasma Processes and Polymers* **2008**, *5*, 345–349.

[54] Yegen, E.; Zimmermann, U.; Unger, W. E. S.; Braun, T. *Plasma Processes and Polymers* **2009**, *6*, 11–16.

[55] Fally, F.; Doneux, C.; Riga, J.; Verbist, J. J. *Journal of Applied Polymer Science* **1995**, *56*, 597–614.

[56] Yegen, E.; Lippitz, A.; Treu, D.; Unger, W. E. S. *Surface and Interface Analysis* **2008**, *40*, 176–179.

[57] Boulares-Pender, A.; Prager-Duschke, A.; Elsner, C.; Buchmeiser, M. R. *Journal of Applied Polymer Science* **2009**, *112*, 2701–2709.

[58] Girard-Lauriault, P.-L.; Ruiz, J.-C.; Gross, T.; Wertheimer, M. R.; Unger, W. E. S. *Plasma Chemistry and Plasma Processing* **2011**, *31*, 535–550.

[59] Girard-Lauriault, P.-L.; Desjardins, P.; Unger, W. E. S.; Lippitz, A.; Wertheimer, M. R. *Plasma Processes and Polymers* **2008**, *5*, 631–644.

[60] Girard-Lauriault, P.-L.; Gross, T.; Lippitz, A.; Unger, W. E. S. *Analytical Chemistry* **2012**, *84*, 5984–5991.

[61] Graf, N.; Lippitz, A.; Gross, T.; Pippig, F.; Holländer, A.; Unger, W. E. S. *Analytical and Bioanalytical Chemistry* **2010**, *396*, 725–738.

[62] Pippig, F.; Sarghini, S.; Holländer, A.; Paulussen, S.; Terryn, H. *Surface and Interface Analysis* **2009**, *41*, 421–429.

[63] Becer, C. R.; Hoogenboom, R.; Schubert, U. S. *Angewandte Chemie International Edition* **2009**, *48*, 4900–4908.

[64] Ivanov, V. B.; Behnisch, J.; Holländer, A.; Mehdorn, F.; Zimmermann, H. *Surface and Interface Analysis* **1996**, *24*, 257–262.

[65] Fischer, T.; Dietrich, P. M.; Streeck, C.; Ray, S.; Nutsch, A.; Shard, A. G.; Beckhoff, B.; Unger, W. E. S.; Rurack, K. *Analytical Chemistry* **2015**, *87*, 2685–2692.

[66] B\"{o}hmler, J.; Ploux, L.; Ball, V.; Anselme, K.; Ponche, A. *The Journal of Physical Chemistry C* **2011**, *115*, 11102–11111.

[67] Awsiuk, K.; Bernasik, A.; Kitsara, M.; Budkowski, A.; Rysz, J.; Haberko, J.; Petrou, P.; Beltsios, K.; Raczkowska, J. *Colloids and Surfaces, B: Biointerfaces* **2010**, *80*, 63–71.

[68] Bramblett, A. L.; S. Boeckl, M.; Hauch, K. D.; Ratner, B. D.; Sasaki, T.; Rogers, J. W. *Surface and Interface Analysis* **2002**, *33*, 506–515.

[69] Frydman, E.; Cohen, H.; Maoz, R.; Sagiv, J. *Langmuir* **1997**, *13*, 5089–5106.

[70] Kallury, K. M. R.; Krull, U. J.; Thompson, M. *Analytical Chemistry* **1988**, *60*, 169–172.

[71] Kallury, K. M. R.; Cheung, M.; Ghaemmaghami, V.; Krull, U. J.; Thompson, M. *Colloids and Surfaces* **1992**, *63*, 1–9.

[72] Min, H.; Girard-Lauriault, P.-L.; Gross, T.; Lippitz, A.; Dietrich, P. M.; Unger, W. E. S. *Analytical and bioanalytical chemistry* **2012**, *403*, 613–23.

[73] Wayment, J. R.; Harris, J. M. *Analytical chemistry* **2006**, *78*, 7841–9.

[74] Abbas, A.; Vivien, C.; Bocquet, B.; Guillochon, D.; Supiot, P. *Plasma Processes and Polymers* **2009**, *6*, 593–604.

[75] Hoffmann, K.; Mix, R.; Resch-Genger, U.; Friedrich, J. F. *Langmuir* **2007**, *23*, 8411–8416.

[76] Kamisetty, N. K.; Pack, S. P.; Nonogawa, M.; Devarayapalli, K. C.; Kodaki, T.; Makino, K. *Analytical and bioanalytical chemistry* **2006**, *386*, 1649–55.

[77] Chiu, S.-K.; Hsu, M.; Ku, W.-C.; Tu, C.-Y.; Tseng, Y.-T.; Lau, W.-K.; Yan, R.-Y.; Ma, J.-T.; Tzeng, C.-M. *Biochemical Journal* **2003**, *374*, 625–632.

[78] Wang, W.; Vaughn, M. W. *Scanning* **2008**, *30*, 65–77.

[79] Pippig, F.; Holländer, A. *Applied Surface Science* **2007**, *253*, 6817–6823.

[80] Funk, C.; Dietrich, P. M.; Gross, T.; Min, H.; Unger, W. E. S.; Weigel, W. *Surface and Interface Analysis* **2011**, n/a–n/a.

[81] Wang, Y.; Lowe, R. D.; Mejia, Y. X.; Feindt, H.; Steltenkamp, S.; Burg, T. P. *Biomicrofluidics* **2013**, *7*, 026503.

[82] Shlyapnikova, E. a.; Shlyapnikov, Y. M.; Afanas'ev, V. N.; Afanas'eva, G. V.; Gavryushkin, A. V.; Beletskii, I. P. *Russian Journal of Bioorganic Chemistry* **2007**, *33*, 243–250.

[83] Noel, S.; Liberelle, B.; Robitaille, L.; De Crescenzo, G. *Bioconjugate chemistry* **2011**, *22*, 1690–1699.

[84] Cavanagh, R.; Heilweil, E.; Stephenson, J. *Surface Science* **1994**, *299-300*, 643–655.

[85] Rae, M.; Fedorov, A.; Berberan-Santos, M. N. *The Journal of Chemical Physics* **2003**, *119*, 2223–2231.

[86] Xing, Y.; Borguet, E. *Langmuir* **2007**, *23*, 684–688.

[87] Xing, Y.; Dementev, N.; Borguet, E. *Current Opinion in Solid State and Materials Science* **2007**, *11*, 86–91.

[88] Hecht, M.; Fischer, T.; Dietrich, P. M.; Kraus, W.; Descalzo, A. B.; Unger, W. E. S.; Rurack, K. *ChemistryOpen* **2013**, *2*, 25–38.

[89] Batz, N. G.; Mellors, J. S.; Alarie, J. P.; Ramsey, J. M. *Analytical Chemistry* **2014**, *86*, 3493–3500.

[90] Salmio, H.; Brühwiler, D. *The Journal of Physical Chemistry C* **2007**, *111*, 923–929.

[91] Zhang, F.; Sautter, K.; Larsen, A. M.; Findley, D. A.; Davis, R. C.; Samha, H.; Linford, M. R. *Langmuir* **2010**, *26*, 14648–14654.

[92] Stein, S.; Böhlen, P.; Udenfriend, S. *Archives of Biochemistry and Biophysics* **1974**, *163*, 400–403.

[93] Moon, J. H.; Shin, J. W.; Kim, S. Y.; Park, J. W. *Langmuir* **1996**, *12*, 4621–4624.

[94] Moon, J. H.; Kim, J. H.; Kim, K.-j.; Kang, T.-H.; Kim, B.; Kim, C.-H.; Hahn, J. H.; Park, J. W. *Langmuir* **1997**, *13*, 4305–4310.

[95] Xiang, S.; Xing, G.; Xue, W.; Lu, C.; Lin, J.-M. *The Analyst* **2012**, *137*, 1669–1673.

[96] Sugimura, H.; Moriguchi, T.; Kanda, M.; Sonobayashi, Y.; Nishimura, H. M.; Ichii, T.; Murase, K.; Kazama, S. *Chemical communications (Cambridge, England)* **2011**, *47*, 8841–3.

[97] Kim, J.; Shon, H. K.; Jung, D.; Moon, D. W.; Han, S. Y.; Lee, T. G. *Analytical chemistry* **2005**, *77*, 4137–4141.

[98] Durfor, C. N.; Turner, D. C.; Georger, J. H.; Peek, B. M.; Stenger, D. a. *Langmuir* **1994**, *10*, 148–152.

[99] Flink, S.; van Veggel, F. C. J. M.; Reinhoudt, D. N. *Journal of Physical Organic Chemistry* **2001**, *14*, 407–415.

[100] Gaur, R.; Gupta, K. *Analytical Biochemistry* **1989**, *180*, 253–258.

[101] Coussot, G.; Perrin, C.; Moreau, T.; Dobrijevic, M.; Le Postollec, A.; Vandenabeele-Trambouze, O. *Analytical and bioanalytical chemistry* **2011**, *399*, 1061–1069.

[102] Ghasemi, M.; Minier, M.; Tatoulian, M.; Arefi-Khonsari, F. *Langmuir* **2007**, *23*, 11554–11561.

[103] Fiorilli, S.; Rivolo, P.; Descrovi, E.; Ricciardi, C.; Pasquardini, L.; Lunelli, L.; Vanzetti, L.; Pederzolli, C.; Onida, B.; Garrone, E. *Journal of Colloid and Interface Science* **2008**, *321*, 235–241.

[104] Shard, A. G.; Ray, S.; Seah, M. P.; Yang, L. *Surface and Interface Analysis* **2011**, *43*, 1240–1250.

[105] Shard, A. G.; Spencer, S. J.; Smith, S. a.; Havelund, R.; Gilmore, I. S. *International Journal of Mass Spectrometry* **2015**, *377*, 599–609.

[106] Oran, U.; Swaraj, S.; Lippitz, A.; Unger, W. E. S. *Plasma Processes and Polymers* **2006**, *3*, 288–298.

[107] Médard, N.; Aouinti, M.; Poncin-Epaillard, F.; Bertrand, P. *Surface and Interface Analysis* **2001**, *31*, 1042–1047.

[108] Sun, W.-C.; Gee, K. R.; Klaubert, D. H.; Haugland, R. P. *The Journal of Organic Chemistry* **1997**, *62*, 6469–6475.

[109] Funabiki, K.; Sugiyama, N.; Iida, H.; Jin, J.-Y.; Yoshida, T.; Kato, Y.; Minoura, H.; Matsui, M. *Journal of Fluorine Chemistry* **2006**, *127*, 257–262.

[110] Mitronova, G. Y.; Belov, V. N.; Bossi, M. L.; Wurm, C. A.; Meyer, L.; Medda, R.; Moneron, G.; Bretschneider, S.; Eggeling, C.; Jakobs, S.; Hell, S. W. *Chemistry - A European Journal* **2010**, *16*, 4477–4488.

[111] Woydziak, Z. R.; Fu, L.; Peterson, B. R. *The Journal of Organic Chemistry* **2012**, *77*, 473–481.

[112] Martin, M. M.; Lindqvist, L. *Journal of Luminescence* **1975**, *10*, 381–390.

[113] Beija, M.; Afonso, C. a. M.; Martinho, J. M. G. *Chemical Society Reviews* **2009**, *38*, 2410–2433.

[114] Kölmel, D. K.; Rudat, B.; Braun, D. M.; Bednarek, C.; Schepers, U.; Bräse, S. *Organic & Biomolecular Chemistry* **2013**, *11*, 3954–3962.

[115] Ulrich, G.; Ziessel, R.; Harriman, A. *Angewandte Chemie (International ed. in English)* **2008**, *47*, 1184–1201.

[116] Loudet, A.; Burgess, K. *Chemical Reviews* **2007**, *107*, 4891–932.

[117] Vives, G.; Giansante, C.; Bofinger, R.; Raffy, G.; Guerzo, A. D.; Kauffmann, B.; Batat, P.; Jonusauskas, G.; McClenaghan, N. D. *Chemical communications (Cambridge, England)* **2011**, 10425–10427.

[118] Alamiry, M. A. H.; Benniston, A. C.; Hagon, J.; Winstanley, T. P. L.; Lemmetyinen, H.; Tkachenko, N. V. *RSC Advances* **2012**, *2*, 4944–4950.

[119] Galangau, O.; Dumas-Verdes, C.; Méallet-Renault, R.; Clavier, G. *Organic & biomolecular chemistry* **2010**, *8*, 4546–4553.

[120] Rurack, K.; Descalzo, A. B.; Fischer, T.; Behnke, T. **2011**, DE102009028982.

[121] Rurack, K.; Descalzo, A. B.; Fischer, T.; Behnke, T. **2011**, EP2302002.

[122] Rurack, K.; Descalzo, A. B.; Fischer, T.; Behnke, T. **2011**, US20110054187.

[123] Qin, W.; Leen, V.; Rohand, T.; Dehaen, W.; Dedecker, P.; Van der Auweraer, M.; Robeyns, K.; Van Meervelt, L.; Beljonne, D.; Van Averbeke, B.; Clifford, J. N.; Driesen, K.; Binnemans, K.; Boens, N. *The Journal of Physical Chemistry A* **2009**, *113*, 439–447.

[124] Qin, W.; Leen, V.; Dehaen, W.; Cui, J.; Xu, C.; Tang, X.; Liu, W.; Rohand, T.; Beljonne, D.; Averbeke, B. V.; Clifford, J. N.; Driesen, K.; Binnemans, K.; Auweraer, M. V. D.; Boens, N. *The Journal of Physical Chemistry C* **2009**, *113*, 11731–11740.

[125] Lempke, L.; Fischer, T.; Bell, J.; Kraus, W.; Rurack, K.; Krause, N. *Organic & Biomolecular Chemistry* **2015**, *13*, 3787–3791.

[126] Kollmannsberger, M.; Rurack, K.; Resch-Genger, U.; Daub, J. *The Journal of Physical Chemistry A* **1998**, *102*, 10211–10220.

[127] Trieflinger, C.; Röhr, H.; Rurack, K.; Daub, J. *Angewandte Chemie (International ed. in English)* **2005**, *44*, 6943–6947.

[128] Wang, Y.-W.; Descalzo, A. B.; Shen, Z.; You, X.-Z.; Rurack, K. *Chemistry - A European Journal* **2010**, *16*, 2887–2903.

[129] Olah, G. a.; Berrier, A. L.; Arvanaghi, M.; Prakash, G. K. S. *Journal of the American Chemical Society* **1981**, *103*, 1122–1128.

[130] Yu, Y.-H.; Descalzo, A. B.; Shen, Z.; Röhr, H.; Liu, Q.; Wang, Y.-W.; Spieles, M.; Li, Y.-Z.; Rurack, K.; You, X.-Z. *Chemistry - An Asian Journal* **2006**, *1*, 176–187.

[131] Rurack, K.; Kollmannsberger, M.; Daub, J. *New Journal of Chemistry* **2001**, *25*, 289–292.

[132] Rohand, T.; Lycoops, J.; Smout, S.; Braeken, E.; Sliwa, M.; Van der Auweraer, M.; Dehaen, W.; De Borggraeve, W. M.; Boens, N. *Photochemical & photobiological sciences : Official journal of the European Photochemistry Association and the European Society for Photobiology* **2007**, *6*, 1061–1066.

[133] Bozdemir, O. A.; Guliyev, R.; Buyukcakir, O.; Selcuk, S.; Kolemen, S.; Gulseren, G.; Nalbantoglu, T.; Boyaci, H.; Akkaya, E. U. *Journal of the American Chemical Society* **2010**, *132*, 8029–8036.

[134] Rohand, T.; Baruah, M.; Qin, W.; Boens, N.; Dehaen, W. *Chemical communications (Cambridge, England)* **2006**, 266–268.

[135] Zhu, M.; Lerum, M. Z.; Chen, W. *Langmuir* **2012**, *28*, 416–423.

[136] Everhart, D. S.; Reilley, C. N. *Analytical Chemistry* **1981**, *53*, 665–676.

[137] Graf, N.; Yegen, E.; Gross, T.; Lippitz, A.; Weigel, W.; Krakert, S.; Terfort, A.; Unger, W. E. *Surface Science* **2009**, *603*, 2849–2860.

[138] Graf, N.; Yegen, E.; Lippitz, A.; Treu, D.; Wirth, T.; Unger, W. E. S. *Surface and Interface Analysis* **2008**, *40*, 180–183.

[139] Girard-Lauriault, P.-L.; Dietrich, P. M.; Gross, T.; Unger, W. E. S. *Surface and Interface Analysis* **2012**, *44*, 1135–1140.

[140] Song, X.; Ma, Y.; Wang, C.; Dietrich, P. M.; Unger, W. E. S.; Luo, Y. *The Journal of Physical Chemistry C* **2012**, *116*, 12649–12654.

[141] Sugimura, H.; Moriguchi, T.; Kanda, M.; Sonobayashi, Y.; Nishimura, H. M.; Ichii, T.; Murase, K.; Kazama, S. *Chemical Communications* **2011**, *47*, 8841–8843.

[142] Imhof, A.; Megens, M.; Engelberts, J. J.; de Lang, D. T. N.; Sprik, R.; Vos, W. L. *The Journal of Physical Chemistry B* **1999**, *103*, 1408–1415.

[143] Aissaoui, N.; Bergaoui, L.; Landoulsi, J.; Lambert, J.-F.; Boujday, S. *Langmuir* **2012**, *28*, 656–65.

[144] Smith, E. A.; Chen, W. *Langmuir* **2008**, *24*, 12405–9.

[145] Chechik, V.; Crooks, R. M.; Stirling, C. J. M. *Advanced Materials* **2000**, *12*, 1161–1171.

[146] Love, J. C.; Estroff, L. A.; Kriebel, J. K.; Nuzzo, R. G.; Whitesides, G. M. *Chemical Reviews* **2005**, *105*, 1103–1170.

[147] Du, H.; Disney, M. D.; Miller, B. L.; Krauss, T. D. *Journal of the American Chemical Society* **2003**, *125*, 4012–4013.

[148] Choukourov, A.; Biederman, H.; Kholodkov, I.; Slavinska, D.; Trchova, M.; Holländer, A. *Journal of Applied Polymer Science* **2004**, *92*, 979–990.

[149] Truica-Marasescu, F.; Girard-Lauriault, P.-L.; Lippitz, A.; Unger, W. E. S.; Wertheimer, M. R. *Thin Solid Films* **2008**, *516*, 7406–7417.

[150] White, L.; Tripp, C. P. *Journal of Colloid and Interface Science* **2000**, *232*, 400–407.

[151] Zhuravlev, L. T. *Langmuir* **1987**, *3*, 316–318.

[152] Shircliff, R. a.; Martin, I. T.; Pankow, J. W.; Fennell, J.; Stradins, P.; Ghirardi, M. L.; Cowley, S. W.; Branz, H. M. *ACS applied materials & interfaces* **2011**, *3*, 3285–92.

[153] Fadeev, A. Y.; McCarthy, T. J. *Langmuir* **1999**, *15*, 7238–7243.

[154] Maidenberg, Y.; Zhang, S.; Luo, K.; Akhavein, N.; Koberstein, J. T. *Langmuir* **2013**, *29*, 11959–11965.

[155] Martin, P.; Marsaudon, S.; Thomas, L.; Desbat, B.; Aimé, J.-P.; Bennetau, B. *Langmuir* **2005**, *21*, 6934–43.

[156] Tong, Y.; Tyrode, E.; Osawa, M.; Yoshida, N.; Watanabe, T.; Nakajima, A.; Ye, S. *Langmuir* **2011**, *27*, 5420–5426.

[157] Vuori, L.; Hannula, M.; Lahtonen, K.; Jussila, P.; Ali-Löytty, H.; Hirsimäki, M.; Pärna, R.; Nõmmiste, E.; Valden, M. *Applied Surface Science* **2014**, *317*, 856–866.

[158] Tripp, C. P.; Hair, M. L. *The Journal of Physical Chemistry* **1993**, *97*, 5693–5698.

[159] Lee, I.; Wool, R. P. *Thin Solid Films* **2000**, *379*, 94–100.

[160] Strobel, M.; Lyons, C. S. *Plasma Processes and Polymers* **2011**, *8*, 8–13.

[161] Kwok, D.; Neumann, A. *Advances in Colloid and Interface Science*; 1999; Vol. 81; pp 167–249.

[162] Janssen, D.; De Palma, R.; Verlaak, S.; Heremans, P.; Dehaen, W. *Thin Solid Films* **2006**, *515*, 1433–1438.

[163] Lam, C. N. C.; Wu, R.; Li, D.; Hair, M. L.; Neumann, a. W. *Advances in colloid and interface science* **2002**, *96*, 169–191.

[164] Lam, C.; Kim, N.; Hui, D.; Kwok, D.; Hair, M.; a.W. Neumann, *Colloids and Surfaces A: Physicochemical and Engineering Aspects* **2001**, *189*, 265–278.

[165] Korhonen, J. T.; Huhtamäki, T.; Ikkala, O.; Ras, R. H. A. *Langmuir* **2013**, *29*, 3858–3863.

[166] Kallury, K. M. R.; Thompson, M.; Tripp, C. P.; Hair, M. L. *Langmuir* **1992**, *8*, 947–954.

[167] Yang, S.-R.; Kolbesen, B. O. *Applied Surface Science* **2008**, *255*, 1726–1735.

[168] Grabar, K. C.; Freeman, R. G.; Hommer, M. B.; Natan, M. J. *Analytical Chemistry* **1995**, *67*, 735–743.

[169] Bras, M.; Dugas, V.; Bessueille, F.; Cloarec, J. P.; Martin, J. R.; Cabrera, M.; Chauvet, J. P.; Souteyrand, E.; Garrigues, M. *Biosensors and Bioelectronics* **2004**, *20*, 796–805.

[170] Kristensen, E. M. E.; Nederberg, F.; Rensmo, H.; Bowden, T.; Hilborn, J.; Siegbahn, H. *Langmuir* **2006**, *22*, 9651–9657.

[171] Piehler, J.; Brecht, A.; Valiokas, R.; Liedberg, B.; Gauglitz, G. *Biosensors & bioelectronics* **2000**, *15*, 473–81.

[172] Howarter, J. a.; Youngblood, J. P. *Langmuir* **2006**, *22*, 11142–7.

[173] Acres, R. G.; Ellis, A. V.; Alvino, J.; Lenahan, C. E.; Khodakov, D. a.; Metha, G. F.; Andersson, G. G. *The Journal of Physical Chemistry C* **2012**, *116*, 6289–6297.

[174] Yang, Z.; Chevolot, Y.; Géhin, T.; Dugas, V.; Xanthopoulos, N.; Laporte, V.; Delair, T.; Ataman-Önal, Y.; Choquet-Kastylevsky, G.; Souteyrand, E.; Laurenceau, E. *Langmuir* **2013**, *29*, 1498–1509.

[175] Mehne, J.; Markovic, G.; Pröll, F.; Schweizer, N.; Zorn, S.; Schreiber, F.; Gauglitz, G. *Analytical and bioanalytical chemistry* **2008**, *391*, 1783–91.

[176] Qin, M.; Hou, S.; Wang, L.; Feng, X.; Wang, R.; Yang, Y.; Wang, C.; Yu, L.; Shao, B.; Qiao, M. *Colloids and Surfaces, B: Biointerfaces* **2007**, *60*, 243–249.

[177] Lowe, R. D.; Pellow, M. a.; Stack, T. D. P.; Chidsey, C. E. D. *Langmuir* **2011**, *27*, 9928–35.

[178] Wang, Y.; Cai, J.; Rauscher, H.; Behm, R. J.; Goedel, W. a. *Chemistry (Weinheim an der Bergstrasse, Germany)* **2005**, *11*, 3968–78.

[179] Dorvel, B.; Reddy, B.; Block, I.; Mathias, P.; Clare, S. E.; Cunningham, B.; Bergstrom, D. E.; Bashir, R. *Advanced Functional Materials* **2010**, *20*, 87–95.

[180] Kim, J.; Seidler, P.; Wan, L. S.; Fill, C. *Journal of colloid and interface science* **2009**, *329*, 114–9.

[181] Cassie, A. B. D.; Baxter, S. *Transactions of the Faraday Society* **1944**, *40*, 546–551.

[182] Polster, D.; Graaf, H.; Baumgärtel, T.; von Borczyskowski, C.; Benedikt, U.; Auer, A. a. *Langmuir : the ACS journal of surfaces and colloids* **2010**, *26*, 8301–8.

[183] Grabar, K. C.; Allison, K. J.; Baker, B. E.; Bright, R. M.; Brown, K. R.; Freeman, R. G.; Fox, A. P.; Keating, C. D.; Musick, M. D.; Natan, M. J. *Langmuir* **1996**, *12*, 2353–2361.

[184] Brzoska, J. B.; Azouz, I. B.; Rondelez, F. *Langmuir* **1994**, *10*, 4367–4373.

[185] Alexander, M.; Short, R.; Jones, F.; Michaeli, W.; Blomfield, C. *Applied Surface Science* **1999**, *137*, 179–183.

[186] Smekal, W.; Werner, W. S. M.; Powell, C. J. *Surface and Interface Analysis* **2005**, *37*, 1059–1067.

[187] Brandstätter, M.; Fromherz, P.; Offenhäusser, A. *Thin Solid Films* **1988**, *160*, 341–346.

[188] *ISO 15472*; 2010.

[189] Cretich, M.; Reddington, A.; Monroe, M.; Bagnati, M.; Damin, F.; Sola, L.; Unlu, M. S.; Chiari, M. *Biosensors and Bioelectronics* **2011**, *26*, 3938–3943.

[190] Fischer, T.; Dietrich, P. M.; Unger, W. E. S.; Rurack, K. *Analytical Chemistry* **2016**, *88*, 1210–1217.

[191] Lee, M.; Kim, J.; Tang, J.; Hochstrasser, R. M. *Chemical Physics Letters* **2002**, *359*, 412–419.

[192] Lakowicz, J. R. In *Principles of fluorescence spectroscopy*, 3rd ed.; Lakowicz, J. R., Ed.; Springer New York, 2006.

[193] Chen, R. F.; Knutson, J. R. *Analytical Biochemistry* **1988**, *172*, 61–77.

[194] Linnros, J.; Lalic, N.; Galeckas, A.; Grivickas, V. *Journal of Applied Physics* **1999**, *86*, 6128–6134.

[195] Berberan-Santos, M. N.; Bodunov, E.; Valeur, B. *Chemical Physics* **2005**, *315*, 171–182.

[196] Berberan-Santos, M. N.; Valeur, B. *Journal of Luminescence* **2007**, *126*, 263–272.

[197] Valeur, B. *Molecular Fluorescence: Principles and Applications*; Wiley-VCH: Weinheim, FRG, 2001.

[198] Seah, M. P.; Spencer, S. J. *Journal of Vacuum Science & Technology A: Vacuum, Surfaces, and Films* **2003**, *21*, 345–350.

[199] Valeur, E.; Bradley, M. *Chemical Society reviews* **2009**, *38*, 606–31.

[200] O'Keefe, A.; Deacon, D. A. G. *Review of Scientific Instruments* **1988**, *59*, 2544–2551.

[201] Berden, G.; Peeters, R.; Meijer, G. *International Reviews in Physical Chemistry* **2000**, *19*, 565–607.

[202] Grand, Y. L.; Floch, A. L. *Applied Optics* **1990**, *29*, 1244–1246.

[203] van der Sneppen, L.; Wiskerke, a. E.; Ariese, F.; Gooijer, C.; Ubachs, W. *Applied Spectroscopy* **2006**, *60*, 931–935.

[204] Snyder, K. L.; Zare, R. N. *Analytical Chemistry* **2003**, *75*, 3086–3091.

[205] Schnippering, M.; Neil, S. R. T.; Mackenzie, S. R.; Unwin, P. R. *Chemical Society Reviews* **2011**, *40*, 207–220.

[206] Muir, R. N.; Alexander, A. J. *Physical Chemistry Chemical Physics* **2003**, *5*, 1279–1283.

[207] Kartouzian, A.; Thämer, M.; Heiz, U. *Physica Status Solidi B* **2010**, *247*, 1147–1151.

[208] Stelmaszczyk, K.; Fechner, M.; Rohwetter, P.; Queißer, M.; Czyzewski, A.; Stacewicz, T.; Wöste, L. *Applied Physics B* **2009**, *94*, 369–373.

[209] Stelmaszczyk, K.; Rohwetter, P.; Fechner, M.; Queißer, M.; Czyzewski, A.; Stacewicz, T.; Wöste, L. *Optics Express* **2009**, *17*, 3673–3678.

[210] Gross, T.; Lippitz, A.; Unger, W. E. S.; Güttler, B. *Surface and Interface Analysis* **2000**, *29*, 891–894.

[211] Rurack, K.; Spieles, M. *Analytical Chemistry* **2011**, *83*, 1232–1242.

[212] Brouwer, A. M. *Pure and Applied Chemistry* **2011**, *83*, 2213–2228.

List of Figures

List of Schemes

List of Tables

List of Slides

AA activated with piranha solution, Dip coated with APTES

AB activated with piranha solution, Dip coated with MPTMS

AC activated, VD with APTES (100 µL,10 % in Tol)

AC1 activated, VD with APTES (100 µL,10 % in Tol), labelled with **1**

AD activated with piranha solution

AD1 activated, labelled with **1**

AE activated, VD with APTES (50 µL,10 % in Tol)

AE1 activated, VD with APTES (50 µL,10 % in Tol), labelled with **1**

AF activated, VD with APTES (200 µL,10 % in Tol)

AF1 activated, VD with APTES (200 µL,10 % in Tol), labelled with **1**

AG activated, VD with APTES:CETES 3:1 (50 µL,10 % in Tol), labelled with **1**

AH activated, VD with APTES:CETES 1:1 (50 µL,10 % in Tol), labelled with **1**

AI activated, VD with APTES:CETES 1:3 (50 µL,10 % in Tol), labelled with **1**

AJ activated with NH_4OH(28 %):H_2O_2(30 %):H_2O 1:1:5

AK activated with HCl(28 %):H_2O_2(30 %):H_2O 1:1:5

AL activated with piranha solution

AM activated with 1 M KOH

AN activated with HCl:H_2O_2:H_2O, VD with APTES (50 µL,10 % in Tol, for 2 h)

AO activated, VD with APTES (50 µL,10 % in Tol, for 4 h)

AP activated ,VD with APTES (50 µL,10 % in Tol, for 24 h)

AQ activated, VD with APTES (50 µL,10 % in Tol, for 4 h), cleaned ultrasonically

AR activated, VD with APTES (50 µL,10 % in Tol, for 4 h), cleaned in MeCN over night

AR1 activated, VD with APTES (50 µL,10 % in Tol, for 4 h), cleaned in MeCN over night, treated with **1**

AS activated, VD with APTES (50 µL,10 % in Tol, for 4 h), cured *in vacuo* at 70 °C over night

AS1 activated, VD with APTES (50 µL,10 % in Tol, for 4 h), cured *in vacuo* at 70 °C over night, treated with **1**

AT activated, VD with APTES (50 µL,10 % in Tol, for 4 h)

AT1 activated, VD with APTES (50 µL,10 % in Tol, for 4 h), treated with **1**

AU activated, VD with AHAMTES (50 µL,10 % in Tol, for 4 h)

AU1 activated, VD with AHAMTES (50 µL,10 % in Tol, for 4 h), treated with **1**

AV activated, VD with APDIPES (50 µL,10 % in Tol, for 4 h)

AV1 activated, VD with APDIPES (50 µL,10 % in Tol, for 4 h), treated with **1**

AW activated, VD with PTMS (50 µL,10 % in Tol, for 4 h)

AW1 activated, VD with PTMS (50 µL,10 % in Tol, for 4 h), treated with **1**

AX activated, VD with APDIPES (50 µL,10 % in Tol)

AX1 activated, VD with APDIPES (50 µL,10 % in Tol), labelled with **1**

AY activated, VD with APDIPES:CETES 3:1 (50 µL,10 % in Tol)

AY1 activated, VD with APDIPES:CETES 3:1 (50 µL,10 % in Tol), labelled with **1**

AZ activated, VD with APDIPES:CETES 1:1 (50 µL,10 % in Tol)

AZ1 activated, VD with APDIPES:CETES 1:1 (50 µL,10 % in Tol), labelled with **1**

BA activated, VD with APDIPES:CETES 1:3 (50 µL,10 % in Tol)

BA1 activated, VD with APDIPES:CETES 1:3 (50 µL,10 % in Tol), labelled with **1**

BB activated, VD with CETES (50 µL,10 % in Tol)

BB1 activated, VD with CETES (50 µL,10 % in Tol), labelled with **1**

BC activated, VD with APTES (50 µL,10 % in Tol)

BC1 activated, VD with APTES (50 µL,10 % in Tol), labelled with **1**

BD activated, VD with APTES:PTMS 3:1 (50 µL,10 % in Tol)

BD1 activated, VD with APTES:PTMS 3:1 (50 µL,10 % in Tol), labelled with **1**

BE activated, VD with APTES:PTMS 1:1 (50 µL,10 % in Tol)

BE1 activated, VD with APTES:PTMS 1:1 (50 µL,10 % in Tol), labelled with **1**

BF activated, VD with APTES:PTMS 1:3 (50 µL,10 % in Tol)

BF1 activated, VD with APTES:PTMS 1:3 (50 µL,10 % in Tol), labelled with **1**

BG activated, VD with PTMS (50 µL,10 % in Tol)

BG1 activated, VD with PTMS (50 µL,10 % in Tol), labelled with **1**

BH activated, VD with APDIPES (50 µL,10 % in Tol)

BH1 activated, VD with APDIPES (50 µL,10 % in Tol), labelled with **1**

BI activated, VD with APDIPES:CPDMMS 2:3 (50 µL,10 % in Tol)

BI1 activated, VD with APDIPES:CPDMMS 2:3 (50 µL,10 % in Tol), labelled with **1**

BJ activated, VD with APDIPES:CPDMMS 2:13 (50 µL,10 % in Tol)

BJ1 activated, VD with APDIPES:CPDMMS 2:13 (50 µL,10 % in Tol), labelled with **1**

BK activated, VD with APDIPES:CPDMMS 1:29 (50 µL,10 % in Tol)

BK1 activated, VD with APDIPES:CPDMMS 1:29 (50 µL,10 % in Tol), labelled with **1**

BL activated, VD with APDIPES:CPDMMS 1:74 (50 µL,10 % in Tol)

BL1 activated, VD with APDIPES:CPDMMS 1:74 (50 µL,10 % in Tol), labelled with **1**

BM activated, VD with APDIPES:CPDMMS 1:224 (50 µL,10 % in Tol)

BM1 activated, VD with APDIPES:CPDMMS 1:224 (50 µL,10 % in Tol), labelled with **1**

BN activated, VD with APDIPES:CPDMMS 1:899 (50 µL,10 % in Tol)

BN1 activated, VD with APDIPES:CPDMMS 1:899 (50 µL,10 % in Tol), labelled with **1**

BO activated, VD with APDIPES:CPDMMS 1:2249 (50 µL,10 % in Tol)

BO1 activated, VD with APDIPES:CPDMMS 1:2249 (50 µL,10 % in Tol), labelled with **1**

BP activated, VD with APDIPES:CPDMMS 1:6749 (50 µL,10 % in Tol)

BP1 activated, VD with APDIPES:CPDMMS 1:6749 (50 µL,10 % in Tol), labelled with **1**

BQ activated, VD with CPDMMS (50 µL,10 % in Tol)

BQ1 activated, VD with CPDMMS (50 µL,10 % in Tol), labelled with **1**

CC activated, VD with APDIPES (50 µL,10 % in Tol)

CC1 activated, VD with APDIPES (50 µL,10 % in Tol), labelled with **1**

CD activated, VD with APDIPES:CPDMMS 1:1 (50 µL,10 % in Tol)

CD1 activated, VD with APDIPES:CPDMMS 1:1 (50 µL,10 % in Tol), labelled with **1**

CE activated, VD with APDIPES:CPDMMS 1:3 (50 µL,10 % in Tol)

CE1 activated, VD with APDIPES:CPDMMS 1:3 (50 µL,10 % in Tol), labelled with **1**

CF activated, VD with APDIPES:CPDMMS 1:7 (50 µL,10 % in Tol)

CF1 activated, VD with APDIPES:CPDMMS 1:7 (50 µL,10 % in Tol), labelled with **1**

CG activated, VD with APDIPES:CPDMMS 1:15 (50 µL,10 % in Tol)

CG1 activated, VD with APDIPES:CPDMMS 1:15 (50 µL,10 % in Tol), labelled with **1**

CH activated, VD with APDIPES:CPDMMS 1:31 (50 µL,10 % in Tol)

CH1 activated, VD with APDIPES:CPDMMS 1:31 (50 µL,10 % in Tol), labelled with **1**

CI activated, VD with APDIPES:CPDMMS 1:63 (50 µL,10 % in Tol)

CI1 activated, VD with APDIPES:CPDMMS 1:63 (50 µL,10 % in Tol), labelled with **1**

CJ activated, VD with APDIPES:CPDMMS 1:127 (50 µL,10 % in Tol)

CJ1 activated, VD with APDIPES:CPDMMS 1:127 (50 µL,10 % in Tol), labelled with **1**

CK activated, VD with APDIPES:CPDMMS 1:255 (50 µL,10 % in Tol)

CK1 activated, VD with APDIPES:CPDMMS 1:255 (50 µL,10 % in Tol), labelled with **1**

CL activated, VD with CPDMMS (50 µL,10 % in Tol)

CL1 activated, VD with CPDMMS (50 µL,10 % in Tol), labelled with **1**

CM activated, VD with APTES (50 µL,10 % in Tol)

CM1 activated, VD with APTES (50 µL,10 % in Tol), labelled with **1**

CNR activated, VD with APTES (50 µL,10 % in Tol), labelled with RITC

CO activated, VD with APTES:CETES 1:1 (50 µL,10 % in Tol)

CO1 activated, VD with APTES:CETES 1:1 (50 µL,10 % in Tol), labelled with **1**

COR activated, VD with APTES:CETES 1:1 (50 µL,10 % in Tol), labelled with RITC

CP activated, VD with APTES:CETES 1:3 (50 µL,10 % in Tol)

CP1 activated, VD with APTES:CETES 1:3 (50 µL,10 % in Tol), labelled with **1**

CPR activated, VD with APTES:CETES 1:3 (50 µL,10 % in Tol), labelled with RITC

CQ activated, VD with APTES:CETES 1:7 (50 µL,10 % in Tol)

CQ1 activated, VD with APTES:CETES 1:7 (50 µL,10 % in Tol), labelled with **1**

CQR activated, VD with APTES:CETES 1:7 (50 µL,10 % in Tol), labelled with RITC

CR activated, VD with CETES (50 µL,10 % in Tol)

CR1 activated, VD with CETES (50 µL,10 % in Tol), labelled with **1**

CRR activated, VD with CETES (50 µL,10 % in Tol), labelled with RITC

CS activated, VD with APDIPES (50 µL,10 % in Tol)

CS1 activated, VD with APDIPES (50 µL,10 % in Tol), labelled with **1**

CS10 activated, VD with APDIPES (50 µL,10 % in Tol), labelled with **10**

CS11 activated, VD with APDIPES (50 µL,10 % in Tol), labelled with **11**

CS12 activated, VD with APDIPES (50 µL,10 % in Tol), labelled with **12**

CT11 activated, VD with APDIPES:CPDMMS 1:1 (50 µL,10 % in Tol), labelled with **11**

CT12 activated, VD with APDIPES:CPDMMS 1:1 (50 µL,10 % in Tol), labelled with **12**

CU11 activated, VD with APDIPES:CPDMMS 1:3 (50 µL,10 % in Tol), labelled with **11**

CU12 activated, VD with APDIPES:CPDMMS 1:3 (50 µL,10 % in Tol), labelled with **12**

CV11 activated, VD with APDIPES:CPDMMS 1:7 (50 µL,10 % in Tol), labelled with **14**

CV12 activated, VD with APDIPES:CPDMMS 1:7 (50 µL,10 % in Tol), labelled with **12**

CW activated, VD with CPDMMS (50 µL,10 % in Tol)

CW1 activated, VD with CPDMMS (50 µL,10 % in Tol), labelled with **1**

CW10 activated, VD with CPDMMS (50 µL,10 % in Tol), labelled with **10**

CW11 activated, VD with CPDMMS (50 µL,10 % in Tol), labelled with **11**

CW12 activated, VD with CPDMMS (50 µL,10 % in Tol), labelled with **12**

Publications

Journal Articles

1. Ast, S.; Fischer, T.; Müller, H.; Mickler, W.; Schwichtenberg, M.; Rurack, K.; Holdt, H.-J. **Integration of the 1,2,3-Triazole „Click“ Motif as a Potent Signalling Element in Metal Ion Responsive Fluorescent Probes.** *Chemistry – A European Journal* **2013**, *19*, 2990–3005

2. Hecht, M.; Fischer, T.; Dietrich, P. M.; Werner, K.; Descalzo, A. B.; Unger, W. E. S., Rurack, K. **Fluorinated Boron-Dipyrromethene (BODIPY) Dyes: Bright and Versatile Probes for Surface Analysis.** *ChemistryOpen* **2013**, *2*, 25–38

3. Fischer, T.; Dietrich, P. M.; Streeck, C.; Ray, S.; Nutsch, A.; Shard, A. G.; Beckhoff, B.; Unger, W. E. S.; Rurack, K. **Quantification of Variable Functional-Group Densities of Mixed-Silane Monolayers on Surfaces via a Dual-Mode Fluorescence and XPS Label.** *Analytical Chemistry* **2015**, *87*, 2685-2692

4. Lempke, L.; Fischer, T.; Bell, J.; Kraus, W.; Rurack, K.; Krause, N. **Gold-catalyzed allene cycloisomerization for pyrrole synthesis: towards highly fluorinated BODIPY dyes.** *Organic & Biomolecular Chemistry* **2015**, *13*, 3787-3791

5. Fischer, T.; Dietrich, P. M., Unger, W. E. S., Rurack, K. **Multi-mode Surface Functional Group Determination – Combining Steady-state and Time-resolved Fluorescence with XPS and Absorption Measurements for Absolute Quantification.** *Analytical Chemistry* **2016**, *88*, 1210-1217

Oral presentations

1. Nutsch, A.; Streeck, C.; Beckhoff, B.; Dietrich, P. M.; Fischer, T.; Rurack, K.; Unger, W. E. S. **Soft X-Rays with varying Energies for Characterization of Fluorescence Markers.** 15th European Conference on Applications of Surface and Interface Analysis 2013 (ECASIA'13): Sardinia, Italy, 13.-18.10.2013

2. Fischer, T; Hecht, M.; Dietrich, P. M.; Unger, W. E. S.; Nutsch, A; Streeck, C.; Weser, J.; Beckhoff, B.; Rurack, K. **Application of dual-mode XPS and fluorescence labels in the quantification of surface functional groups.** 15th European Conference on Applications of Surface and Interface Analysis 2013 (ECASIA'13): Sardinia, Italy, 13.-18.10.2013

Poster presentations

1. Fischer, T.; Hecht, M.; Dietrich, P. M.; Unger, W. E. S.; Rurack, K. **Development of a dual XPS and Fluorescence Label for the Analysis of Surface Amino Groups.** ThGOT, 8. Thementage Grenz und Oberflächentechnik: Leipzig, Germany, 04.-05.09.2012

2. Hecht, M.; Fischer, T. ; Dietrich, P. M.; Unger, W. E. S.; Rurack, K. **Development and Characterization of a Photostable Boron-dipyrromethene Dye as a Versatile Probe of the Analysis of Surface Functional Groups.** Nanocon2012 : Brno, Czech Republic, 23.-25.10.2012

3. Fischer, T.; Hecht, M.; Dietrich, P. M.; Unger, W. E. S.; Rurack, K. **Towards Quantitative Surface Amino Group Analysis with One Combined Fluorescence and XPS Label.** ANAKON 2013: Essen, Germany, 04.-07.03.2013

4. Lempke, L.; Kronenberg, L.; Fischer, T.; Rurack, K.; Krause, N. **Gold-catalyzed cycloisomerization of flourinated allenes: Application in BODIPY-synthesis.** 15. JFC Frühjahrssymposium: Berlin, Germany, 06.-09.03.2013

5. Fischer, T.; Hecht, M.; Dietrich, P. M.; Unger, W. E. S.; Rurack, K. **Quantifizierung von Oberflächenaminogruppen mithilfe eines dualen XPS- und Fluoreszenzlabels.** 8. Deutsche BioSensor Symposium: Wildau, Germany, 10.-13.03.2013

6. Kraus, W.; Hecht, M.; Fischer, T.; Rurack, K. **Fluorinated Boron-dipyrromethen (BODIPY) Structures for Surface Analysis.** 21. Jahrestagung der deutschen Gesellschaft für Kristallographie: Freiberg, Germany, 19.-22.03.2013

7. Nutsch, A.; Streeck, C.; Beckhoff, B.; Dietrich, P. M.; Fischer, T.; Rurack, K.; Unger, W. E. S. **Traceable quantitative surface chemical analysis for industrial applications.** 9th International Nanotechnology Conference on Communication and Cooperation: Berlin, Germany, 14.17.04.2013

8. Streeck, C.; Nutsch, A.; Beckhoff, B.; Dietrich, P. M.; Fischer, T.; Rurack, K.; Unger, W. E. S. **Reference-free total reflection X-ray fluorescence analysis for surface functional group quantification of funtional groups on surfaces for bio-analytical applications.** E-MRS 2014 Spring Meeting: Lille, Fance, 26.-30.05.2014

Selbstständigkeitserklärung

Hiermit erkläre ich, dass ich die vorliegende Arbeit selbstständig angefertigt, sowie keine anderen als die angegebenen Quellen und Hilfsmittel verwendet habe. Diese Arbeit wurde bisher keiner anderen Prüfungsbehörde vorgelegt.

Berlin, den

_____

Tobias Fischer